E.T.S. de Ingeniería Industrial,
Informática y de Telecomunicación

Design of the power electronics of a city bus charging station supported by stationary energy storage system and photovoltaic generation

Grado en Ingeniería
en Tecnologías Industriales

Trabajo Fin de Grado

Autor: Guilermo Puy Pérez de Laborda

Directores: Pablo Sanchis y Alfredo Ursúa

Pamplona, 12 de Junio de 2020

upna Universidad Pública de Navarra
Nafarroako Unibertsitate Publikoa

ABSTRACT

This BSc Thesis analyses different options for the power electronics needed to interconnect a city bus charging station with a support system based on stationary lithium-ion storage and photovoltaic generation. First, the currently used topologies are analyzed by conducting a review of the existing literature. Secondly, and based on the previous study, various alternatives are proposed for connecting the three elements of the system (charger, stationary support battery and photovoltaic system) to each other and to the grid. Subsequently, the options proposed are designed and sized. Their efficiencies are also studied in the light of different operating profiles. The final comparison allows the selection of the most interesting alternative in terms of topology and energy efficiency. The most interesting option in terms of costs for semiconductors, passive components and the necessary transformer is also determined.

Keywords: fast charging station, e-bus, efficiency, cost, stationary energy storage system, PV generation

RESUMEN

En este Trabajo de Fin de Grado se analizan diferentes opciones de configuración para la electrónica de potencia necesaria para interconectar una estación de carga de autobuses urbanos con un sistema de apoyo basado en almacenamiento estacionario de iones de litio y generación fotovoltaica. En primer lugar, se realiza un estado del arte de las opciones actualmente utilizadas. En segundo lugar, y en función del estudio anterior, se plantean diversas alternativas para el conexionado de los tres elementos del sistema (cargador, batería estacionaria de apoyo e instalación fotovoltaica) entre sí y a la red eléctrica. Posteriormente, se diseñan y dimensionan las opciones planteadas. También se estudian sus eficiencias ante diferentes perfiles de funcionamiento. La comparación final permite seleccionar la alternativa más interesante a nivel topológico y de eficiencia energética. También se determina la opción más interesante a nivel de costes en cuanto a semiconductores, componentes pasivos y transformador necesario.

Palabras clave: estación de carga rápida, autobús eléctrico, eficiencia, coste, almacenamiento estacionario, generación PV

TABLE OF CONTENTS

LIST OF FIGURES

LIST OF TABLES

LIST OF ABBREVIATIONS

EV	Electric Vehicle
V2G	Vehicle to Grid
AC	Alternating Current
DC	Direct Current
DCFC	Direct Current Fast Charge
DC/DC	Direct Current - Direct Current
AC/DC	Alternating Current - Direct Current
HF	High-Frequency
LF	Low-Frequency
Li-ion	Lithium-Ion
SoC	State of Charge
C	Capacity
THD	Total Harmonic Distortion
PV	Photovoltaic
ESS	Energy Storage System
MV	Medium Voltage
LV	Low Voltage
BEB	Battery-Electric Bus
e-Bus	Electric Bus
CC-CV	Constant Current-Constant Voltage
AFE	Active Front End
L	Inductance
ESR	Equivalent Series Resistance
FCS	Fast Charging Stations

1 Introduction

1.1 Motivation

Concern for the environment, the possibility of reducing pollution, and the gradual increase in oil consumption in recent decades have meant that the transport sector is constantly evolving in the search for other energy sources that can replace petrol and diesel.

In the present day, electricity is the source on which vehicle brands, the European Union, and mostly the customers bet, mainly because if its lesser impact on the environment and the possible obtaining of this energy through renewable sources.

In this context arises the project "New e-Bus line integrated with Smart Grid" in Pamplona, a project carried out technically by the UPNA and supported by the Mancomunidad de Pamplona and CENER. This project or better called "task", arises within the STARDUST project, belonging to the EU Horizon 2020 Smart Cities program, in which different holistic solutions have been implemented in areas such as building, energy and electric mobility. In this project, Pamplona is situated as one of the so-called lighthouse cities, for which the task already mentioned is only one of them.

One of the most innovative components that compose the New e-Bus line integrated with Smart Grid task is a charging station with a support system formed by a stationary battery and photovoltaic generation.

In order to carry out the task, 3 theoretical studies were planned accompanied by the subsequent implementation. The 3 theoretical studies focus on power electronics, the analysis of the electrochemical functioning of the batteries of the support system, and the energy management of the complete system. The execution of these studies would be carried out later through the implementation of the installation.

For the above-mentioned reasons, this BSc. thesis " Design of the power electronics of a city bus charging station supported by stationary energy storage system and photovoltaic generation" is carried out, where the aim is to select the most interesting alternative for power electronics on a topological and energy efficiency level.

1.2 Research aims and objectives

This project aims to make a comparison between the configuration options that will be proposed for the power electronics needed to interconnect an urban e-bus charging station with a support system based on stationary lithium-ion storage and photovoltaic generation.

The final comparison will allow the selection of the most interesting alternative on a topological and energy efficiency level. A cost comparison is also included for which the full costs of the proposed configurations have not been considered but only the costs of the semiconductors, passive components, and transformers.

1.3 Thesis outline

This project is structured in 10 chapters:

- Chapter 1: motivation, the research aims and objectives, and the thesis outline

- Chapter 2: the existing EV charging modes are listed, as well as the most common configuration proposals for EV charging stations.
- Chapter 3: description of the current FSC at UPNA.
- Chapter 4: analysis of the existing possibilities for the support system.
- Chapter 5: proposal and sizing of the connection of the three elements of the system (recharging point, ESS, and photovoltaic system) to each other and the grid.
- Chapter 6: description of the methodology used for the calculation of losses. The results obtained are analyzed.
- Chapter 7: estimate of the costs in terms of semiconductors, passive components, and transformer of each of the configurations.
- Chapter 8: global comparison of the configurations.
- Chapter 9: alternative of implementing interleaved converters.
- Chapter 10: conclusions and future work.

2 Literature review

This chapter will first analyse the charging modes according to IEC 61851. Next, the most common topologies proposed for EV chargers will be analysed, focusing on the fast-charging ones, which are the ones relevant to this project.

2.1 Electric vehicle charger modes

IEC 61851 defines 4 different EV charger modes:

- Mode 1. Corresponds to slow charge. The electric vehicle is connected to the AC grid through a standard connection and without exceeding a consumption of 16 A per phase and 11 kW. The rectifier is located at the vehicle itself. This type of charging is usually done at home.
- Mode 2. Corresponds to slow charge. The electric vehicle is connected to the AC grid via a specific connection since intermediate protection is required in addition to charge regulation. The maximum consumption is 32 A per phase and 22 kW. The rectifier is situated in the vehicle itself. This type of charge is common in private installations.
- Mode 3 corresponds to the so-called slow or semi-fast charge. The electric vehicle is connected to the AC grid via a specific connection since intermediate protection is required in addition to charge regulation. The maximum consumption is 63 A per phase and 43 kW. The rectifier is placed on the vehicle itself. This type of charge is common in public charging stations.
- Mode 4. Corresponds to the so-called fast charge or DC charge. The electric vehicle is connected to a DC grid, using an external charger. The maximum consumption is 400 A per phase and 240 kW. This type of charging is common in public charging stations.

2.2 Single-phase on-board chargers

The charge corresponding to modes 1, 2 and 3 have in common that the rectifier for charging the EV battery is situated in the EV. Depending on whether they have the possibility of returning power from their battery to the grid (V2G technology), there are 2 types of structures, as shown in Fig. 2.1:

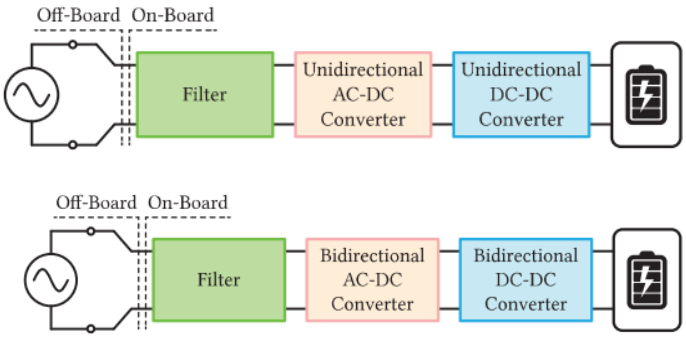

Fig. 2.1. Two different topologies (unidirectional and bidirectional) in the on-board chargers [1]

Some classic examples of each of these topologies for single-phase charges are the following:

- For unidirectional topology, it is common to use a diode bridge as a rectifier, as shown in Fig. 2.2. A DC/DC converter is used to control the power factor. And other DC/DC converter with galvanic isolation is the one that in the end controls the EV battery

charge. It is common to use a full bridge to invert the signal and then to rectify it with a diode bridge [1].

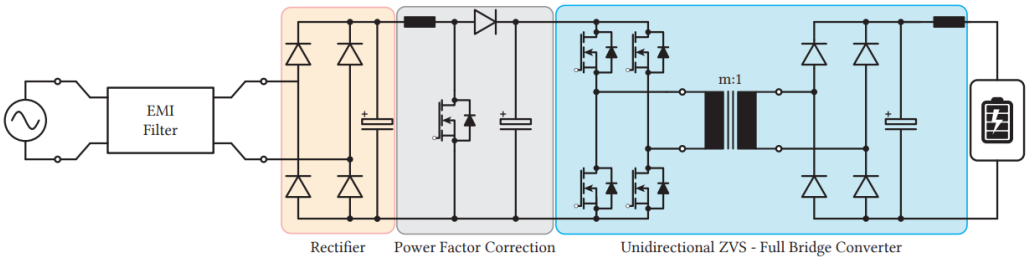

Fig. 2.2. Common topology for single-phase unidirectional on-board charger [1]

- For bidirectional topology, it is common to use a full bridge, also known as an H-bridge, as a rectifier, as shown in Fig. 2.3. The DC/DC converter that controls the EV battery provides galvanic isolation. It is common to use a full bridge to invert the signal and then to rectify it again with another full bridge [1].

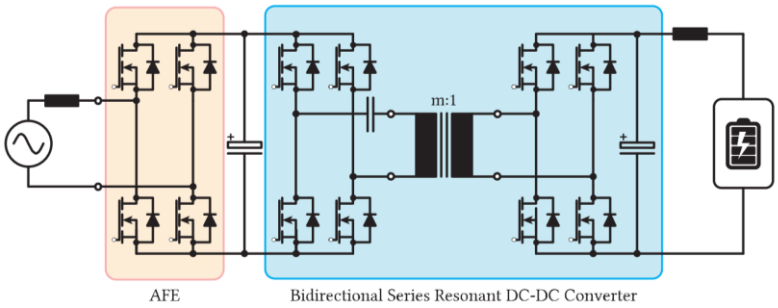

Fig. 2.3. Common topology for bidirectional single-phase on-board charger [1]

2.3 Off-board DC chargers: Fast charging stations

This project is focused on type 4 charging mode because, for an e-Bus (Electric Bus) circulating in the city to be able to carry out its journey without being parked for hours while the BEB (Battery-Electric Bus) is being charged, it is necessary to apply a great deal of charging power to the batteries that it carries. This can currently only be done with a power corresponding to charge mode 4, in which the charger is outside the EV and the charge is made in DC. Several research papers have been analyzed in this thesis to observe the different power electronics architectures proposed in the literature for FCS (Fast Charging Stations). The following general classification of architectures has been made:

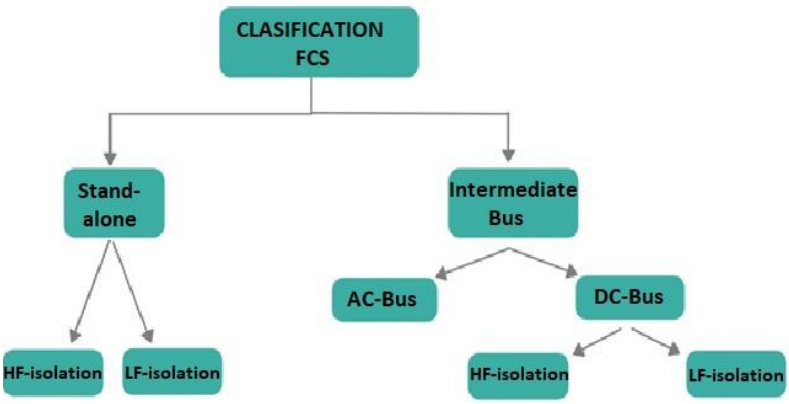

Fig. 2.4. Classification of FCS

2.3.1 Stand-alone charging station

This type of charge corresponds to the one that now exists at UPNA for line 9. This electronic structure is simply composed of:

- A transformer providing galvanic isolation
- A rectifier that allows the charging in DC, assuming that the energy is taken from the grid
- A single DC/DC converter that controls the charge of the only existing recharge pole.
- In addition, it is necessary to include a filter between the grid and the rectifier to reduce the harmonics generated.

Depending on how the galvanic isolation is carried out, two types of direct charging can be differentiated: using a low-frequency (LF) isolation or a high-frequency (HF) isolation.

With low-frequency isolation

The electronic structure consists of a low-frequency transformer and a rectifier. In addition, a filter should be added to attenuate the harmonics and comply with existing regulations. in [2] the use of a thyristor bridge (Fig. 2.5 a), a diode bridge with a subsequent charge regulator that controls the power factor (Fig. 2.5 b), and an active rectifier (Fig. 2.5 c) are considered as possible rectifiers. The study simulates the last option for a power of 300 kW by adding an inductive filter. A THD of 0.42 % is calculated taking into account up to harmonic 50 (2500 Hz).

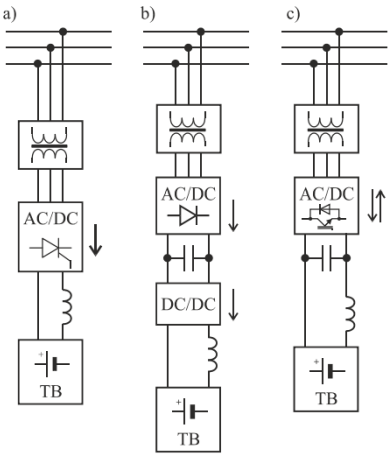

Fig. 2.5. Different topologies for the FCS: a) based on thyristor bridge b) based on diode bridge c) based on active rectifier [2]

With high-frequency isolation

In [3] it is compared the use of a structure like the one mentioned above with another one using high-frequency isolation. The great advantage of this option is the smaller size of the transformer.

The proposed structure is the one shown in Fig. 2.6 (a), for an output of up to 300 kW. It comprises:

- An LCL filter between the grid and the rectifier to comply with the harmonic regulation.
- an active rectifier
- two DC-DC converters in parallel with high-frequency galvanic isolation. The topology of these DC-DC converters is shown in Fig. 2.6 (b).

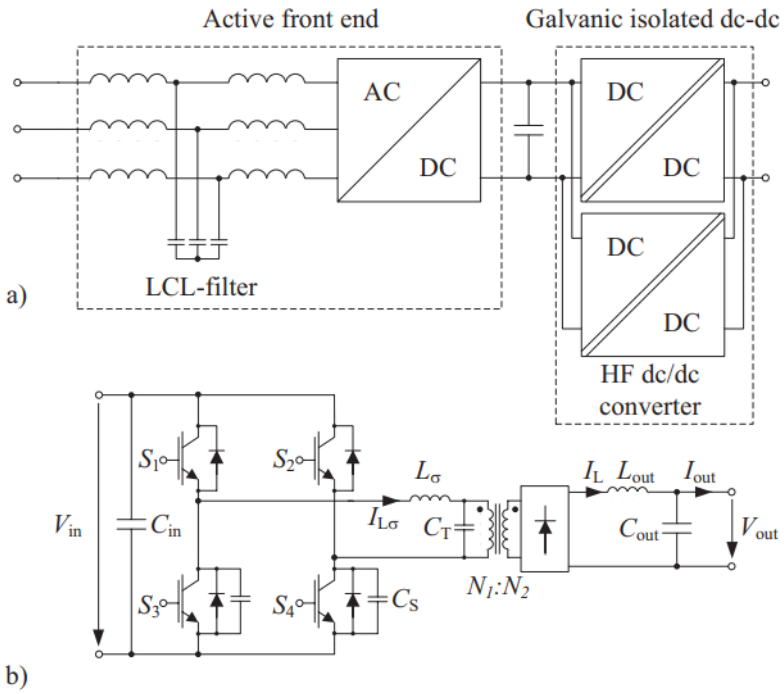

Fig. 2.6. a) Solution for HF converter solution for FCS with two in parallel connected galvanic isolated dc-dc stages and b) HF dc-dc isolated converter topology [3]

As can be seen in Fig. 2.6 (b), the HF dc-dc isolated converter comprises:

- an H-bridge inverter (single-phase) operated at a frequency of 8 kHz
- the transformer, of a necessary size smaller than if it were placed between the rectifier and the grid operating at low frequency
- a diode bridge with its corresponding filter to deliver power to the EV battery

2.3.2 Distributed charging station

When the structure has more elements, an intermediate Bus is used. This is the case, for example, when there is more than one pole to recharge more than one vehicle at a time, or when ESS (Energy Storage System) or a renewable energy source is incorporated. In these cases, there are two possibilities for making the connections of these elements, as can be seen in Fig. 2.7: in AC or DC.

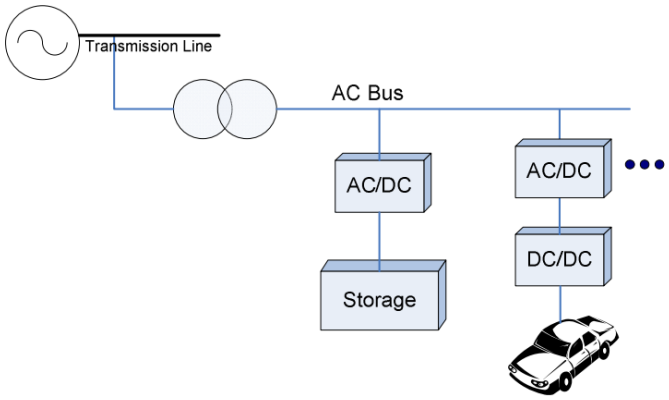

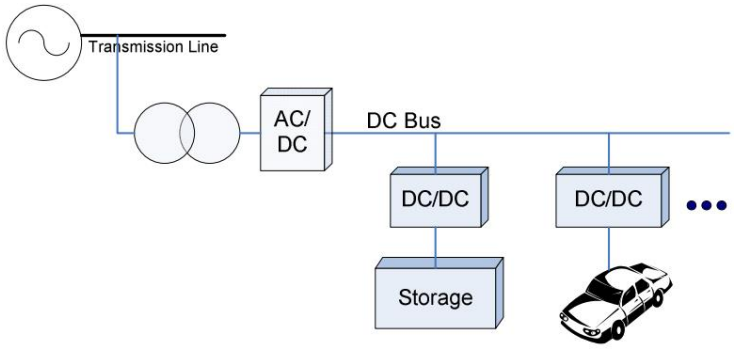

Fig. 2.7. Two different ways to implement the FCS with an intermediate Bus: AC-Bus or DC-Bus [4]

From a practical point of view, it may seem that using an AC-Bus may be more useful because this system has been used for more years and therefore there are more technologies and more developments than for DC. Also, in the event that the ESS and renewable energy sources are to be included once the charging point already exists on a stand-alone architecture, this may be a more convenient way if, for example, there is no access to the DC-Bus.

However, DC-Bus provides a more convenient way to integrate renewable energy sources and ESSs. If all the elements that work in DC were connected to an AC-Bus, an inverter would be needed for each of them, having theoretically more costs in losses and hardware. This is the reason because the use of the DC-Bus predominates over the AC-Bus [4]. Still, in this project it will be checked precisely if that is totally true for the FSC to be designed.

A DC-Bus architecture connected to the alternating power grid consists of a transformer, a rectifier and a DC/DC converter for each of the elements connected to the DC-Bus.

With this type of configuration, the proposal in [5] has been analyzed first. The topology proposed in [5] is the one shown in Fig. 2.8. The installation has an ESS in addition to the integration of a renewable energy source, concretely 100 kWp photovoltaic panels.

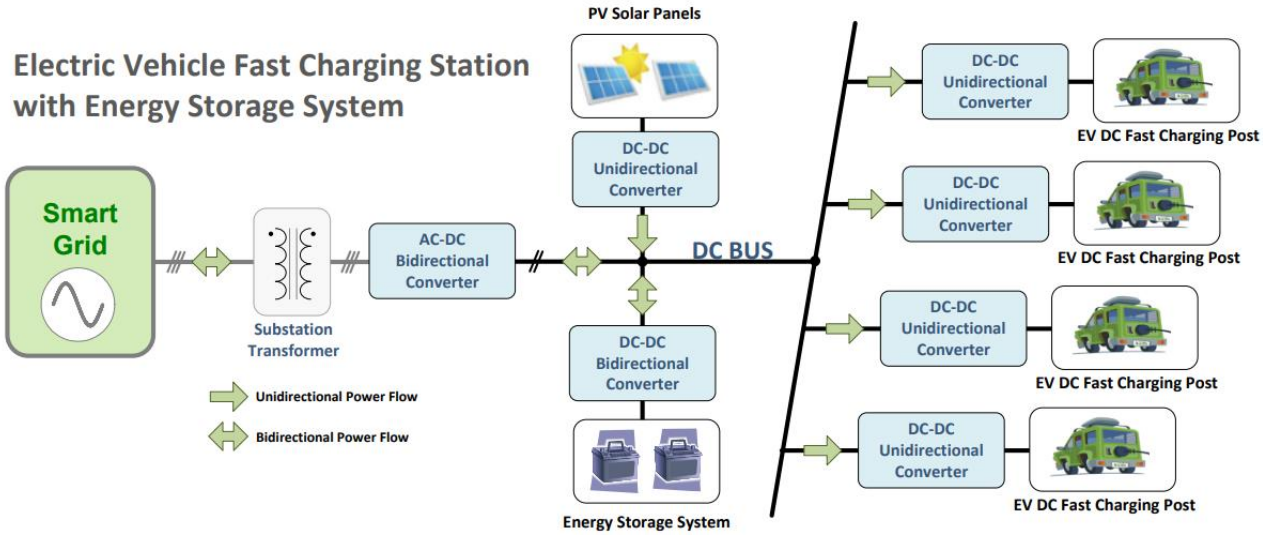

Fig. 2.8. Block diagram of the proposed architecture for the FCS with ESS and a renewable energy source [5]

The first converter connects the DC-Bus with the EG. To have the possibility to use the V2G technology, a bidirectional rectifier has been selected. Taking into account the application and

the required nominal power (150 kW), a three-phase interleaved rectifier has been chosen, as represented in Fig. 2.9. It consists of three similar three-phase IGBT bridges, sharing the same DC-Bus, and using a second-order passive low-pass LC filter on the grid side.

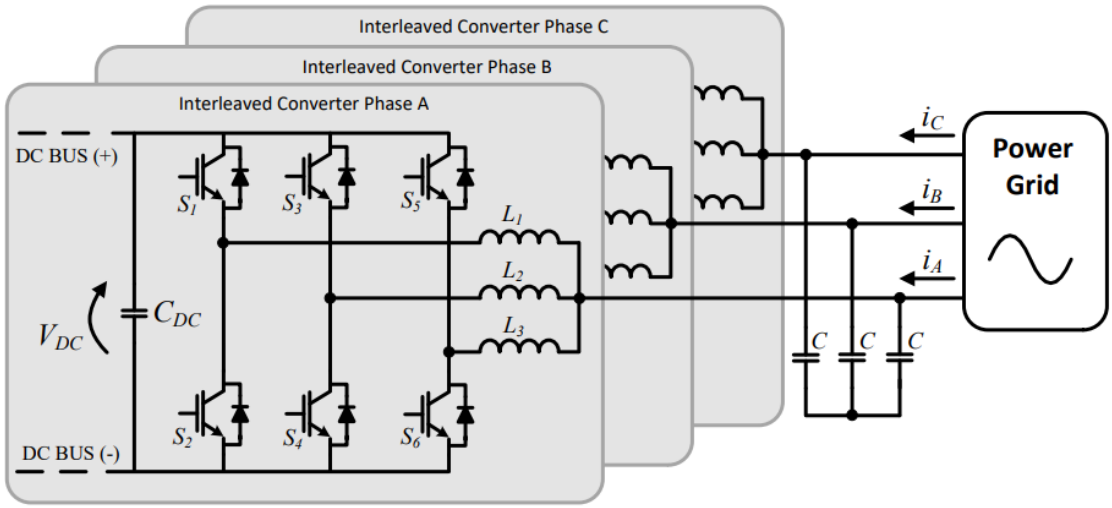

Fig. 2.9. Three-phase interleaved bidirectional AC-DC [5]

To charge the EV batteries, a buck type converter is required. For a converter with nominal power of 50 kW, the interleaved topology has been chosen, instead of a buck-type converter, thus allowing decreasing the switching frequency and the nominal power of each semiconductor, keeping a low current ripple on the battery side. This converter is shown in Fig. 2.10.

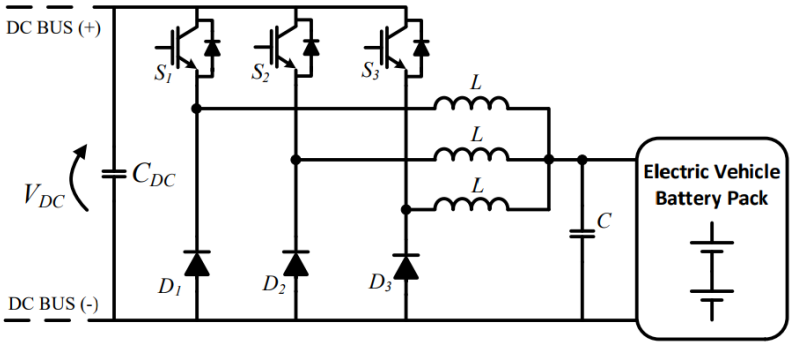

Fig. 2.10. Interleaved buck-type DC-DC power converter used to interface the DC-Bus of the FCS with the EV battery [5]

The ESS is connected to the Bus with a bidirectional DC-DC converter. Taking into account the required nominal power of the converter (300 kW), the bidirectional DC-DC interleaved converter has been selected, shown in Fig. 2.11.

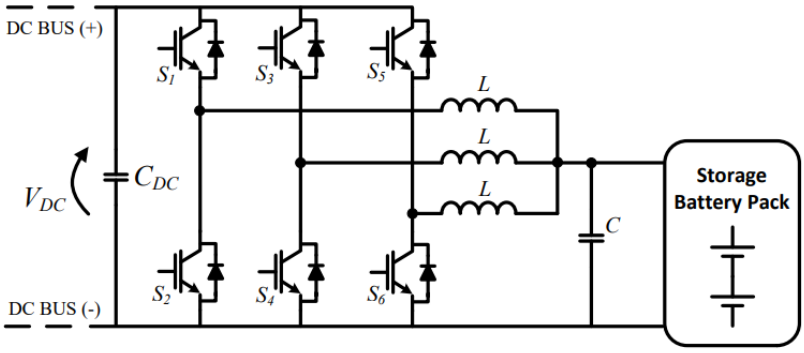

Fig. 2.11. Interleaved bidirectional buck-boost DC-DC converter used to interface the DC-Bus of the FCS with the battery ESS [5]

The connection to the photovoltaic system is proposed to be done with a boost converter with controlled input current according to the power extracted from the PVs. Depending on the maximum power of the photovoltaic solar panels, the options of selecting a simple boos-type converter or an interleaved converter with 2 or 3 legs can be considered, as represented in the Fig. 2.12.

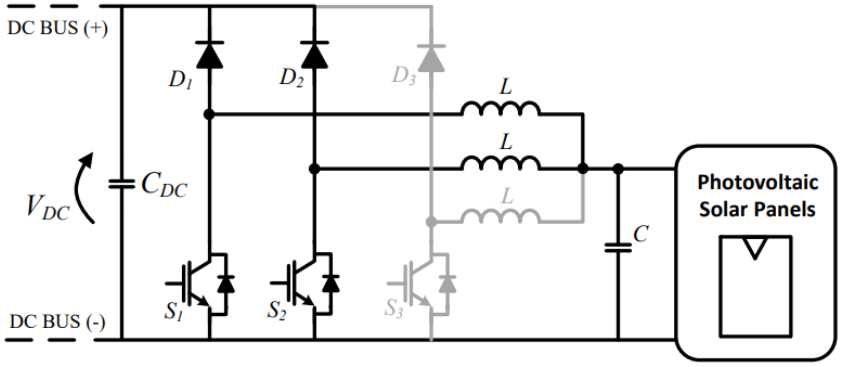

Fig. 2.12. Interleaved boost-type DC-DC converter used to interface an array of PV solar panels with the DC-Bus of the FCS [5]

The topology proposed in [4] is provided with ESS as in the previous paper but without a renewable energy source. In other words, all the power used to charge the vehicles is taken from the grid but using an ESS to mitigate the oscillation in the power demand.

The selected AC/DC converter must have a power of 1.1 MW for this installation. The paper compares the use of a 6-pulse diode bridge with a 12-pulse one and concludes that the 12-pulse diode rectifier is the most suitable topology for this application. This is mainly because with this rectifier a higher reduction of output harmonics can be achieved than with a 6-pulse rectifier. Specifically, two 6-pulse diode rectifiers are connected in series. The DC-Bus voltage is controlled by two buck-boost converters as shown in the Fig. 2.13. These converters are also responsible for the active filtering of the current harmonics generated by the rectifier. With this configuration, it is determined that the harmonics can be reduced to less than 5% at full load.

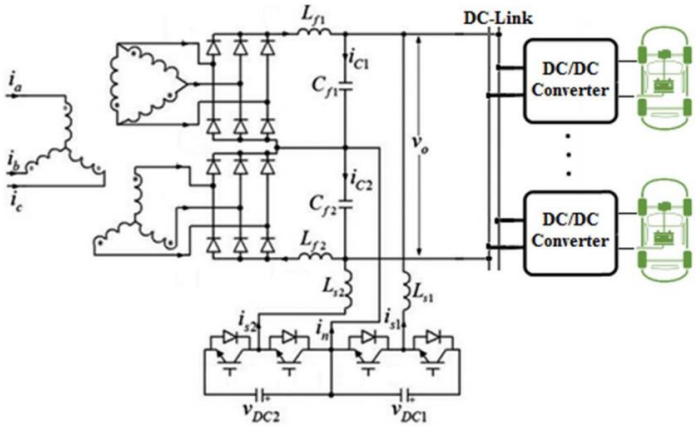

Fig. 2.13. 12-pulse diode rectifier with harmonic reduction via two buck-boost converters [4]

In the case of DC/DC converters, the Half-bridge buck-boost converter, and the Three-level Buck-boost converter are studied in detail, topologies that can be shown in Fig. 2.14. And Fig. 2.15. The option of unidirectional converters is not considered to offer the possibility of using V2G technology. The paper shows how the Three-level buck-boost converter shows a better performance in almost all aspects when being used as the charge regulator of the 180 kW ESS. Besides, a variable switching frequency strategy is proposed to obtain better efficiency.

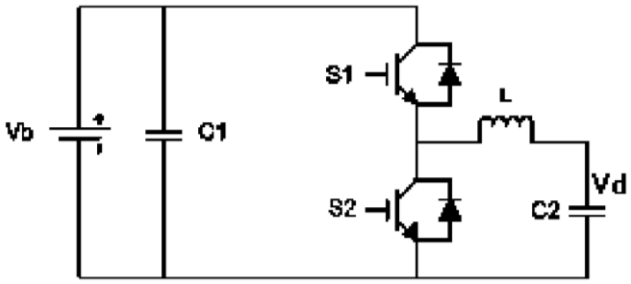

Fig. 2.14. Half-bridge buck-boost converter [4]

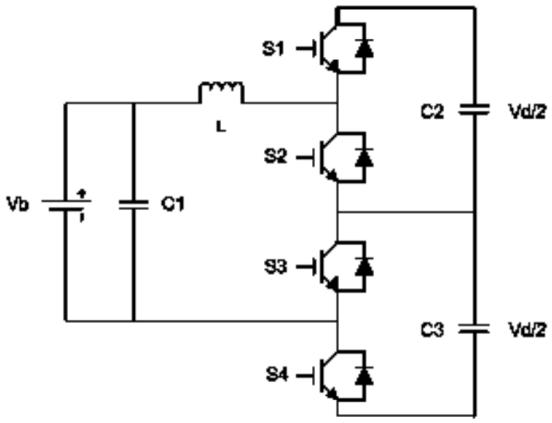

Fig. 2.15. Three-level buck-boost converter [4]

3 Present fast charging station at UPNA

This chapter will first discuss the data of the current FCS at UPNA provided by the Department of Electrical Engineering of the same university. Then, the topology used will be analysed in more detail, and finally a comparison will be made between the DC/DC converter used and a single-leg converter.

3.1 Current FCS data

3.1.1 Connection and Transformation center

The connection is made on the 13.2 kV distribution grid that runs along Cataluña Street. The transformation center is provided with a 13.2 kV/400 V transformer with a power of 350 kVA. The maximum power of the cabling between the transformation centre and the charging point is known to be 300 kW.

3.1.2 Charging point

The charging point consists of the power electronics, a pantograph, and the pick-up system. Power electronics data:

- Maximum power: 300 kW
    - The power electronics consists of 20 buck-boost converter of 15 kW each in parallel
- Input/Output: AC/DC
- Average energy of the charges (DC side): 10 kWh (according to Vectia)

After some measurements on the AC side of the charging point, the following conclusions on the charges were obtained:

- Maximum power: 250 kW
- Maximum current: 625 A
- Average energy of the charges (AC side): 12 kWh
- Average charge duration: 3.5 min

Fig. 3.1 shows the profile of a charge.

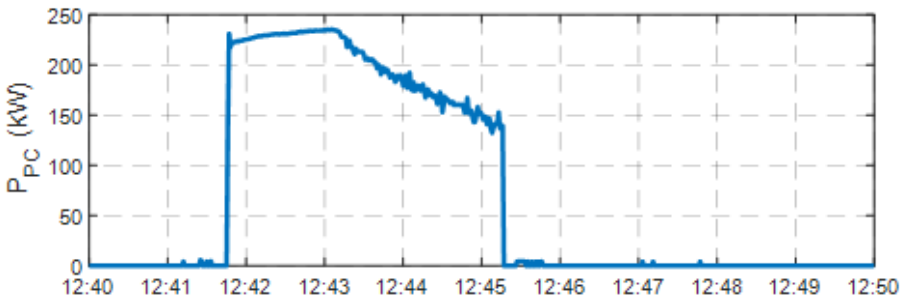

Fig. 3.1. Example of a charge measured and its profile

The profile clearly shows that the charge consists of two clearly differentiated periods, a first ascending and a second descending part. In the ascending period, the current is constant and the power increases as the e-bus battery voltage increases while recharging. In the second

period, the charging voltage remains constant and the current decreases, therefore the downward slope.

The type of batteries used in these buses corresponds to lithium-ion, which are recharged as shown in figure 3.1, that is CC-CV (constant current – constant voltage) type charge.

The nominal voltage of the battery is 650 VDC. And depending on the state of charge of the battery during charging, the voltage at the output of the point of charge will be higher or lower than this value.

3.2 Analysis of the current fast charging station

Firstly, it should be noted that the topology used is that composed of an LF transformer, a rectifier, and a unidirectional DC/DC converter that controls the charge. The function of the transformer is none other than to lower the MV (13.2 kV) to LV (400 V) in addition to providing galvanic isolation. It is located in the transformation center of the Fig. 3.2. The rectifier is then responsible for rectifying the signal. Although there is no data to confirm this, it is certainly an active rectifier. And finally, the buck-boost type converter with 20 identical parallel legs.

The maximum and minimum charging voltage downstream of the charging station can be calculated in the knowledge that the nominal charging voltage is about 650V, according to the data provided above.

From the operating range of a lithium cell of the LTO type, which are those used in buses on line 9 the number of cells can first be obtained and then the voltage of the fully discharged and fully charged battery can be calculated. For this purpose, they are needed the voltage values of cell, which are shown in Table 3.1.

Paramater	Value
Minimum voltage (fully discharged battery)	1.5V
Nominal voltage	2.3V
Maximum voltage (fully charged battery)	2.9V

Table 3.1. Parameters of the battery cell used in the buses of the current FCS

These values determine that the number of cells in the battery of line 9 buses is 280.

This means that during the charging process the voltage may vary from 420 V (fully discharged) to 820 V (fully charged).

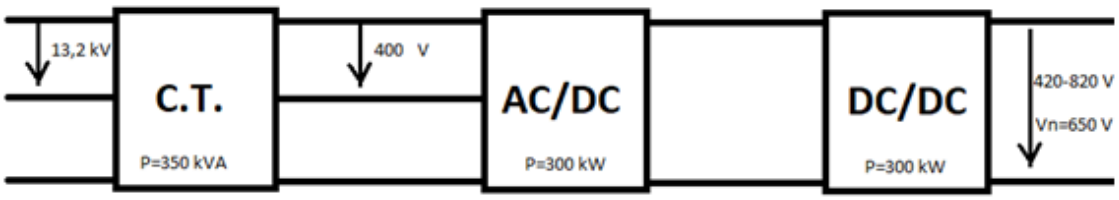

Fig. 3.2. Scheme of the present FCS

Observing the profile of a CC-CV type charge on Fig. 3.3, the maximum charge power is given at the moment of maximum voltage, which corresponds with the fully charged battery voltage, and at the moment of maximum current.

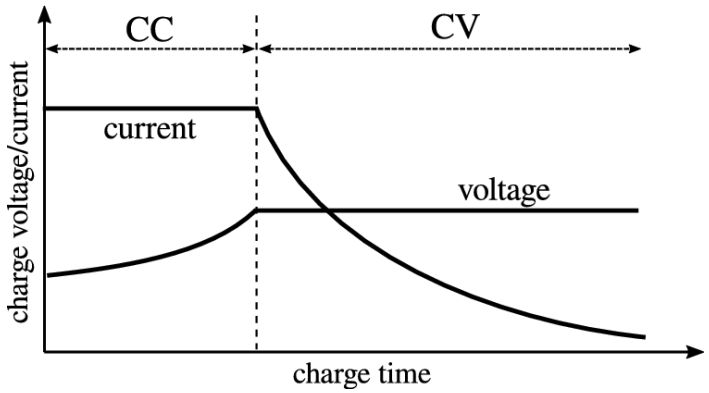

Fig. 3.3. Charge profile of CC-CV charge [6]

Knowing this ratio and the maximum battery voltage, the maximum current that will flow through the output of the converter can be calculated:

$$Imax = \frac{Pmax}{Vmax} = \frac{250\ kW}{820\ V} = 304\ A$$

However, this current is divided among the 20 legs that make up the converter.

This value will be used in Chapter 5 in the subsequent sizing of converters intended to control the charge of the BEB.

3.3 Comparison with the use of a single-leg DC/DC converter

The fact that a multi-leg converter can be more optimal than a single-leg one is primarily due to the scale applied to the power handled by each leg compared to the single-leg converter. By dividing the processed power, the current requirements of the various elements that make up the multi-leg topology (i.e. semiconductors, magnetic elements, capacitors, etc.) are also divided. Thus, in a multi-leg converter it is possible to access devices with lower specifications concerning the currents, such that, in general, they are less voluminous or have better characteristics from the point of view of optimizing their losses (i.e. lower conduction resistances, lower parasitic capacities, etc.) [7].

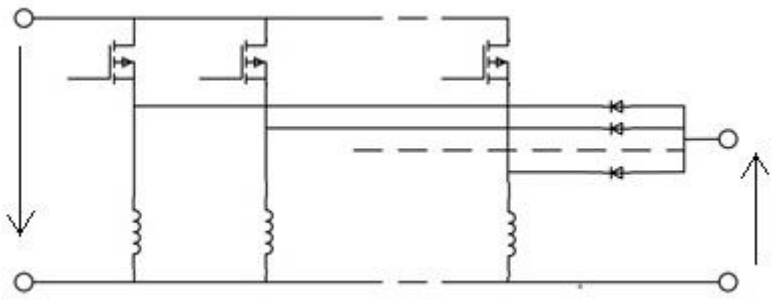

Fig. 3.4. Multi-leg buck-boost type converter

The multi-leg converter allows to relax the maximum current specifications, thus allowing access to devices with lower maximum currents, which proves to be a great advantage in component selection. In the particular case of IGBT-type transistors, it is often possible to select devices with better performance as the maximum current they have to handle is scaled [7].

In addition to the laws of scale, the multi-leg converters also offer other types of advantages, among which we can highlight the possibility of applying interleaving control. However, the use

of this technology by the existing FCS is ruled out because of the complexity of controlling a 20-legs converter.

Another advantage that should be highlighted of the multi-leg converters is their robustness, which enables the multi-leg converter to respond to faults. If one of the legs fails, the multi-leg converter may be able to continue to operate, although with some of its specifications limited by that failure. Conversely, if the power system is based on a single leg, protection and fault tolerance systems must be implemented which increase the cost and complexity of this design. It is important to note that this type of protection and fault tolerance systems are also present in a multi-leg converter (i.e. it is not possible to eliminate these protection systems by adopting a modular design). However, their number and complexity are reduced compared to a single-leg converter [7].

Despite all these advantages, a multi-leg converter also has several disadvantages. In the first place, although the modular converter simplifies the design due to the possibility of simplifying the design of the power leg, it transfers the complexity of the design to the connection system and the control of the legs. Related to the above mentioned, the number of legs that make up the multi-leg converter has a direct impact on the cost, volume and weight of the final power supply, as well as on the complexity of the design. Therefore, calculating the optimal number of legs (and the power to be processed by each leg) adds additional complexity to the design process that must be taken into account given its impact on the final solution [7].

Another disadvantage is the need to balance the currents of each leg. If it is not possible to use a leg that achieves a performance as a current source, the individual current of each leg must be measured in some way. Although only the average current information for each leg is required, this current sensor can be complex and expensive [7].

In a DC/DC converter such as the buck-boost type used in the present FCS at UPNA, the IGBT collector-emitter cut-off voltages and collector currents are too large. Therefore, the advantages provided by the multi-leg converters are what have surely persuaded the designers to select this topology.

4 Possible configurations of the support system

To consider the possibilities of configuring the support system, it should be noted that galvanic isolation will not be taken into account as there will already be a transformer at the head of the charging station. It is also considered that the support system is connected upstream to an AC grid, which is how the future connection of the charging station is planned to be.

It is known that the support system will consist of a 40 kWh ESS and a 50 kW PV system. From this system, the ESS needs to be recharged by the PV but also by the grid because in the future charging station, e-buses will need to be charge even if there is no availability of PV power.

The ESS must be capable of providing a maximum charge power of 175 kW. This number is obtained from [8] in which different energy management strategies are analyzed for the sizing of the FCS with ESS for e-buses, the same FCS that is being designed in this project. In [8] it is determined that using the SOC (state of charge) control strategy, the maximum power that the grid should be able to provide is 75 kW. Bearing in mind that the maximum charge power is 250 kW, it is the ESS that should provide the remaining power (175 kW), since the use of PV has not been included in [8]. This situation of the EES contributing 175 kW would correspond, for the installation to be designed in this project, to the case in which there was no photovoltaic generation and the consumption was maximum.

Having knowledge of the basic operation of the support system and the characteristics of each element, 2 different configurations offered commercially have been observed: AC-coupling and DC-coupling.

4.1 AC-coupling

The first option is to connect the ESS and the PV system separately to the AC grid. This means that each element is connected to the grid through a DC/AC converter. While in the case of the PV system a 50 kW unidirectional inverter will be required, in the case of the ESS it will have to be 175 kW and bidirectional to charge and discharge it. These two elements would be connected through an AC-Bus.

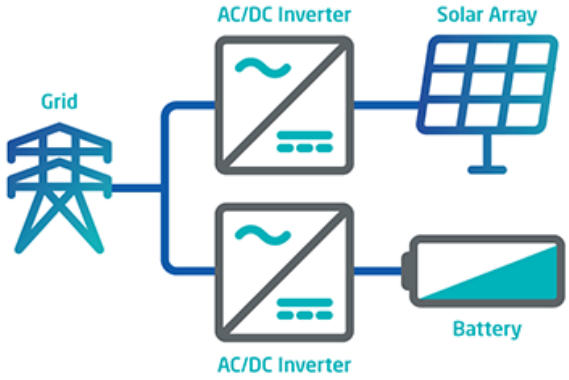

Fig. 4.1. AC-coupled support system [9]

There are many commercial solutions of this type. A proposal from Ingeteam is shown in Fig. 4.1. Specifically, Ingeteam has photovoltaic inverters with powers similar to those required for this converter, as is the case with the INGECONSUN 40TL M480. As far as battery inverters are concerned, those of this brand are of much higher power than the desired one, but others have

been found which would match our requirements, such as the DYNAPOWER MPS-250, of 250 kW.

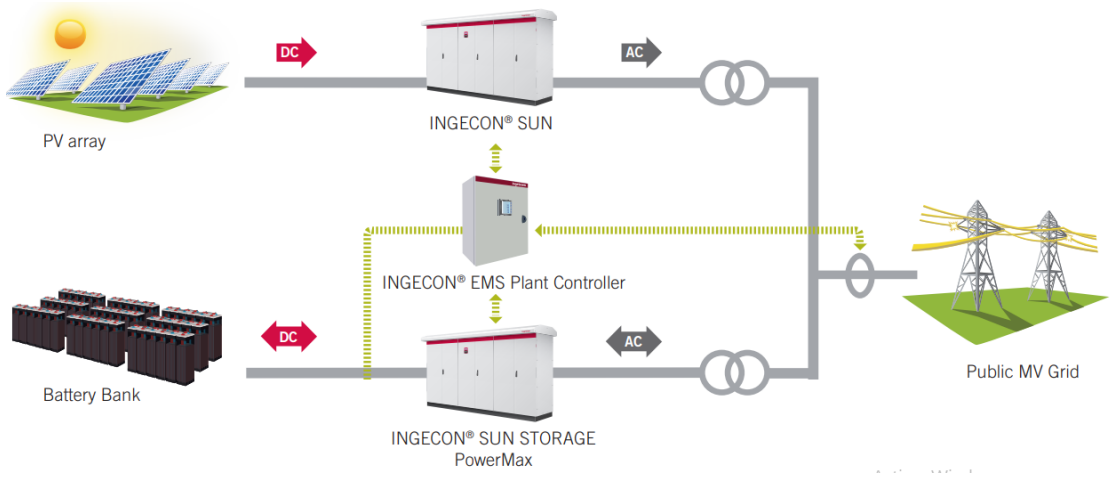

Fig. 4.2. Commercial solution for the AC-coupled support system proposed by Ingeteam

4.2 DC-coupling

There is another alternative for the configuration of the support system, which can be seen in Fig. 4.3. The main difference to the previous option is that in this case only one DC/AC converter is used which acts as a connection between the AC grid and the DC bus. The ESS and the PV system are connected to this DC bus through two DC/DC converters, which should be 175 kW bidirectional and 50 kW unidirectional, respectively. If the maximum consumption mentioned above is to be carried out in alternating mode, then the DC/AC converter must be 175 kW to transfer the power from the BE. On the other hand, if this maximum consumption takes place in the DC-coupling itself, then the DC/AC converter must be 75 kW due to the power requirements explained in the introduction to chapter 4.

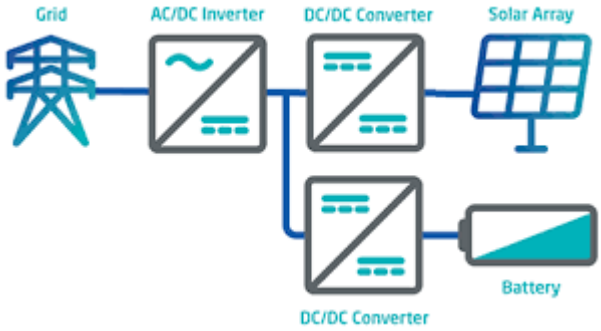

Fig. 4.3. DC-coupled support system. Adapted from [9]

Commercially there are not so many solutions that correspond to this configuration. This is because most commercial solutions that have PV generation and ESS with DC-coupling are not prepared to charge the ESS with energy from the RE, which is indispensable in this application. However, Dynapower offers the configurations shown in Fig. 4.4. with the option of feeding electricity back to the grid but also with the option of charging the ESS with the grid [10].

Fig. 4.4. Commercial solutions of the DC-coupled support system proposed by Dynapower [10]

When comparing architectures in Fig. 4.3 and Fig. 4.4, it can be expected that the architectures in Fig. 4.3 will show a higher efficiency because they have one less converter and therefore fewer losses will occur. However, the possibility of adopting the topologies shown in Fig. 4.4 was ruled out because it is known that control is more difficult by stability problems.

5 Proposed configurations and sizing

This chapter proposes 3 possibilities for the connection of the support system and the charging point. Each of the options is dimensioned including the necessary filters. These sizing are the base for the next chapters to be able to calculate the efficiencies and costs of each configuration.

the proposed topologies have been named configuration 1.1, configuration 1.2, and configuration 2. The first number corresponds to the type of coupling used to interconnect the 3 elements of the system. The number 1 corresponds to use an AC-Bus while the number 2 to a DC-Bus

The sizing of the current FCS is also included in order to compare the proposed configurations with the existing one. This topology has been called configuration 0.

The option of using interleaved converters has not been considered in this chapter. In order to compare these configurations, it has been decided to select the classical topologies. However, Chapter 9 implements the proposed configurations with interleaved converters and calculates the difference in efficiencies and costs from those calculated in this chapter.

5.1 Configuration 1.1

One of the configurations that can be used in a FSC is to use an AC bus structure, as shown in Fig. 5.1. The grid voltage is reduced by using an LF transformer. The secondary windings of this transformer are used as an AC bus to connect each of the components. This would be the equivalent of connecting the support system to the current charging point at UPNA on its 400V AC side. This support system would correspond to that seen in section 4.1.

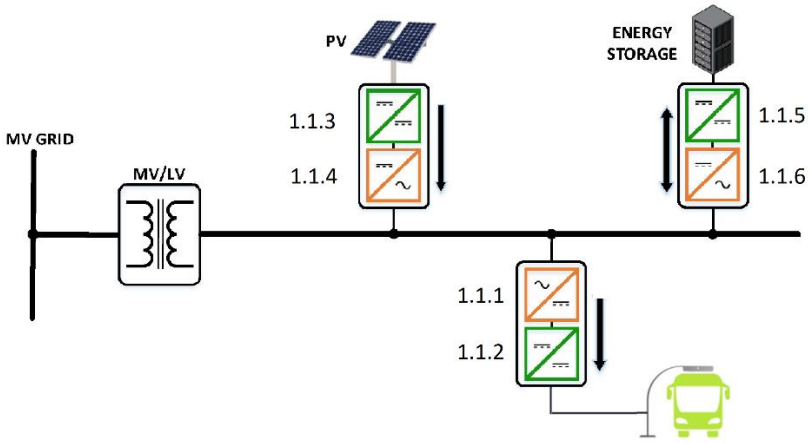

Fig. 5.1. Possibility number 1.1 for the FCS with ESS and PV. Adapted from [11]

A transformer would be placed in the system head to lower the voltage from medium to low voltage, in addition to providing galvanic isolation. For each of the components, an AC/DC converter would be required, connected to the AC bus at a common coupling point. For the ESS the converter should be reversible for charging and discharging while for the PV system and the charging point a unidirectional one is sufficient. For this case in particular, a reversing converter would be required for the PV system and a rectifier for the charging point.

The nominal power of the conversion stages are as follows:

- the maximum power with which the e-bus is recharged is 250 kW, as explained in Chapter 3
- the power of the PV array is 50 kW, as mentioned in Chapter 4
- the nominal power of the ESS conversion stage must be 175 kW, as explained in Chapter 4.

The converters have been numbered, as shown in Fig. 5.1. The numbering will be used in the following sections for sizing.

5.1.1 Recharge point conversion stage

A three-phase unidirectional rectifier is required in the AC/DC stage. The BEB charge is controlled by a unidirectional DC/DC converter. For the DC/DC converter, a buck type converter is sufficient because the rectifier used is a boost type one, meaning that the voltage of the intermediate DC bus between the converters can be increased to a voltage higher than the maximum voltage at which the charge is carried out, which is known to be 820 V. This avoids the use of a buck-boost converter, a type of converter with lower efficiency than a buck converter.

Converter 1.1.1

The following specifications are required for the AC/DC converter:

Parameter	Value
Rated power	250 kW
Rated voltage AC side	400 V (AC)
Rated voltage DC side	1000 V (DC)
Rated current AC side	360 A
Nominal current DC side	250 A
Switching frequency	10 kHz

Table 5.1. Technical characteristics of the converter 1.1.1

Semiconductor Selection

According to the design specifications, SEMiX404GB12E4s has been chosen for power semiconductors. The IGBTs chosen supports 1200V collector-emitter voltage and maximum collector currents of 400A.

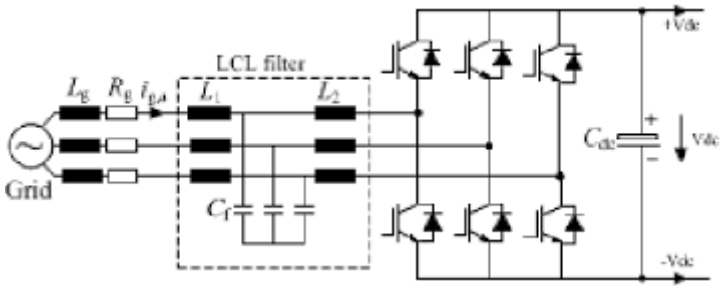

Fig. 5.2. Active rectifier with LCL filter [12]

LCL filter sizing

To calculate the total value of inductance of the filter required for this rectifier, which is assumed to be equal to the sum of the values of the two coils that make up the LCL filter, the following approximate formula has been used:

$$L = \frac{V_{DC}}{6.9\, f_{sw}\, \Delta I_{Lmax}} \quad ,$$

where f_{sw} is the switching frequency of the semiconductors.

In order to calculate the maximum ripple normally admitted in this type of converters, the values of the LC filter of [13] have been used. Thus, using the data in [13] and the formula commented upon, a maximum allowable ripple of 35% of the Inom has been calculated. It is assumed that afterward, the ripple will be lower due to the action of the filter capacitor. In fact, it has been observed through the Bode diagram that the ripple of the LC filter of [13] is 5%, as shown in Fig 5.3.

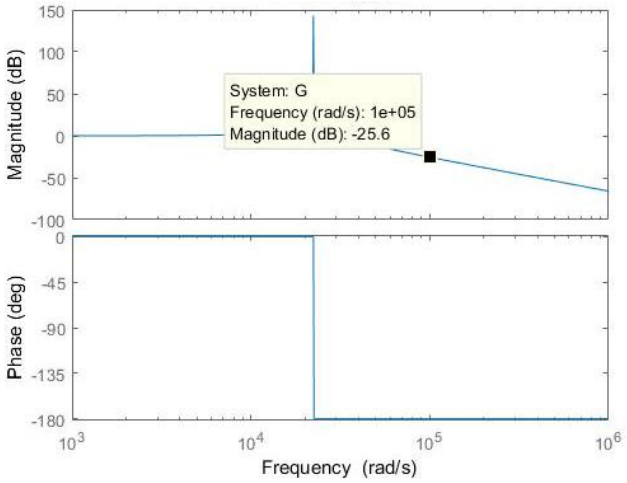

Fig. 5.3. Bode diagram of the proposed LC filter in [13]

Once the maximum ripple desired is defined, the formula already mentioned in this section has been applied again but now with the values of this converter, shown in Table 5.1:

$$L = \frac{V_{DC}}{6.9\, f_{sw}\, \Delta I_{Lmax}} = \frac{1000}{6.9 * 10{,}000 * 0.35 * (\frac{250{,}000}{3 * 230} * \sqrt{2})} = 80.8\ \mu H$$

This is the value corresponding to the sum of the inductances of the LCL filter.

In turn, to determine the ESR (Equivalent Series Resistance) of the coils with which the inductor losses are then calculated, data from [14] have been now used. The ESR of the filter coils of [14] in value per unit has been calculated using as a basis the inductive impedance used in the filter proposed. A value of 1.41 pu. has been obtained. This value has been utilized in the converter to be sized.

To determine the value of the filter capacitor, the formula of the resonance frequency of the LCL filter has been used:

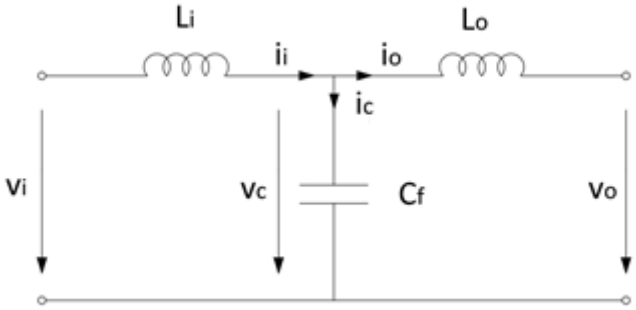

Fig. 5.4. Single-phase LCL filter circuit

$$f_{res} = \frac{1}{2\,\pi} \times \sqrt{\frac{L_i + L_g}{L_i \times L_g \times C_f}}$$

From which it follows:

$$C_f = \frac{1}{4\,\pi^2} \times \frac{L_i + L_g}{L_i \times L_g \times {f_{res}}^2}$$

A resonance frequency of 7117 Hz has been calculated in [14]. That is, a resonance frequency of 44.5% of the switching frequency, a value that has been used in the design of the filter to be dimensioned. Considering that the coils of the LCL filter are equal and half of the calculated value it is necessary a C of:

$$C_f = \frac{1}{4\,\pi^2} \times \frac{40.4E-6 + 40.4E-6}{40.4E-6 \times 40.4E-6 \times 4448^2} = 63.3\ uF$$

To determine the losses that occur in the capacitor, two things are needed to be considered.

It is first necessary to obtain the current that circulates through it. Using Kirchoff's law in the circuit in Figure 5.4, the filter model in the s-plane can be described with the following equations:

$$i_i - i_c - i_o = 0$$

$$v_i - v_c = i_i\ s\ L_i$$

$$v_c - v_o = i_o\ s\ L_o$$

$$v_c = i_c \left(\frac{1}{s\ C_f}\right)$$

Assuming that the grid (Vo) is an ideal voltage source and that for high frequencies it can approach a short circuit, the current flowing through the capacitor results:

$$i_o\ s\ L_o = i_c \left(\frac{1}{s\ C_f}\right) \qquad i_c = i_o s^2\ C_f\ L_o$$

In the second place, it is also necessary to determine the value of the ESR of the capacitor. For this purpose, the ESR of the filter capacitor of [14] has been calculated in value per unit using as a base the conductive impedance used in the filter proposed. A value of 1.57E-3 pu. has been obtained and subsequently utilized in the converter to be sized.

It should be noted that these calculations have subsequently been used in all other DC/AC converter sizing in sections 5.1.2, 5.1.3, 5.2.2 and 5.2.4.

Thus, the characteristic parameters of the LCL filter are as follows:

Parameter	Value
L_i	40.4 uH
ESR Inductance	0.018 Ω
L_o	40.4 uH
Cf	63.3 uF
ESR Capacitance	0.13 Ω

Table 5.2. LCL filter parameters of the converter 1.1.1

Converter 1.1.2

For the DC/DC converter, considering the BEB's recharge voltage values, the characteristics required by the converter are as follows:

Parameter	Value
Type	Unid. Buck type
Rated power	250 kW
Rated input voltage (DC-bus)	1000 V
Rated output voltage	650 V
Minimum and maximum output voltages	420 – 820 V
Nominal input current	250 A
Maximum output current (with Vmax and Pmax)	305 A
Switching frequency	10 kHz

Table 5.3. Technical characteristics of the converter 1.1.2

Semiconductor Selection

According to the design specifications, SKM400GAR12E4has been chosen for power semiconductors. The IGBTs chosen supports 1200V collector-emitter voltage and maximum collector currents of 400A.

Coil sizing

To calculate the value of inductance necessary to obtain a lower current ripple than desired, the general equation of the instantaneous voltage in a coil is employee:

$$V_L = L\frac{di_l}{dt}$$

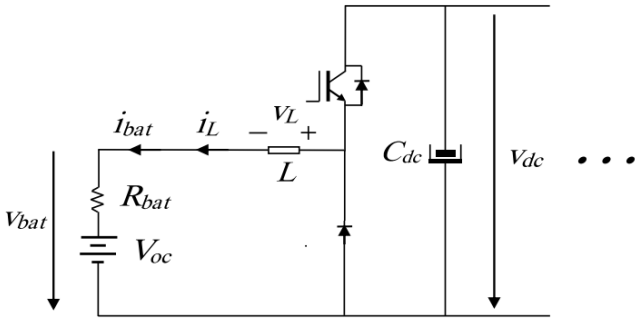

Fig. 5.5. Buck type converter. Adapted from [15]

Considering that during Ton the current flows through the IGBT, the voltage applied to the coil is constant and equal to Vdc-Vbat, as can be seen in Fig 5.5. Therefore, the following formula can be deduced:

$$(V_{dc} - V_{bat}) * T_{on} = L * \Delta i_l$$

$$\Delta i_l = \frac{(V_{dc} - V_{bat}) * T_{on}}{L}$$

Also, in a buck-type converter, the relation between the input-output voltage ratio and the duty cycle is:

$$D = \frac{T_{on}}{T_{off}} = \frac{V_{bat}}{V_{dc}}$$

Thus, it is easily deduced that:

$$T_{on} = \frac{D}{F_{conm}}$$

By linking the two formulas together, it follows that:

$$\Delta i_l = \frac{V_{dc} * (1 - D) * D}{L * F_{conm}}$$

Deriving this formula with respect to D, it is obtained that there is a maximum for D=0.5. Substituting this value and clearing the L, the following formula is obtained:

$$L \geq \frac{V_{dc}}{4 * F_{conm} * \Delta i_{l\,max.}}$$

It has been calculated from the values of [15] that the maximum allowable ripple used in in this type of application is 15 %.

A minimum value of L=546 uH has been calculated considering this allowable ripple and that the current circulating through the coil is the output current (305 A).

To be able to determine the losses that occur in this coil due to the internal resistance, the procedure has been the same as for the previous DC/AC converter. In this case, data from [16] has been used to determine the ESR of the inductive impedance of the converter, obtaining a value of 0.12 pu. This value will be used for the rest of the DC/DC converters in sections 5.1.2 and 5.1.3.

Parameter	Value
L	546 uH
ESR Inductance	0.02 Ω

Table 5.4. Coil parameters of the converter 1.1.2

5.1.2 PV array conversion stage

Two converters are needed in this conversion stage. A boost type converter will raise the output voltage of the PV array. A minimum DC-Bus voltage will then be reached so that the inverter can be connected to the 400 V AC grid. A three-phase unidirectional inverter is required together with an LCL filter for the DC/AC converter. The topology selected for this inverter is the same one as in the charging point rectifier in section 5.1.1, shown in Fig. 5.2.

Converter 1.1.3

In order to define the specifications of the DC/DC converter, it is necessary to obtain the output values of the voltage and current of the photovoltaic system. For this purpose, the values from INGECON SUN 50 converter datasheet have been used. It is a 50 kW photovoltaic inverter that incorporates a boost type converter.

Parameter: Input (DC)	Value
Recommended PV array power range	52 - 65 kWp
Voltage range MPPT	405 - 750 V

Table 5.5. Technical specifications from the datasheet of the INGECON SUN 50

The next step would be to size the converter 1.1.3 using the values in Table 5.5. The specifications required for this converter are shown in Table 5.6

Parameter	Value
Type	Unid. Boost type
Rated power	50 kW
Minimum MPPT input voltage	405 V
Maximum MPPT input voltage	750 V
Rated output voltage	1000 V
Maximum input current	123 A
Rated output current	50 A
Switching frequency	20 kHz

Table 5.6. Technical characteristics of the converter 1.1.3

The converter 1.1.4 sizing in this same section justifies the rated output voltage value in table 5.6

Semiconductor Selection

According to the design specifications, SEMiX151GAL12E4s has been chosen for power semiconductors. The IGBTs chosen supports 1200V collector-emitter voltage and maximum collector currents of 150 A.

Coil sizing

Starting from the same equation as in section 5.1.1 for sizing the coil of a DC/DC converter:

$$V_l = L\frac{di_l}{dt}$$

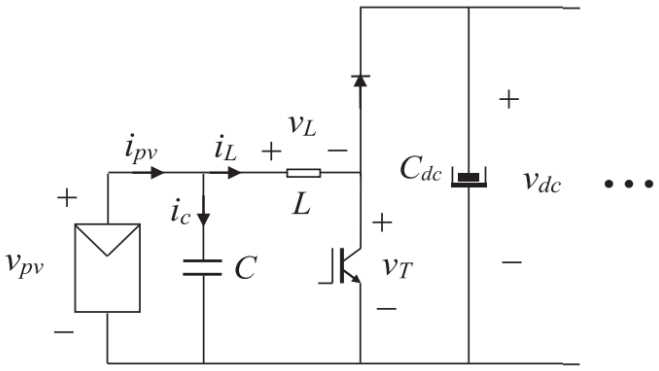

Fig. 5.6. Boost type converter connected to a PV array [17]

During Ton the current is flowing through the IGBT. The voltage applied to the coil is constant and equivalent to the input voltage Vpv. Therefore:

$$V_{pv} * T_{on} = L * \Delta i_l$$

$$V_{pv} = \frac{L * \Delta i_L * F_{conm}}{D}$$

Therefore, in order not to exceed the maximum allowable ripple, it will be necessary a coil with a value of inductance of:

$$L \geq \frac{V_{pv} * D_{max}}{F_{conm} * \Delta i_{L\,max.}}$$

However, in the boost type converter studied, the input value is variable, so the minimum inductance required is calculated as a function of the output voltage (Vdc), which in this case is constant:

$$L \geq \frac{V_{dc} * (1 - D) * D}{F_{conm} * \Delta i_{L\,max.}}$$

To obtain the work cycle with which the maximum ripple is produced, the previous formula is derived with respect to D and is equal to 0, obtaining a value of D=0.5

$$L \geq \frac{V_{dc}}{4 * F_{conm} * \Delta i_{L\,max.}}$$

To know the maximum permissible ripple typical in this type of applications, from the values of [17] a maximum ripple of 37% has been calculated by applying the formulas demonstrated:

$$i_{L\,nom.} = 18.9\ A$$

$$\Delta i_{L\,max.} = \frac{V_{dc}}{4 * F_{conm} * L} = \frac{340\ V}{4 * 16000Hz * 750E-6} = 7.08\ A$$

$$\frac{6.56\ A}{18.9\ A} = 0.37$$

Thus, using the 0.37 ripple value, the minimum value of inductance calculated for the boost type converter is:

$$L \geq \frac{V_{dc}}{4 * F_{conm} * \Delta i_{L\,max.}} = \frac{1000\,V}{4 * 20000Hz * (123\,A * 0.37)} = 275\,uH$$

Parameter	Value
L	275 uH
ESR Inductance	0.01 Ω

Table 5.7. Coil parameters of the converter 1.1.3

For this converter, the losses produced in the capacitor located in parallel with the PV array will be neglected due to the small impact.

Converter 1.1.4

The following specifications are required for the AC/DC converter:

Parameter	Value
Rated power	50 kW
Rated voltage AC side	400 V (AC)
Rated voltage DC side	1000 V (DC)
Rated current AC side	72 A
Rated current DC side	100 A
Switching frequency	20 kHz

Table 5.8. Technical characteristics of the converter 1.1.4

The need for 1000 V on the DC side is because this inverter is a buck-type converter in which a minimum DC voltage is required, which can be calculated from Fig 5.7:

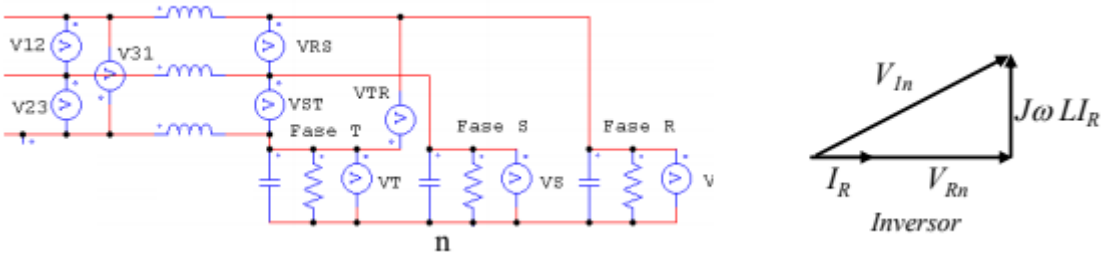

Fig. 5.7. AC side of the three-phase inverter and phase diagram of the voltages [18]

As can be seen in Fig. 5.7, the following relationship is fulfilled:

$$V_{1n} = \sqrt{{V_{Rn}}^2 + (j\ w\ L\ I_R)^2}$$

Besides, it is known that a three-phase inverter meets that:

$$(V_{1n})_{max} = \frac{V_{in}}{2\sqrt{2}\,V_{pt}} M_{max}\,,$$

where M is the desired limit value of the modulator.

From these two formulas, it can be obtained that the minimum necessary DC voltage is:

$$(V_{in})_{min} = \frac{\sqrt{8}\,V_{pt}\sqrt{{V_{Rn}}^2 + (w\ L\ I_R)^2}}{M_{max}}$$

By approximating the following values:

- L = 200 uH
- $\frac{M_{max}}{V_{pt}}$ = 0.8
- the AC voltage can be up to 10% higher than its nominal value

it is calculated a minimum necessary DC voltage of 894 V. This is the reason why it was decided to select a DC-Bus voltage between the inverters and the DC/DC converters of 1000 V.

Semiconductor Selection

According to the design specifications, SEMiX151GB12E4s has been chosen for power semiconductors. The IGBTs chosen supports 1200V collector-emitter voltage and maximum collector currents of 150 A

LCL filter sizing

Using the formula mentioned in section 5.1.1 and the same maximum permissible ripple of 35%:

$$L = \frac{V_{DC}}{6.9\, f_{sw}\, \Delta I_{Lmax}}$$

A minimum value of L=203 uH is obtained. The methodology to obtain the value of the capacitor has been the same as in section 5.1.1. Therefore, the characteristic parameters of the filter to be used are the following:

Parameter	Value
L_i	101 uH
ESR Inductance	0.045 Ω
L_o	101 uH
Cf	6.3 uF
ESR Capacitance	0.012 Ω

Table 5.9. LCL filter parameters of the converter 1.1.4

5.1.3 ESS conversion stage

A bidirectional conversion stage will be required to discharge and charge the battery.

Converter 1.1.5

In order to define the specifications of the DC/DC converter, the voltage and current values of the ESS where this converter will be connected are needed. The assumptions made are based on the values of the lithium-ion batteries used in the current city buses mentioned in chapter 2:

- the minimum voltage is 400 V and the maximum voltage is 600 V.
- the nominal voltage is 500 V.
- the nominal power can be given with the minimum voltage, even though this may not be the case and the converter is being over-dimensioned.

Therefore, taking into account the minimum DC voltage calculated in 5.1.2 to achieve the desired 400 V AC output, a bi-directional converter with the following technical characteristics would be required:

Parameter	Value
Type	Bidirect. Buck-boost type
Rated power	175 kW

Rated input voltage	1000 V
Output voltage range (battery side)	400 - 600 V
Rated input current	175 A
Maximum output current (battery side)	440 A
Switching frequency	10 kHz

Table 5.10. Technical characteristics of the converter 1.1.5.

Semiconductor Selection

According to the design specifications, SEMiX603GB12E4p has been chosen for power semiconductors. The IGBTs chosen supports 1200V collector-emitter voltage and maximum collector currents of 600 A.

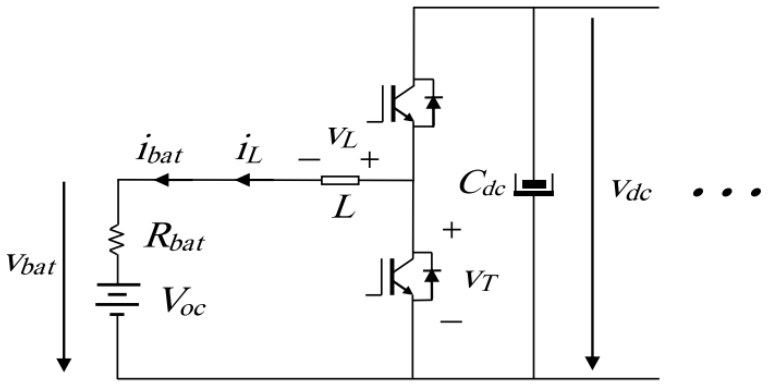

Fig. 5.8. Bidirectional converter connected to the ESS [19]

Coil sizing

It is known that, regardless of the mode of operation of the bi-directional converter, the minimum inductance is calculated with the formula already deduced in section 5.1.1:

$$L \geq \frac{V_{dc}}{4 * F_{conm} * \Delta i_{L\,max.}}$$

As has already been done for the previous converters in sections 5.1.1 and 5.1.2, the maximum allowable ripple in similar applications has been calculated. For this case, the ripple of [19] have been calculated. In this paper a ripple of up to 15% is allowed when the bi-directional converter is in buck but also in boost mode. With this value and those in Table 5.10, the minimum value of L obtained is:

$$L \geq \frac{V_{dc}}{4 * F_{conm} * \Delta i_{L\,max.}} = \frac{1000\,V}{4 * 10000Hz * (440 * 0.15)} = 379\,uH$$

Therefore, the characteristics of the coil will be as follows:

Parameter	Value
Inductancia nominal	379 uH
ESR Inductance	0.014 Ω

Table 5.11. Coil parameters of converter 1.1.5

Converter 1.1.6

For the AC/DC converter, a three-phase bidirectional converter is required together with an LCL filter. The topology selected for this inverter is the same one as in the charging point rectifier in section 5.1.1, shown in Fig. 5.2. The following specifications are required:

Parameter	Value
Rated power	175 kW
Rated voltage AC side	400 V (AC)
Rated voltage DC side	1000 V (DC)
Rated current AC side	255 A
Rated current DC side	270 A
Switching frequency	10 kHz

Table 5.12. Technical characteristics of converter 1.1.6

Semiconductor Selection

According to the design specifications, SEMiX404GB12E4s has been chosen for power semiconductors. The IGBTs chosen supports 1200V collector-emitter voltage and maximum collector currents of 400 A.

LCL filter sizing

Again, with the formula already used in section 5.1.1:

$$L = \frac{V_{DC}}{6.9\, f_{sw}\, \Delta I_{Lmax}}$$

A minimum value of L=115 uH is obtained. The methodology to obtain the value of the capacitor has been the same as in sections 5.1.1 and 5.1.2 for converters 1.1.1 and 1.1.4. Therefore, the characteristic parameters of the LCL filter to be used are the following:

Parameter	Value
L_i	57 uH
ESR Inductance	0.025 Ω
L_o	57 uH
Cf	44.5 uF
ESR Capacitance	0.089 Ω

Table 5.13. LCL filter parameters of the converter 1.1.6

5.2 Configuration 1.2

This option corresponds to the use of an AC-Bus as in configuration 1.1. The difference is that the support system is connected to AC-Bus via only one AC/DC converter. This is because the PV array and the ESS are connected by means of a DC-coupling, as shown in Fig. 5.9

For both the charging point and the support system there is an AC/DC stage and a DC/DC stage. These stages may be different depending on whether the power flow is unidirectional or bidirectional, and on the need to raise or lower the voltage. It is again assumed that the transformer is 13.2 kV/400 V as it is at present, so the AC bus has a voltage of 400 V.

The component powers that make up the installation determined in section 5.1 have been used to select the converter power ratings.

The converters have been numbered, as shown in Fig. 5.9.

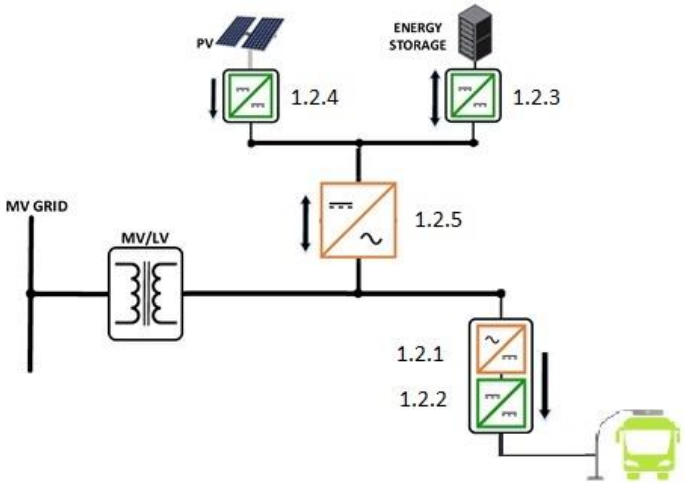

Fig. 5.9. Possibility number 1.2 for the FCS with ESS and PV. Adapted from [11]

5.2.1 Charging point conversion stage

Converters 1.2.1 and 1.2.2 are of identical parameters to the already dimensioned 1.1.1 and 1.1.2.

5.2.2 Support system conversion stage

Converter 1.2.3

The necessary characteristics of this converter are identical to the converter 1.1.5.

Converter 1.2.4

The necessary characteristics of this converter are identical to the converter 1.1.3.

Converter 1.2.5

In the AC/DC stage, a three-phase bi-directional rectifier is required to link the AC-bus and the DC coupling of the support system. A converter of the same type as model 1.1 with an LCL filter has been selected.

If the EES is to be charged simultaneously by the grid and the PV system, the power of the converter must be 225 Kw.

The technical specifications would be as follows:

Parameter	Value
Maximum power	225 kW
Rated voltage AC side	400 V (AC)
Rated voltage DC side	1000 V (DC)
Maximum current AC side	326 A
Maximum current DC side	225 A
Switching frequency	10 kHz

Table 5.14. Technical characteristics of converter 1.2.5

Semiconductor Selection

According to the design specifications, SEMiX404GB12E4s has been chosen for power semiconductors. The IGBTs chosen supports 1200V collector-emitter voltage and maximum collector currents of 400 A.

LCL filter sizing

With the formula already used in section 5.1.1 for the converter 1.1.1:

$$L = \frac{V_{DC}}{6.9\, f_{sw}\, \Delta I_{Lmax}}$$

A minimum value of L=90 uH is obtained considering the values of Table 5.14 and the same maximum allowable ripple as in section 5.1.1. for the converter 1.1.1. Therefore, the characteristic parameters of the LCL filter to be used are the following:

Parameter	Value
L_i	45 uH
ESR Inductance	0.02 Ω
L_o	45 uH
Cf	56.8 uF
ESR Capacitance	0.11 Ω

Table 5.15. LCL filter parameters of the converter 1.2.5

5.3 Configuration 2

This option corresponds to the use of the dc-coupling support system in section 4.1. In the same coupling it would be connected the recharging point, as shown in Fig. 5.10. That is, the topology corresponds to using a DC-Bus in which the different components are coupled through a DC/DC stage.

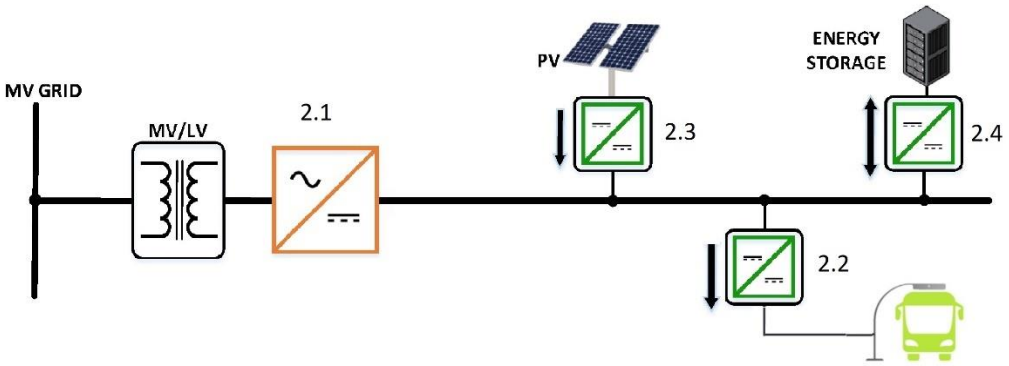

Fig. 5.10. Possibility number 2 for the FCS with ESS and PV. Adapted from [11]

As in configurations 1.1 and 1.2, a transformer would provide galvanic isolation between the grid and the whole installation, as shown in Fig. 5.10. However, a single AC/DC stage is now used to form an intermediate DC-Bus. The DC/DC converters would control each of the 3 components that make up the installation. As in the previous options, this stage may vary depending on whether the power flow is desired to be unidirectional or bidirectional, and on the need to raise or lower the voltage. And for the same reason analyzed in section 5.1.1, a DC-Bus voltage of 1000 V is imposed so that the AFE converter can operate as an inverter.

The component powers that make up the installation determined in section 5.1 have been used to select the converter power ratings. It should also be noted that the maximum power required from the grid in case of not having PV power is 75 kW

The converters have been numbered, as shown in Fig. 5.10

5.3.1 Charging point conversion stage

The 2.2 converter is a unidirectional DC/DC converter with the same characteristics as converter 1.1.2.

5.3.2 PV array conversion stage

The 2.3 converter is a unidirectional DC/DC boost type converter with the same characteristics as converter 1.1.3.

5.3.3 ESS Conversion Stage

The 2.4 converter is a bi-directional DC/DC buck-boost type converter with the same characteristics as converter 1.1.5.

5.3.4 Rectifier stage – Converter 2.1

This converter is the link between the AC grid and the DC-Bus. The selected topology is the one used for converter 1.1.1 in section 5.1.1, corresponding to the Fig. 5.2. The main reason why this bidirectional topology has been selected is that this topology allows the converter to feed power back to the internal grid of the UPNA through to the support system. The characteristics of this converter are as follows:

Parameter	Value
Rated power	75 kW
Rated voltage AC side	400 V (AC)
Rated voltage DC side	1000 V (DC)
Rated current AC side	110 A
Rated current DC side	75 A
Switching frequency	16 kHz

Table 5.16.. Technical characteristics of the converter 2.1

Semiconductor Selection

According to the design specifications, SEMiX151GB12E4s has been chosen for power semiconductors. The IGBTs chosen supports 1200V collector-emitter voltage and maximum collector currents of 150 A.

LCL filter sizing

With the formula already used in section 5.1.1 for the converter 1.1.1:

$$L = \frac{V_{DC}}{6.9\, f_{sw}\, \Delta I_{Lmax}}$$

A minimum value of L=166 uH is obtained considering the values of Table 5.16 and the same maximum allowable ripple as in section 5.1.1. for the converter 1.1.1. Therefore, the characteristic parameters of the LCL filter to be used are the following:

Parameter	Value
L_i	83 uH
DC Resistance	0.036 Ω
L_o	83 uH
C	12 uF
ESR Capacitance	0.024 Ω

Table 5.17. LCL filter parameters of the converter 2.1

5.4 Configuration 0

The topology of the current FCS is composed of an LF transformer, a rectifier and a DC/DC converter that controls the charge, as shown in Fig. 5.11.

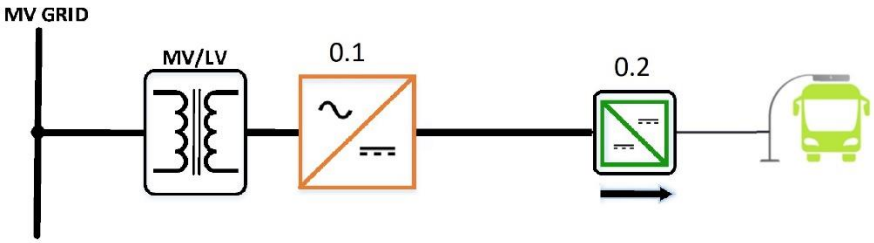

Fig. 5.11. Topology of the present FCS at UPNA

The function of the transformer is none other than to lower the MV (13.2 kV) to LV (400 V) in addition to providing galvanic isolation. It has a power of 300 kVA, since 250 kW is the maximum power with which the charge is carried out. As in this current topology there is no support system, it is the grid the one that provides the necessary power to carry out the e-Bus charge at all times.

As it is learned from chapter 2, the 0.1 converter is an active rectifier. The 0.2 converter is a DC/DC converter with 20 identical parallel modules.

However, in order to compare in equal conditions the proposed configurations with the current topology in terms of efficiency and costs, it has been considered that the converters that make up configuration 0 are the same as those proposed for the conversion stage of the charging point of the configurations with AC-Bus (configurations 1.1 and 1.2).

5.4.1 Rectifier conversion stage – Converter 0.1

The 0.1 converter is an active rectifier converter with the same characteristics as converter 1.1.1.

5.4.2 Charging point conversion stage – Converter 0.2

The 0.2 converter is a buck type rectifier converter with the same characteristics as converter 1.1.2.

6 Power losses and efficiency of the proposed configurations

The first two sections of this chapter explain the procedure followed for calculating losses depending on the type of converter. The results obtained and their analysis are included in sections 6.3 and 6.4, respectively.

6.1 Diode and IGBT energy losses

6.1.1 Diode losses

There are two different types of diode losses:

- Conduction losses. Assuming constant I_F during the driving time of the diode ($t_{ON(diode)}$):

$$p_{con} = V_F(I_F)\, I_F$$

$$E_{con} = p_{con} * t_{ON(diode)}$$

  The voltage V_F is obtained from the graphs on the manufacturer's datasheets.
- Switching losses: The turn-on losses are negligible. The reverse recovery losses (E_{rr}) depend on the voltage (V_F), current (I_F), control voltage (V_{GE}) and door resistance (R_G). They can be obtained from the manufacturer's data sheets by passing it on to the real conditions:

$$E_{rr}(V_F, I_F, R_G) \approx E_{rr}\left(V_{Fref}, I_{Fref}, R_{Gref}\right) \left(\frac{V_F}{V_{Fref}}\right)^{0.6} \left(\frac{I_C}{I_{Cref}}\right) K_{RGrr}$$

  The constant K_{RGrr} has been taken as 1.

To work with the graphs of the datasheets, shown in Appendix B, EXCEL has been used to calculate the polynomial function that resembles these graphs.

6.1.2 IGBT losses

There are two different types of IGBT losses:

- Conduction losses: As with the diode, assuming constant I_C during the IGBT's driving time:

$$p_{con} = V_{CEsat}(I_C)\, I_C$$

$$E_{con} = p_{con} * t_{ON(IGBT)}$$

  The voltage V_{CEsat} is obtained from the graphs on the datasheets.
- Switching losses: The energy lost on each switching (E_{ON} and E_{OFF}) depends on the voltage (V_{CE}), current (I_C), control voltage (V_{GE}) and door resistance (R_G). It can be obtained from the manufacturer's datasheets by passing them on to the real conditions:

$$E_{on}(V_{CE}, I_C, R_G) \approx E_{on}\left(V_{CEref}, I_{Cref}, R_{Gref}\right) \left(\frac{V_{CE}}{V_{CEref}}\right)^{1.3} \left(\frac{I_C}{I_{Cref}}\right) K_{RGon}$$

$$E_{off}(V_{CE}, I_C, R_G) \approx E_{off}\left(V_{CEref}, I_{Cref}, R_{Gref}\right) \left(\frac{V_{CE}}{V_{CEref}}\right)^{1.3} \left(\frac{I_C}{I_{Cref}}\right) K_{RGoff}$$

Constants K_{RGon} y K_{RGoff} have been taken as 1.

To work with the graphs of the datasheets, shown in Appendix B, EXCEL has been used to calculate the polynomial function that resembles these graphs.

6.2 Converters losses

6.2.1 Active rectifier converter

The losses produced in the semiconductor that makes up an inverter like the one in Fig. 6.1 can be calculated through the analysis of a single phase.

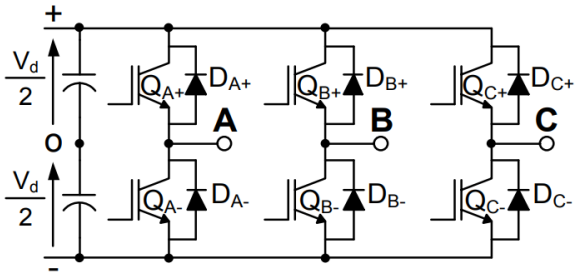

Fig. 6.1. Active rectifier converter

Considering a single phase, the iA current will pass through the A terminal by a single semiconductor depending on the state of the branch and the direction of the current:

$$s_{A+}\ \text{TLI}\begin{cases} =0=\text{Est. 2} \Rightarrow V_{Ao,\text{TLI}}=-\dfrac{V_d}{2} & \begin{cases} i_A>0\Rightarrow D_{A-} \\ i_A<0\Rightarrow Q_{A-} \end{cases} \\ =1=\text{Est. 1} \Rightarrow V_{Ao,\text{TLI}}=\dfrac{V_d}{2} & \begin{cases} i_A>0\Rightarrow Q_{A+} \\ i_A<0\Rightarrow D_{A+} \end{cases} \end{cases},$$

where s_{A+} is the control signal for the transistor Q_{A+} (complementary to Q_{A-}), V_d is the DC-Bus voltage and V_{Ao} is the phase voltage with respect to the midpoint of the bus.

The use of complementary switching signals implies the use of certain possible states in a phase, as shown in Table 6.1.

State	Q_{A+}	Q_{A-}	Analysis
0	OFF	OFF	Only in transitions
1	**ON**	**OFF**	**Valid state**
2	**OFF**	**ON**	**Valid state**
3	ON	ON	Not allowed

Table 6.1. Valid states of phase A

For the calculation of losses, only the semicycle in which the current is positive has been considered. This is because the losses on the other half of the cycle are the same.

The losses have been calculated for each switching period by calculating the duty cycle and the current circulating in the phase. For the calculation of this current, the average value of the currents at the beginning and the end of the switching period has been calculated, considering it constant.

In addition, in order to define the losses in the other two phases, it is enough to multiply the losses of the semiconductors by 3, since the losses for these phases are exactly the same as those of the already calculated branch.

Conduction losses

In a positive semi cycle for a phase, driving losses occur in Q_{A+} during Ton and in D_{A-} during Toff. It will be necessary to calculate the duty cycle and current for each switching period.

Moreover, associated to these conduction losses, it is necessary to add the losses produced in the ESR of the coil and the capacitor. The ESR values have been previously calculated in chapter 5. While the converter current itself on the AC side flows through the coil, the current that flows through the capacitor has also been determined in chapter 5 by means of the single phase diagram of the LCL filter.

Switching Losses

The commutations that occur on a branch in a switching period when the current is outgoing are:

Conm.	Transition	Switch ON	Switch OFF
0	1 -> 2	Q_{A+}	D_{A-}
1	2 -> 1	D_{A-}	Q_{A+}

Table 6.2. Branch switches in a switching period

Thus, switching losses for a positive current switching period are caused by an IGBT switching on and off, and a diode switching off.

Total Losses

The average of the total losses can be calculated considering that the total losses have been calculated for half a period (0.01 s at 50 Hz mains frequency):

$$P = \frac{1}{0.01} \sum_{k=Tconm}^{0.01-Tconm} (P_{on}(k) + P_{sw}(k))$$

6.2.2 DC/DC converter

The calculation of losses for a DC/DC converter is more straightforward, since the current that flows through it is constant.

First, the duty cycle with which the converter is operating must be calculated, value that can be determined with the input-output voltage ratio of the converter.

While the DC-Bus voltages are constant for all DC/DC converters, the voltages on the other side are not, since voltages of the Li-ion batteries vary depending on the state of charge, as does the output voltage of the PV array. For the batteries, it has been considered that the voltages are constant and equal to the nominal one, while for the PV array the voltage is the minimum that guarantees to be in the MPPT.

Finally, the already mentioned formulas of losses in IGBTs and diodes have been applied considering the maximum current that can circulate through the semiconductors and bearing in mind their different graphs in the datasheets. Losses in the ESR of the coil have also been calculated.

6.3 Power losses of each configuration

MATLAB software was used to calculate the losses produced in the converters of each of the topologies. The scripts are listed in Appendix A.1. The procedure was as follows.

To begin with, for each of the proposed topologies, the calculations have been repeated 5 times depending on the available photovoltaic power (P_{PV}) for values of 100%, 75%, 50%, 25% and 0%.

The period in which the losses have been analyzed is divided into two subperiods. The first one is the time of duration of the BEB recharge, data obtained from Fig. 3.1 with a value of 210 seconds. The second subperiod is the time between recharges of the e-buses, with a value of 560 seconds. This value has been obtained considering that the total energy supplied by the grid and the photovoltaic in both subperiods (constant power of 75 kW) is equal to the energy of the BEB charge, without considering the energy losses.

Thus, there are 2 operating modes in the period analysed: a first subperiod in which the ESS is discharged and the BEB is recharged, and a second one in which the ESS is recharged. The total duration of operation of the system in which the losses have been analyzed is 770 seconds (560s + 210s).

While the conversion stages of the PV array work with the same power regardless of the operating mode, for the ESS conversion stages and the recharge point it is necessary to differentiate the two phases.

For the charging phase of the BEB charge, the charging profile shown in Fig. 3.1 was used and is named P_{cp} (charging point power). It has been considered a constant recharging power for fractions of a second.

6.3.1 Configuration 1.1

This topology is shown in Fig. 5.1. It has been considered that the power handled by the ESS conversion stage during the recharge of the BEB ($P_{ESS(discharging)}$), which is the power of converters 1.1.5 and 1.1.6 ($P_{1.1.5}$, $P_{1.1.6}$), is equal to the charging profile in Fig. 3.1 but 75 kW lower. This 75 kW corresponds to the power that will be provided by the PV array in addition to the grid (P_{grid}).

$$P_{ESS(discharging)} = P_{1.1.5} = P_{1.1.6} = P_{cp} - (P_{PV} + P_{grid}) = P_{cp} - 75\ \text{kW}$$

During the subperiod in which the BEB is not recharged and it is the ESS that is recharged, the power of this conversion stage is 75 kW. This 75 kW is the power provided by the PV array in case there is power PV availability in addition to the contribution of the grid:

$$P_{ESS(charging)} = P_{1.1.5} = P_{1.1.6} = P_{PV} + P_{grid} = 75\ \text{kW}$$

On the other hand, the power handled by the PV array conversion stage is always the one corresponding to the existing availability of PV power, regardless of which subperiod is analyzed.

The power that flows through the charging point conversion stage will be 0 when it is the ESS that is being recharged and equal to the charging profile in Fig. 3.1 when it is the BEB that is being recharged.

The results obtained are as follows:

Converter ref.	PV power (kW)	Subperiod (charging the BEB or ESS)	Input power (kW)	Power losses (kW)	Input energy (kWh)	Energy losses (kWh)	Efficiency
1.1.1	-	BEB	197.72	4.634	11.53	0.270	97.66
		EES	0	0	0	0	-
1.1.2	-	BEB	197.72	4.246	11.53	0.248	97.85
		EES	0	0	0	0	-
1.1.3	0	both (const. power)	0	0	0	0	-
	12,5	both (const. power)	12.50	1.102	2.67	0.236	91.19
	25	both (const. power)	25.00	1.481	5.35	0.317	94.08
	37,5	both (const. power)	37.50	1.890	8.02	0.404	94.96
	50	both (const. power)	50.00	2.328	10.69	0.498	95.34
1.1.4	0	both (const. power)	0	0	0	0	-
	12,5	both (const. power)	12.50	1.508	2.67	0.323	87.94
	25	both (const. power)	25.00	1.712	5.35	0.366	93.15
	37,5	both (const. power)	37.50	1.952	8.02	0.418	94.79
	50	both (const. power)	50.00	2.228	10.69	0.477	95.54
1.1.5	-	BEB	122.72	2.807	7.16	0.164	97.71
		EES	75.00	0.979	11.67	0.152	98.70
1.1.6	-	BEB	122.72	2.978	7.16	0.174	97.57
		EES	75.00	2.045	11.67	318	97.27

Table 6.3. Energy losses, power losses and efficiency of each converter in configuration 1.1

PV power (kW)	Total energy losses (kWh)	Power losses charging the BEB(kW)	Power losses charging the ESS (kW)
0	1.326	14.664	3.023
12,5	1.884	17.273	5.632
25	2.009	17.857	6.216
37,5	2.147	18.506	6.865
50	2.300	19.220	7.579

Table 6.4. Total energy and power losses of the configuration 1.1 depending on the PV power

6.3.2 Configuration 1.2

This topology is shown in Fig. 5.9. The power flowing through the stationary battery conversion stage (in this configuration corresponding to the converter 1.2.3) is that determined in section 6.3.1. The power handled by the converter 1.2.5 during the recharge of the BEB ($P_{1.2.5(discharging\ ESS)}$) is:

$$P_{1.2.5(discharging\ ESS)} = P_{1.2.4} + P_{1.2.3} = P_{PV} + (P_{cp} - 75\ \text{kW})$$

While during the recharge of the ESS, the power handled by this converter is

$$P_{1.2.5(charging\ ESS)} = P_{grid} = P_{1.2.3} - P_{1.2.4} = 75\ \text{kW} - P_{PV}$$

For the rest of the converters in this topology, the considerations made are the same as for the converters in 1.1 configuration in section 6.3.1.

The results obtained are as follows:

Converter ref.	PV power (kW)	Subperiod (charging of BEB or ESS)	Input power (kW)	Power losses (kW)	Input energy (kWh)	Energy losses (kWh)	Efficiency
1.2.1	-	BEB	197.72	4.634	11.53	0.270	97.66
		EES	0	0	0	0	-
1.2.2	-	BEB	197.72	4.246	11.53	0.248	97.85
		EES	0	0	0	0	-
1.2.4	0	both (const. power)	0	0	0	0	-
	12.5	both (const. power)	12.50	1.102	2.67	0.236	91.19
	25	both (const. power)	25.00	1.481	5.35	0.317	94.08
	37.5	both (const. power)	37.50	1.890	8.02	0.404	94.96
	50	both (const. power)	50.00	2.328	10.69	0.498	95.34
1.2.5	0	ESS	75.00	2.000	11.67	0.31	97.33
	12.5	ESS	62.50	1.820	9.72	0.28	97.09
	25	ESS	50.00	1.653	7.78	0.26	96.69
	37.5	ESS	37.50	1.500	5.83	0.23	96.00
	50	ESS	25.00	1.361	3.89	0.21	94.55
	0	BEB	122.72	2.851	7.16	0.166	97.68
	12.5	BEB	135.22	3.093	7.89	0.180	97.71
	25	BEB	147.72	3.348	8062	0.195	97.73
	37.5	BEB	160.22	3.615	9035	0.211	97.74
	50	BEB	172.72	3.895	10.08	0.227	97.74
1.2.3	-	BEB	122.72	2.807	7.16	0.164	97.71
		EES	75.00	0.979	11.67	0.152	98.70

Table 6.5. Energy losses, power losses and efficiency of each converter in configuration 1.2

PV power (kW)	Total energy losses (kWh)	Power losses charging the BEB(kW)	Power losses charging the ESS (kW)
0	1.311	14.537	2.979
12.5	1.533	15.881	3.900
25	1.603	16.515	4.113
37.5	1.682	17.192	4.369
50	1.771	17.909	4.668

Table 6.6. Total energy and power losses of the configuration 1.2 depending on the PV power

6.3.3 Configuration 2

This topology is shown in Fig.5.10. The power handled by the inverter in this topology (P2.1) during the recharge of the BEB and during the recharge of the ESS is:

$$P_{2.1} = P_{grid} = 75\ \text{kW} - P_{PV}$$

For the rest of the converters in this topology, the considerations made are the same as for the converters in the 1.1 configuration in section 6.3.1.

The results obtained are as follows:

Converter ref.	PV power (kW)	Subperiod (charging of BEB or ESS)	Input power (kW)	Power losses (kW)	Input energy (kWh)	Energy losses (kWh)	Efficiency
2.2	-	BEB	197.72	4.246	11.53	0.248	97.85
		EES	0	0	0	0	-
2.4	-	BEB	122.72	2.807	7.16	0.164	97.71
		EES	75.00	0.979	11.67	0.152	98.70
2.3	0	both (const. power)	0	0	0	0	-
	12.5	both (const. power)	12.50	1.102	2.67	0.236	91.19
	25	both (const. power)	25.00	1.481	5.35	0.317	94.08
	37.5	both (const. power)	37.50	1.890	8.02	0.404	94.96
	50	both (const. power)	50.00	2.328	10.69	0.498	95.34
2.1	0	both (const. power)	75.00	2.351	16.04	0.503	96.86
	12.5	both (const. power)	62.50	2.064	13,37	0.442	96.70
	25	both (const. power)	50.00	1.806	10.69	0.386	96.39
	37.5	both (const. power)	37.50	1.578	8.02	0.337	95.79
	50	both (const. power)	25.00	1.378	5.35	0.295	94.49

Table 6.7. Energy losses, power losses and efficiency of each converter in configuration 2r

PV power (kW)	Total energy losses (kWh)	Power losses charging the BEB(kW)	Power losses charging the ESS (kW)
0	1.067	9.404	3.330
12.5	1.241	10.218	4.144
25	1.267	10.340	4.266
37.5	1.305	10.520	4.446
50	1.356	10.759	4.685

Table 6.8. Total energy and power losses of the configuration 2 depending on the PV power

6.3.4 Configuration 0

In this topology, corresponding to Fig. 5.11, it becomes clear that since there is no ESS, the power handled at all times by both converters is equivalent to the recharge power of the BEB. Therefore, during the subperiod in which the BEB is not recharged, the power that circulates through these converters is, like its losses, zero.

The results obtained are as follows:

Converter ref.	PV power (kW)	Subperiod (charging of BEB or ESS)	Input power (kW)	Power losses (kW)	Input energy (kWh)	Energy losses (kWh)	Efficiency
0.1	-	BEB	197.72	4.634	11.53	0.270	97.66
		EES (none)	0	0	0	0	-
0.2	-	BEB	197.72	4.246	11.53	0.248	97.85
		EES (none)	0	0	0	0	-
			Total:	8.879	Total:	0.518	

Table 6.9. Energy losses, power losses and efficiency of each converter in configuration 0

6.4 Results

The results of tables 6.4, 6.6, and 6.8 have determined the efficiencies of each configuration, shown in Fig. 6.2. These efficiencies have been calculated by means of the quotient of the energy with which the BEB is recharged in each period of 770 seconds (E_{cp}) and the energy provided by the energy sources during that same time. This energy sources are the grid and the PV array. In turn, this energy generated by the sources is equal to the energy with which the BEB is recharged plus the total energy losses of each configuration produced in both periods:

$$\rho = \frac{E_{cp}}{E_{grid} + E_{PV}} = \frac{E_{cp}}{E_{cp} + E_{losses}}$$

The performance of configuration 2 is for all PV power values higher than that configuration 1.1 and 1.2, as shown in Fig. 6.2. In turn, the performance of configuration 1.2 is higher than that of configuration 1.1.

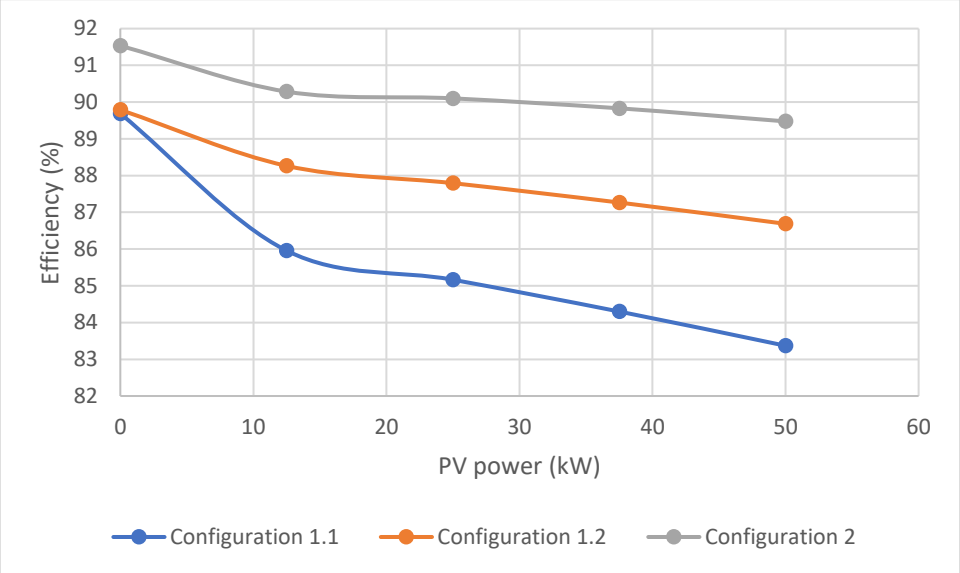

Fig. 6.2. Efficiencies depending on the PV power

6.5 Analysis of the results

6.5.1 Dependence of losses on the availability of PV power

It should be noted that for all 3 configurations the efficiencies decrease as the PV power increases, which means that the power losses increase. In the case of configuration 1.1, the reason is obvious since, in the case of no PV availability, it is the grid that provides the missing power. Configuration 1.1 uses an AC-Bus so there is no conversion stage between the grid and this AC-Bus. However, the generated PV power flows through the converters 1.1.3 and 1.1.4.

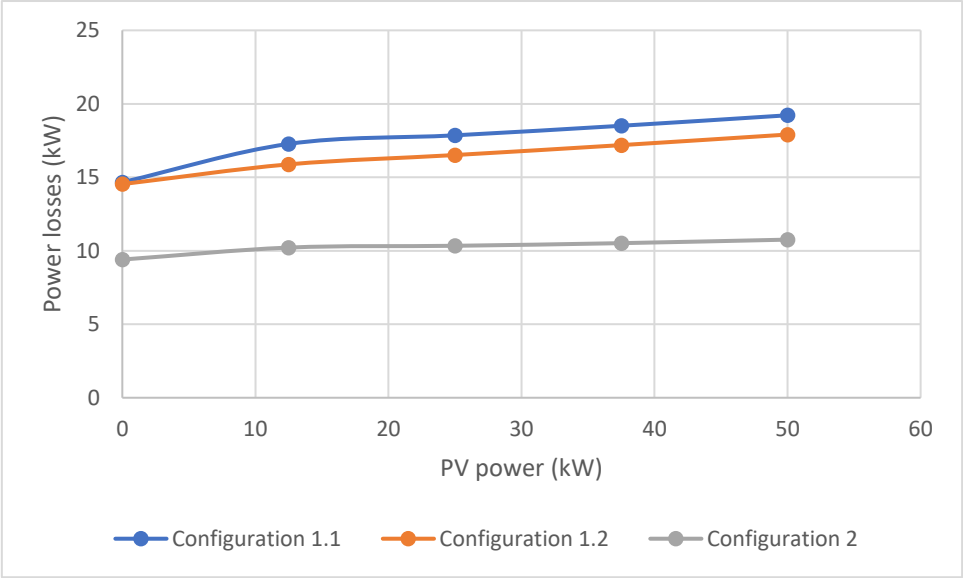

Fig. 6.3. Power losses during the BEB charge depending on the PV power

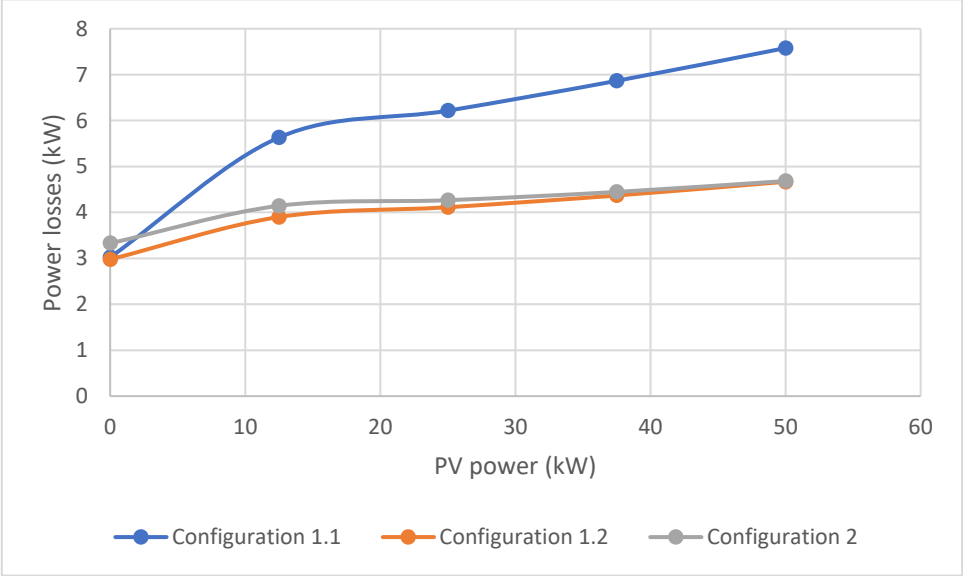

Fig. 6.4. Power losses during the ESS charge depending on the PV power

In the case of configuration 1.2, although losses also increase with the increase in PV availability for the same reason, the dependency is not as great as for configuration 1.1. With P_{PV}= 0, the losses are practically the same as for configuration 1.1. The reason is that if the photovoltaic system and its conversion stage did not exist, these two configurations would be the same.

However, for higher availability of PV power, power losses for configuration 1.2 are lower than for configuration 1.1 regardless of the subperiod analyzed, as shown in Fig. 6.3 and Fig. 6.4. During the recharge of the ESS, the lower losses are due to the fact that in this configuration the PV power flows only through the converters 1.2.4 and 1.2.3, while in configuration 1.1 it flows through the converters 1.1.3, 1.1.4, 1.1.6 and 1.1.5. During the recharge of the BEB, the difference in power losses is not as high as earlier, as can be seen in Fig. 6.3. This is because the PV power now flows through the same number of converters as in configuration 1.1. The reason that the losses are still lower in configuration 1.2. is that converter 1.2.5 is working closer to its nominal power than 1.1.4 and 1.1.6, as can be shown in Tables 6.3 and 6.5. This is because in

configuration 1.2 the PV array power flows together with the ESS power through the converter 1.2.5.

For configuration 2, the losses are not as high as in configuration 1.2 as the PV power increases. In both subperiods, for higher PV power there are greater losses in converter 2.3. However, the power that needs to be provided by the grid is lower when there is greater availability of PV. Therefore, the losses in converter 2.1 are lower.

6.5.2 Comparison between configurations 1.2 and 2

When comparing 1.1 and 1.2 configuration both with AC-Bus, it is 1.2 that shows the best performance. This is due to the DC-coupling support system in configuration 1.2. This type of coupling allows a significant reduction of losses compared to configuration 1.1 during the recharge of the ESS as the availability of PV power increases as explained in section 6.5.1.

When comparing the best performing AC-Bus topology (configuration 1.2) and the DC-Bus configuration (configuration 2), it that be concluded that configuration 2 deliver better results, as shown in section 6.4.

Although for the EES recharge sub-period the losses are very similar, the main difference lies in the recharging of the BEB.

The reason why the losses during the recharge of the BEB are considerably lower in configuration 2 is that a DC-Bus is being used. Thus, 2 DC/AC converters are being eliminated with respect to configuration 1.2: that of the ESS and that of the recharging point.

Even if two DC/AC converters are being eliminated, one must be included to connect the DC-Bus to the grid. However, this converter works with a maximum power of 75 kW, while the removed converters worked with a maximum power of 175 kW (converter 1.2.5) and 250 kW (converter 1.2.1) during the BEB recharge. For this reason, the power losses in converter 2.1 are not as great as those in converters 1.2.5 and 1.2.1.

During the ESS charge no power flows through the converter 1.2.1. This is the reason why during this subperiod the difference in losses is not as big as during the recharge of the BEB. Only the losses of converter 1.2.5 are avoided in this subperiod if configuration 2 is used and not also those of converter 1.2.1, as was the case during the BEB charge.

6.5.3 Comparison with configuration 0

The configuration 0, corresponding to the one existing right now in the FSC at UPNA, counts as expected with higher efficiency, as can be seen in Fig. 6.5.

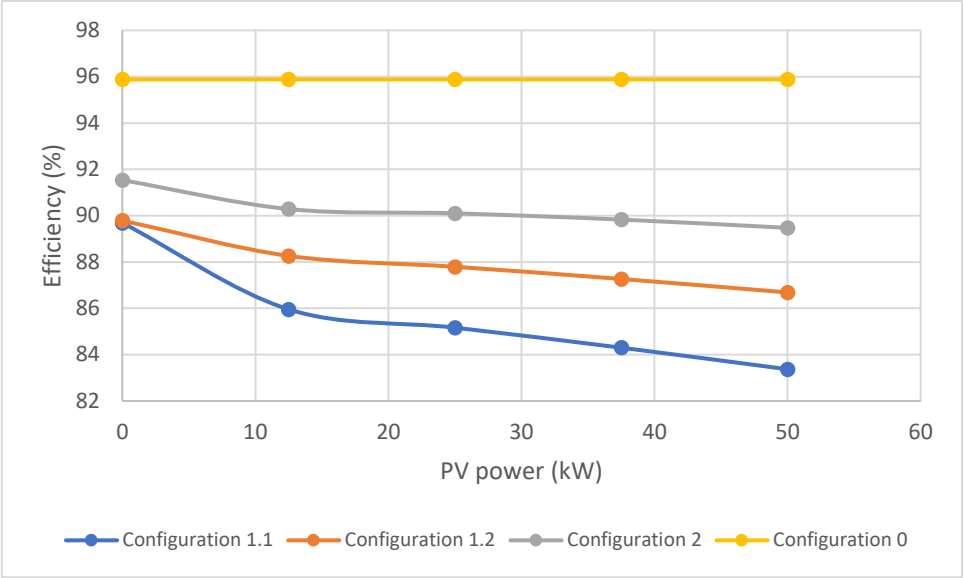

Fig. 6.5. Efficiencies depending on the PV power including configuration 0 efficiency

This is because in configuration 0 losses only occur during the recharge of the BEB as the rest of the time no power flows through any of the conversion stages. Therefore, in order to compare the efficiency of the proposed configurations and the existing one, it is more appropriate to show the power losses only during the charging subperiod of the BEB, as shown in Fig. 6.6

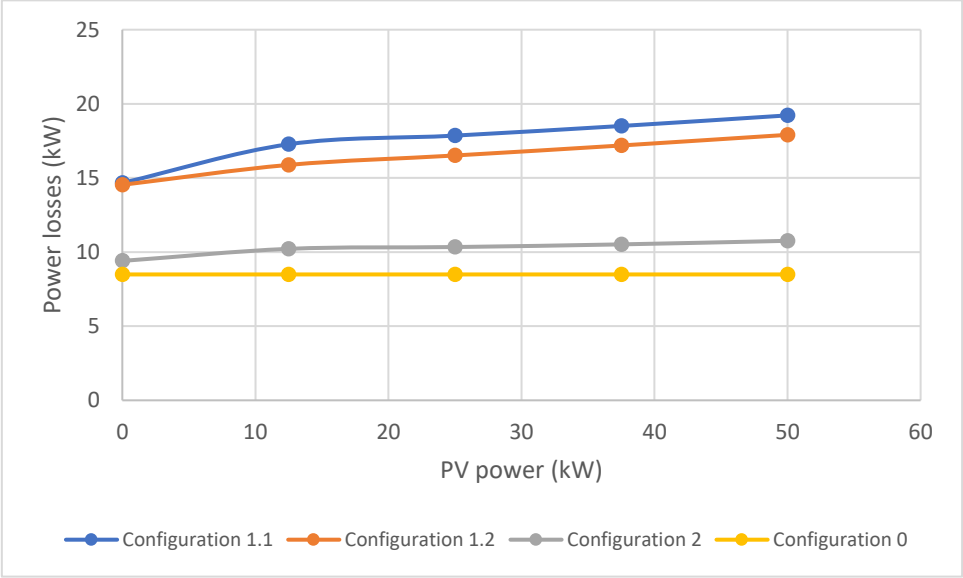

Fig. 6.6. Power losses during the BEB charge depending on the PV power

When comparing only the power losses during this subperiod, one can see that the losses of the current topology are lower than those of the rest of the topologies. This is because in configuration 0 there are only two converters, which are also in an operating point close to the nominal one. The efficiencies of these converters 0.1 and 0.2 are very high, as shown in Table 6.9.

It is therefore obvious that in terms of efficiency, the current configuration is the most appropriate for the reason above mentioned. However, the reasons for proposing configurations 1.1, 1.2, 2 instead of the current configuration are the following:

- Including stationary ESS in order to reduce the power consumption peaks from the grid and the required power of the transformation center.
- Including PV generation

7 Estimated costs of the proposed configurations

In this chapter the cost of the configurations in Chapter 5 are estimated, both the newly proposed and the existing FCS. To this end, section 7.1 lists the considerations made for this calculation. Section 7.2 shows the results obtained

7.1 Considerations

As mentioned in Chapter 1, the quantified costs are those corresponding to:

- Semiconductors
- Passive components
- Transformer

The price of the semiconductors chosen in chapter 5 were taken from SEMIKRON website,

In the case of coils, they indeed vary a lot depending on the application, ripple, voltages, currents, etc., because they can change material and have different core and winding proportions. However, all inductors of the same type have been considered, corresponding to those of the JNEX type, which is a type of magnetic material for the core (silicon iron). The cost per watt depending on the inductance value of these coils is shown in Fig. 7.1. This values have been provided by the supervisors of this BSc. Thesis.

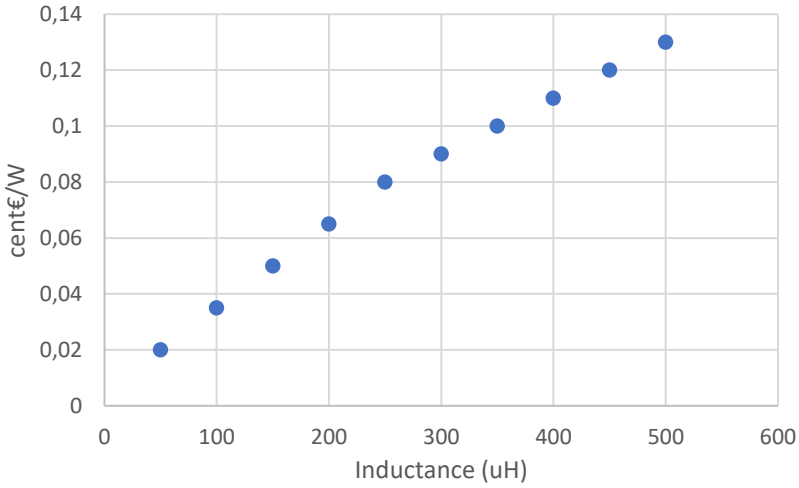

Fig. 7.1. Price dependence on the inductance value of a JNEX type coil

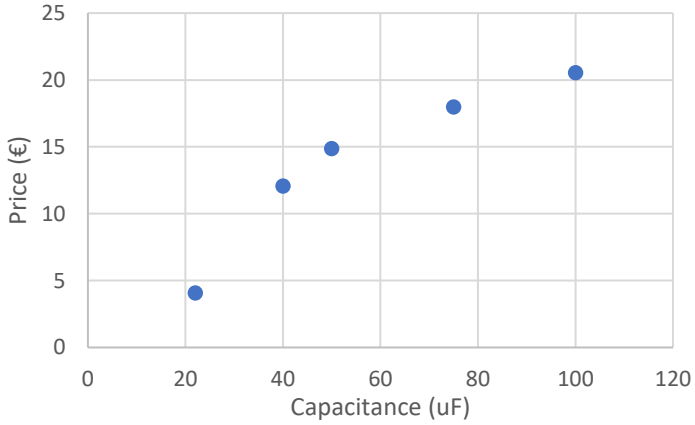

Fig. 7.2. Price dependence on the capacitance value of a film capacitor

A similar procedure has been followed for the LCL filter capacitors. Reference prices of 230 V AC film capacitors have been chosen, shown in Fig. 7.2. A dependence of the price on the capacity value price evolution has been estimated with a grade 3 polynomial trend. The capacity values calculated in Chapter 5 have been used to determine the price of the capacitors needed.

A value of 0.72 cents/W was used for the transformation center. This value has also been obtained using an estimate based on commercial costs.

7.2 Results

7.2.1 Configuration 1.1

The costs calculated for topology 1.1 are shown in Table 7.1.

Converter ref.	Component	Unit price (€)	Nº units	Total (€)
1.1.1	SEMiX404GB12E4s	116.45	3	349.35
1.1.2	SKM400GAR12E4	119.47	1	119.47
1.1.3	SEMiX151GAL12E4s	46.31	1	46.31
1.1.4	SEMiX151GB12E4s	59.42	3	178.26
1.1.5	SEMiX603GB12E4p	263.2	1	263.20
1.1.6	SEMiX404GB12E4s	116.45	3	349.35
			Total cost of semiconductors:	**1305.94**
1.1.1	C=63.3 uF	16.54	3	49.61
1.1.4	C=6.3 uF	1.87	3	5.60
1.1.6	C=44.5 uF	12.07	3	36.22
1.1.1	L= 40 uH (83,3 kW)	12.15	6	72.90
1.1.2	L= 546 uH (250 kW)	267.69	1	267.69
1.1.3	L= 275 uH (50 kW)	35.14	1	35.14
1.1.4	L= 101 uH (16.7 kW)	5.19	6	31.16
1.1.5	L= 379 uH (175 kW)	153.78	1	153.78
1.1.6	L= 57 uH (58.3 kW)	11.29	6	67.73
			Total cost of passive components:	**719.63**
-	Transformer (75 kW)	540.00	1	540.00
			Transformer cost:	**540.00**

Table 7.1. Estimated costs for configuration 1.1

7.2.2 Configuration 1.2

The costs calculated for topology 1.2 are shown in Table 7.2.

Converter ref.	Component	Unit price (€)	Nº units	Total (€)
1.2.1	SEMiX404GB12E4s	116.45	3	349.35
1.2.2	SKM400GAR12E4	119.47	1	119.47
1.2.3	SEMiX603GB12E4p	263.20	1	263.20
1.2.4	SEMiX151GAL12E4s	46.31	1	46.31
1.2.5	SEMiX404GB12E4s	116.45	3	349.35
			Total cost of semiconductors:	**1127.68**
1.2.1	C=63.3 uF	16.54	3	49.61
1.2.5	C=56.8 uF	15.16	3	45.47
1.2.1	L= 40 uH (83.3 kW)	12.15	6	72.90
1.2.2	L= 546 uH (250 kW)	267.69	1	267.69
1.2.4	L= 275 uH (50 kW)	35.14	1	35.14
1.2.3	L= 379 uH (175 kW)	153.78	1	153.78
1.2.5	L= 45 uH (75W)	12.00	6	71.98
			Total cost of passive components:	**696.57**
-	Transformer (75 kW)	540.00	1	540.00
			Transformer cost:	**540.00**

Table 7.2. Estimated costs for configuration 1.2

7.2.3 Configuration 2

The costs calculated for topology 2 are shown in Table 7.3.

Converter ref.	Component	Unit price (€)	Nº units	Total (€)
2.1	SEMiX151GB12E4s	59.42	3	178.26
2.2	SKM400GAR12E4	119.47	1	119.47
2.3	SEMiX151GAL12E4s	46.31	1	46.31
2.4	SEMiX603GB12E4p	263.20	1	263.20
			Total cost of semiconductors:	**607.24**
2.1	C=12 uF	3.20	3	9.61
2.1	L= 83 uH (83.3 kW)	6.61	6	39.63
2.2	L= 546 uH (250 kW)	267.69	1	267.69
2.3	L= 275 uH (50 kW)	35.14	1	35.14
2.4	L= 379 uH (175 kW)	153.78	1	153.78
			Total cost of passive components:	**505.84**
-	Transformer (75 kW)	540.00	1	540.00
			Transformer cost:	**540.00**

Table 7.3. Estimated costs for configuration 2

7.2.4 Configuration 0

The costs calculated for the current topology are shown in Table 7.4.

Converter ref.	Component	Unit price (€)	Nº units	Total (€)
0.1	SEMiX404GB12E4s	116.45	3	349.35
0.2	SKM400GAR12E4	119.47	1	119.47
			Total cost of semiconductors:	**468.82**
0.1	C=63.3 uF	16.54	3	49.61
0.1	L= 40 uH (83.3 kW)	12.15	6	72.90
0.2	L= 546 uH (250 kW)	267.69	1	267.69
			Total cost of passive components:	**390.20**
-	Transformer (250 kW)	1800.00	1	1800.00
			Transformer cost:	**1800.00**

Table 7.4. Estimated costs for configuration 0

8 Final Comparison

In this chapter, a final comparison between the proposed configurations will be made, including the current topology. The comparative criteria determined in Chapter 1 will be used, which are as follows:

- efficiencies of each topology
- semiconductor cost
- passive components cost
- transformer cost

A rating scale has been determined for these criteria, as shown in Table. 8.1. In the rating scale used, 4 corresponds to the highest rating while 1 corresponds to the lowest.

CRITERIA	RATING SCALE			
	1	2	3	4
Efficiency	Very low	Low	High	Very high
Semiconductor cost (€)	>1200	900-1200	600-900	<600
Passive components cost (€)	>700	600-700	500-600	<500
Transformer cost (€)	>700	600-700	500-600	<500

Table 8.1. Rating scale of the criteria

Subsequently, each of the configurations has been assessed with the rating scales defined in Table 8.1, as shown in the Table. 8.2.

CRITERIA	CONGIFURATION ASSESSMENT			
	Config. 1.1	Config. 1.2	Config. 2	Config. 0
Efficiency	1	2	3	4
Semiconductor cost (€)	1	2	3	4
Passive components cost (€)	1	2	3	4
Transformer cost (€)	4	4	4	1

Table 8.2. Configuration assessment

The results are shown in Fig. 8.1.

As can be seen in Fig. 8.1, it is the current configuration that has the best rating in terms of energy efficiency. As already mentioned in chapter 6, this result was to be expected since it is only in operation during the recharge of the BEB.

However, the reason for proposing configurations 1.1, 1.2, and 2 is that the support system and the PV array was intended to be included in the current FSC. Therefore, taking into account only the proposed configurations, it is topology 2 that shows a better performance independently of the PV availability. As observed in chapter 6, the best performance of this topology is due to the DC-Bus, which prevents the power provided by the ESS to the BEB from circulating through AC/DC converters.

With regards to the costs of semiconductors and passive components, it is again the current topology that has the best valuation in this criterion. However, if, for the same reason as before, this topology is overlooked, it is configuration 2 that has the lowest price.

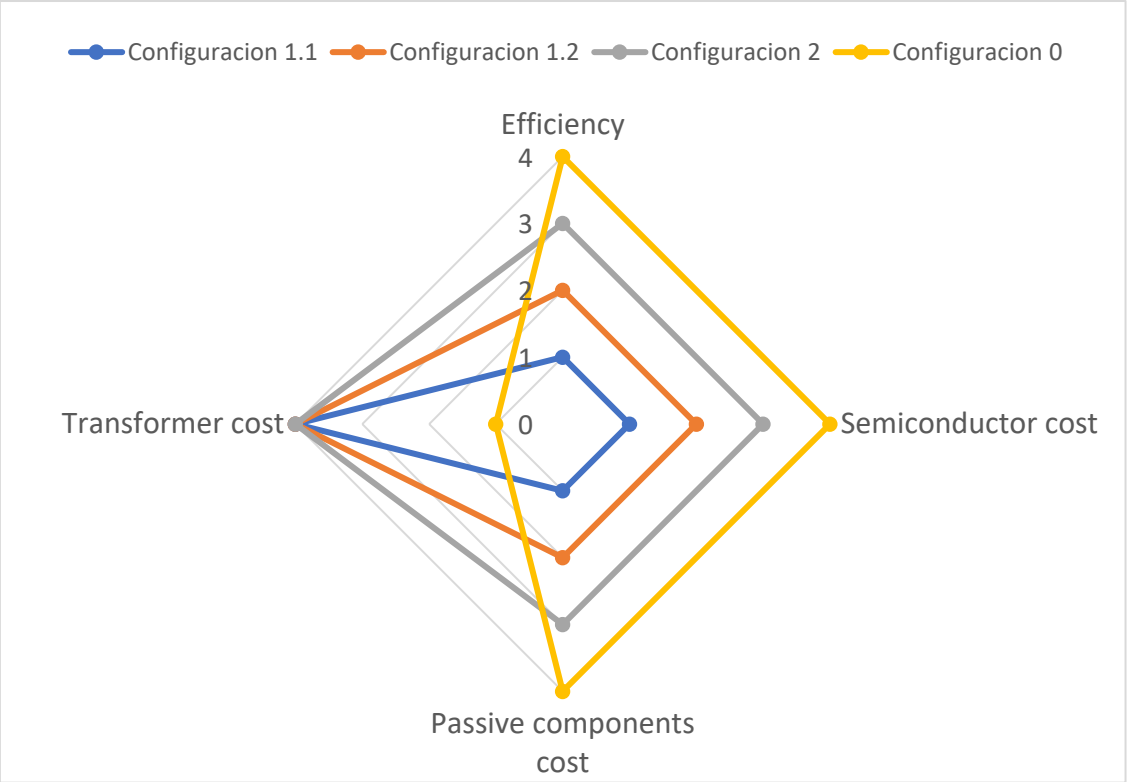

Fig. 8.1. Radar chart for global comparison of all configurations

This result is easily justifiable due to the lower number of components that are needed in the DC-Bus option. Besides, the extra AFE converter needed in this configuration does not need to have a high nominal power, since the ESS significantly reduces the peak power demand of the grid. This is the reason why this converter does not make the configuration provided with DC-Bus more expensive.

When comparing the cost of the transformers, the proposed topologies have better results than the current FCS. The reason is the already mentioned use of ESS, which allows reducing the peak power demand of the grid. The nominal power of the transformers in the proposed configurations is the same for all of them, as they all include the same ESS.

Comparing all the costs considered in this thesis, the difference in transformer costs can justify any of the alternatives proposed compared to the current one.

However, it should be noted that the need for transformer with lower nominal power is due to the fact that these configurations are provided with a PV array and stationary ESS. If a comparison of all costs is desired, the price of these components should be included.

It should also be pointed out that other expenses of converters such as the costs of drivers, wiring, signal circuitry, cooling system, and mechanical enclosure have not been considered.

The contracted power must be included if such a comparison of all costs is made. Without going into numbers, it is known that it may be reduced using the ESS, which accounts for a large percentage of the total cost.

In Spain, for contracted power greater than 15 kW, it is not the maximum recorded value that is taken, but the highest value of the fifteen-minute average of the power registered during the

month. For this reason, the power required to be contracted is reduced from around 180 kW to 75 kW, which means a great difference in cost [8].

In view of the results, it can be therefore concluded that for the proposed topologies, it is configuration 2 the one that shows the best results in terms of efficiency and prices for semiconductors and passive components.

9 Interleaving technique

This chapter first lists the advantages of using interleaved converters.

Section 9.2 discusses the difference in losses between the 1.1.1 converter dimensioned in Chapter 5 and the interleaved converter 1.1.1.

Sections 9.3 and 9.4 compare the efficiencies and costs of the configurations dimensioned in chapter 5 and the same configurations but with interleaved converters.

9.1 Reasons for using interleaved converters

When designing converter topologies, there is an option called interleaving technique. As seen in Chapter 2, this is a technology that is often proposed in the conversion stages of a FCS. This technique consists of the operation of N identical converters in parallel, which implies [20]:

- an increase of N times the number of devices used in the equipment (semiconductors, coils, conductors...)
- a decrease in the size and price of each one of them

Interleaving consists of the inclusion of "N" parallel branches composed of identical converters with control signals synchronized at the same frequency but out of phase. This offset causes the currents of each branch, which have the same mean value and high-frequency ripples, to be out of phase. The sum of these currents at the output of the overall circuit produces a significant cancellation of harmonics at the switching frequency. This output current thus presents a reduction in the ripple amplitude. [20]

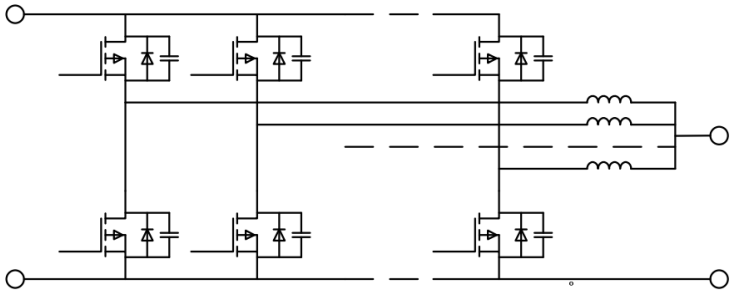

Fig. 9.1. Interleaved DC/DC converter [20]

If "N" is the number of identical branches or converters connected in parallel and "f" is the switching frequency, the advantages of this type of technology include [20]:

- For a given f, by performing interleaving with a phase shift of "2π/N", the frequency of the system's output current ripple is "f-N", which makes it possible to meet the specifications for ripples with lower output capacities and lower inductance values.
- For an output ripple frequency "f", the switching frequency of each leg can be reduced to "f/N" with a consequent reduction in switching losses.
- The output current ripple amplitude is reduced by a factor of "1/N".
- The currents circulating in each branch are reduced by "1/N", which allows for the selection of lower power semiconductor devices.

9.2 Analysis of power losses in interleaved converters

The interleaving technique has been implemented in 1.1.1 converter of the 1.1 topology. In order to achieve this, a number of branches of N=3 were selected as seen in chapter 2, as was proposed by some authors. Therefore, there have been searched new semiconductors of power of a third part than the ones used in the converter 1.1.1. In this case, SEMiX151GB12E4s with a maximum collector current of 150 A has been chosen, instead of the 400 A semiconductor needed without interleaving. No semiconductor has been found with parameters closer to those needed.

The values of the passive components of the LCL filter are the same as in the original converter since, although the current for each leg is 3 times lower, it still allows that the ripple on the leg can also be 3 times greater. Despite this higher branch ripple, as shown in section 9.1, the ripple at the output may be the same as for the original converter. The number of coils corresponding to those named Li in Chapter 5 is multiplied by 3, although their power is a third part of the Li of the converter 1.1.1. The number of capacitors and Lo coils in converter 1.1.1 is the same as in the interleaved converter as is the value, since their connection point remains in the same place.

MATLAB software was used as for the loss calculations in Chapter 6. The MATLAB script can be found in Appendix A.2

The power losses in the interleaved converter 1.1.1 are shown in Fig. 9.2, while Fig. 9.3 shows the power losses in converter 1.1.1 but with the classical active rectifier topology.

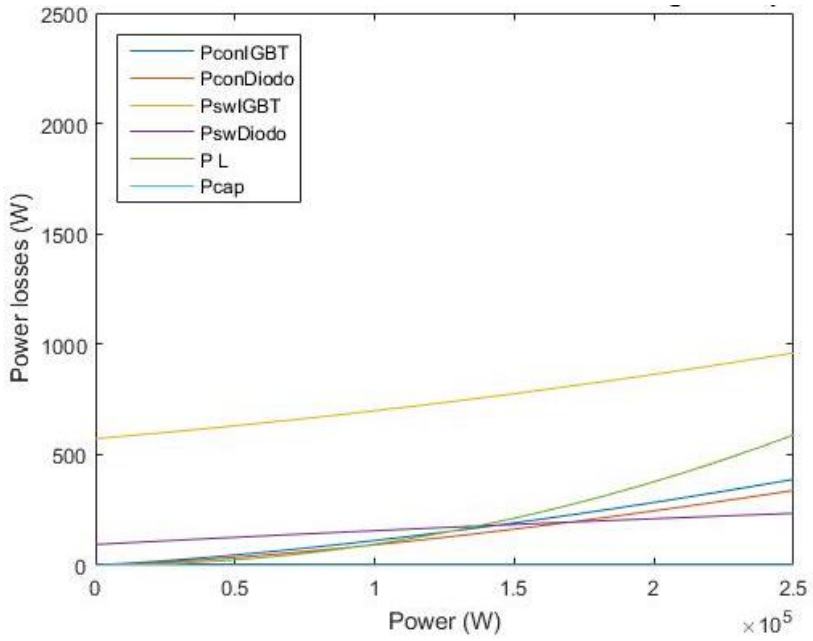

Fig. 9.2. Power losses in interleaved converter 1.1.1

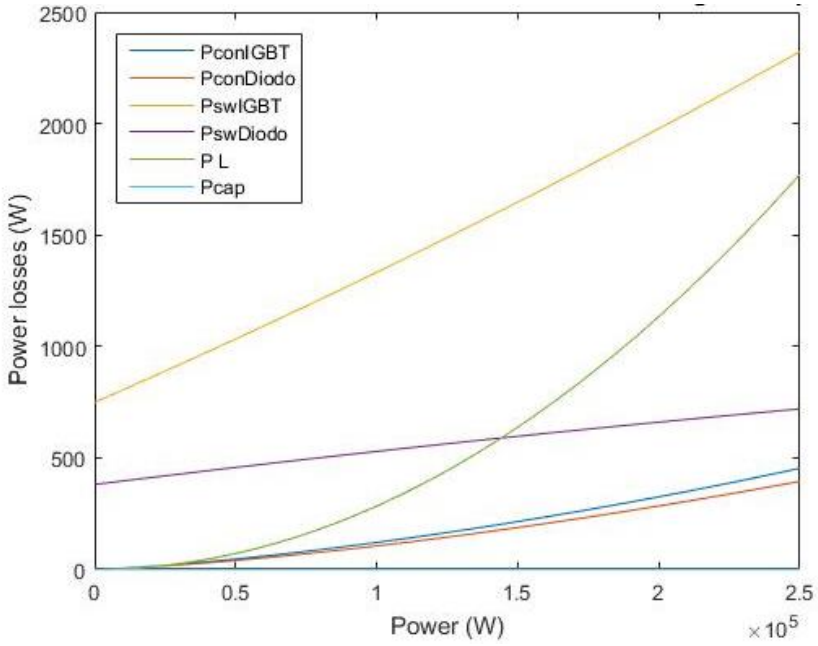

Fig. 9.3. Power losses in converter 1.1.1

Fig 1.2 and 1.3 show how inductance losses (P L) have been reduced by 3 times compared to the original converter. This is because if the losses in the inductances of the original converter are:

$$P_L = I^2 * R_L$$

Then, the losses in the interleaved converter inductances are:

$$P_{L\,inter} = \frac{I^2}{3^2} * R_L * 3 \quad ,$$

as the currents per inductance are now 3 times lower but there are also 3 times more coils.

Figures 1.2 and 1.3 also show how the switching losses of IGBTs and diodes are 3 times lower. It is a result that makes sense if we look at the demonstration of [21], in which it is determined that the switching loss in interleaved converter semiconductors is N times less than that of one-leg converters.

These figures also show how the conduction losses of IGBTs and diodes remain the same. This can be justified through the conduction loss equation of these two semiconductors:

$$P_{cond,IGBT} = I_c * V_{ce\,sat} * D$$

$$P_{cond,diode} = I_f * V_f * (1 - D)$$

In the interleaved converter, these equations are changed into:

$$P_{cond,IGBT} = \frac{I_c}{N} * V_{ce\,sat} * D * N$$

$$P_{cond,diode} = \frac{I_f}{N} * V_f * (1 - D) * N$$

This confirms that the results obtained for losses in the interleaved converter are correct.

Figure 1.4 shows the performance comparison for the two possibilities. The results of the efficiencies for 250 kW for the interleaved converter and the original converter are 99.00% and 97.74% respectively.

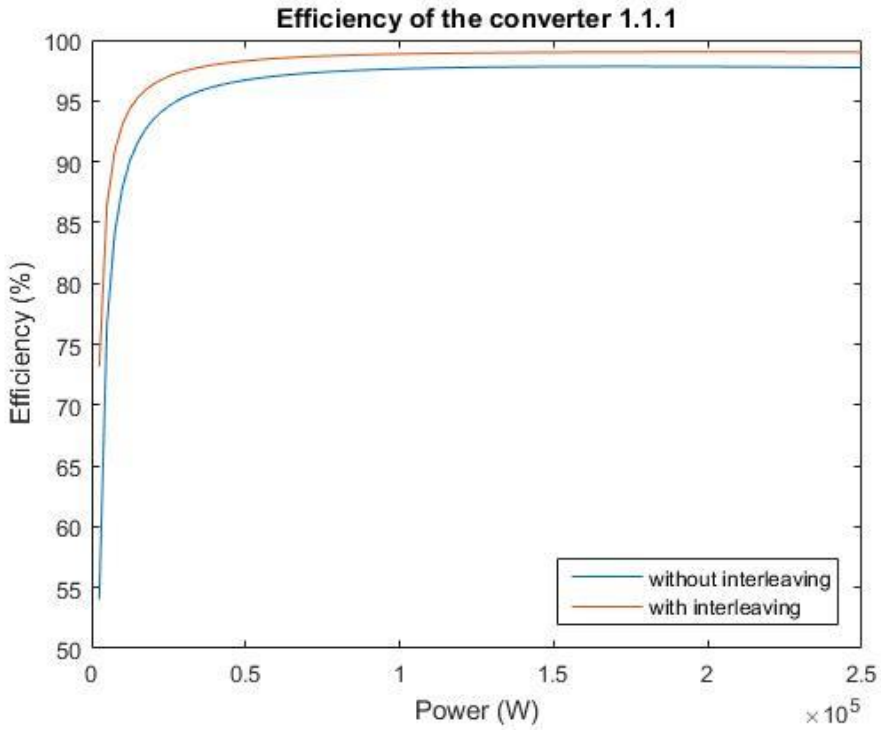

Fig. 9.4. Converter 1.1.1 efficiency with and without interleaved converters

9.3 Efficiencies of the proposed configurations with interleaved converters

In this section the new efficiencies were calculated for the proposed configurations when interleaved converters with 3 parallel branches are used.

In order to achieve this, it was necessary to select new semiconductors according to the new collector current values required. The semiconductors selected for each converter are listed in tables 9.1, 9.3, and 9.5.

The procedure for calculating the new efficiencies was the same as in Chapter 6. The only difference was to change the data sheets (different graphs for Eon, Eoff, Err, Vf, Vce) to those of the new semiconductors chosen.

Fig. 9.5 shows both the new efficiencies and those already calculated in Chapter 6.

The efficiencies of interleaved converter topologies are higher than those of the topologies in Chapter 6, as shown in Fig 9.5. This result was to be expected after the power loss analysis in section 9.2.

As can be seen in the figure, the losses of the configurations with interleaved converters do not increase significantly as the PV power increases. This is due to the high efficiencies of the interleaved converters, even at operating points far from their nominal power. Figure 9.4 shows the example of the converter 1.1.1 with a high performance at operating points far from its nominal power.

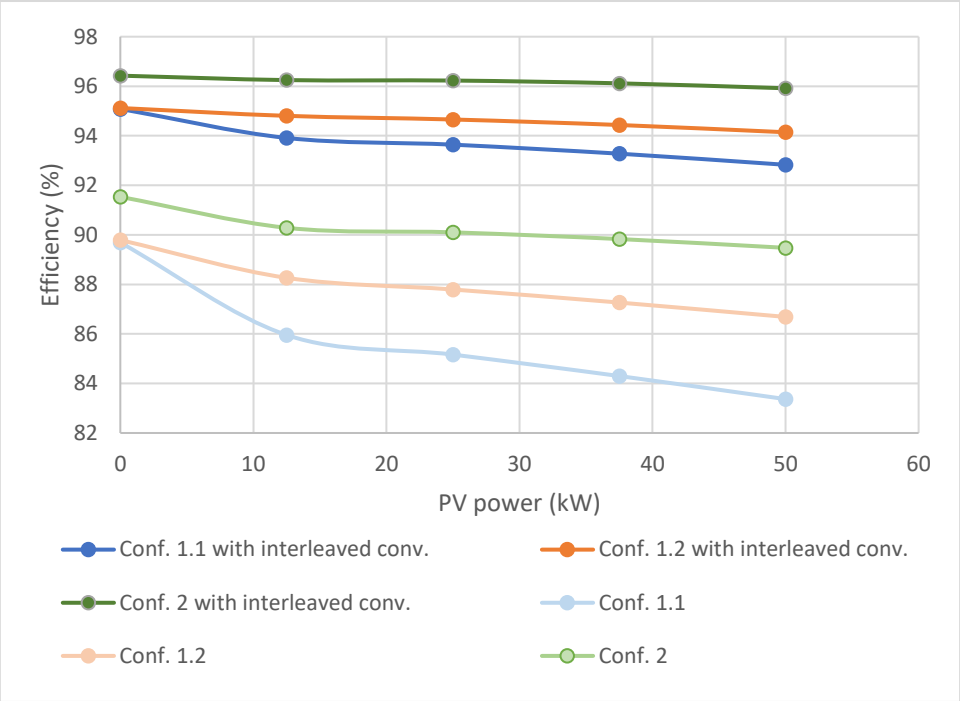

Fig. 9.5. Efficiencies of the proposed configurations with and without interleaved converters

The performance difference between the same configuration with or without interleaving technique will determine whether using interleaved converters is worthwhile despite the cost difference discussed in section 9.4.

9.4 Costs of the proposed configurations with interleaved converters

As in Chapter 7, the quantified costs are only those for semiconductors and passive components. The cost of the transformer has not been included in this section as it is the same for the proposed configurations.

The cost of the passive components remains unchanged. As discussed in Section 9.2, if more coils are needed, they will be of less power. For the case of N=3 it is necessary 3 times more coils but their power will be a third. If the costs of the coils in the Fig. 7.1 are used, it is possible to calculate that the total price is the same. As for the capacitors, the number and capacity value are the same. For this reason, the costs of the passive components will be the same.

The difference lies in the price of semiconductors. In the new selection of semiconductors, to alter the result as little as possible, an attempt has been made to select them from the same family and with the necessary power. However, it has not been possible in all cases.

9.4.1 Configuration 1.1

The estimated semiconductor costs for topology 1.1 with interleaved converters are shown in Table 9.1.

Converter ref.	Component	Unit price (€)	Nº units	Total (€)
1.1.1	SEMiX151GB12E4s	44.57	9	401.13
1.1.2	SKM150GAR12T4	53.90	3	161.70
1.1.3	SK 60 GAL 125	28.22	3	84.66
1.1.4	SKM50GB12V	45.52	9	409.68

1.1.5	SEMiX202GB12E4s	75.37	3	226.11
1.1.6	SEMiX151GB12E4s	44.57	9	401.13
			TOTAL:	**1684.41**

Table 9.1. Estimated semiconductor costs for configuration 1.1 with interleaved converters

Table 9.2 shows the price of semiconductors of configuration 1.1 with and without interleaved converters. Table 7.1 has been used to estimate the cost of the semiconductors used in the 1.1 configuration with the classic converter topologies.

Configuration 1.1	Total semiconductor price (€)
Without interleaved converters	1305.94
With interleaved converters	1684.41

Table 9.2. Semiconductor costs in configuration 1.1 with and without interleaved converters

9.4.2 Configuration 1.2

The semiconductor costs estimated for topology 1.2 with interleaved converters are shown in Table 9.3.

Converter ref.	Component	Unit price (€)	Nº units	Total (€)
1.2.1	SEMiX151GB12E4s	44.57	9	401.13
1.2.2	SKM150GAR12T4	53.90	3	161.70
1.2.3	SEMiX202GB12E4s	75.37	3	226.11
1.2.4	SK 60 GAL 125	28.22	3	84.66
1.2.5	SEMiX151GB12E4s	44.57	9	401.13
TOTAL:				**1274.73**

Table 9.3. Estimated costs for configuration 1.2 with interleaved converters

Table 9.4 shows the price of semiconductors of configuration 1.1 with and without interleaved converters. Table 7.2 has been used to estimate the price of the semiconductors used in the 1.1 configuration with the classic converter topologies

Configuration 1.2	Total semiconductor price (€)
Without interleaved converters	1127.68
With interleaved converters	1274.73

Table 9.4. Semiconductor costs in configuration 1.2 with and without interleaved converters

9.4.3 Configuration 2

The semiconductor costs estimated for topology 1.1 with interleaved converters are shown in Table 9.5.

Converter ref.	Component	Unit price (€)	Nº units	Total (€)
2.1	SKM50GB12V	45.52	9	409.68
2.2	SKM150GAR12T4	53.90	3	161.70
2.3	SK 60 GAL 125	28.22	3	84.66
2.4	SEMiX202GB12E4s	75.37	3	226.11
			TOTAL:	**882.15**

Table 9.5. Estimated costs for configuration 2 with interleaved converters

Table 9.6 shows the price of semiconductors of configuration 1.1 with and without interleaved converters. Table 7.3 has been used to estimate the price of the semiconductors used in the 1.1 configuration with the classic converter topologies

Configuration 2	Total semiconductor price (€)
Without interleaved converters	607.24
With interleaved converters	882.15

Table 9.6. Semiconductor costs in configuration 2 with and without interleaved converters

9.5 Analysis of the results

The use of interleaved converters provides performance improvements for all configurations. As proved in section 9.2, these improved performances are due to the lower switching frequency of the semiconductors and the lower current flowing through each leg, despite the fact that the number of components is greater.

However, the costs of configurations with interleaved converters are higher as a result of economies of scale, as noted in section 6.4.

Furthermore, it should be noted that the estimated costs only reflect the increase in semiconductors and not the increase in other elements, such as drivers, cooling systems, mechanical elements, volume, weight, etc.

In view of the results, it can be concluded that it would be interesting to carry out a more in-depth analysis of the total costs of interleaved converters, having calculated in section 9.3 their high performance but also in section 9.4 its higher cost.

10 Conclusions and future work

In this BSc. Thesis 3 different ways were proposed to connect the stationary ESS, the PV array, and the recharging point. It has been proved that, with regards to efficiency and as far as possible at a cost level, the best option is the one proposed with DC-Bus, corresponding to the so-called configuration 2 shown in Fig 5.10.

Therefore, it can be considered that the objectives that were proposed at the beginning of this BSc. Thesis have been met.

However, it is true that when the project was started it was uncertain to what extent the configurations would be comparable in terms of price. Eventually, it was the costs of semiconductors, passive components, and transformers that led us to determine the lowest total cost.

But to compare the financial return of the proposed configurations including the current topology, it would be necessary to consider more costs such as the price of the PV array, the ESS, the cost of energy, the cost difference between AC and DC protections... Even the total cost of the converters including the elements that have not been considered as the drivers, wiring, signal circuitry, cooling system, and mechanical enclosure.

Not only the economic aspect should be analysed but also the contribution of renewable energies in improving environmental impacts such as reduction of carbon dioxide gas.

Following the results obtained in Chapter 9 it would also be very interesting to make a global comparison between the use of classical topologies and interleaved converters. For this purpose, the total cost of the converters should be considered, including the elements already mentioned that have not been studied in this thesis. However, the improved efficiency of interleaved converters also leads to savings in electricity bills, which should also be taken into account in the global comparison.

This thesis is only the first step in selecting the best topology for the FCS to be designed. In order to make this selection, a more in-depth cost-benefit study is needed, based on the results of this BSc. Thesis. In the same way, a field is left wide open for designing the control of the entire system.

REFERENCES

[1] D. Dujić, ”Electric Vehicles Charging -An Ultrafast Overview-“, École Polytechnique Fédérale de Lausanne (EPFL), Power Electronics Laboratory, Switzerland [Online]. Available: https://pcim.mesago.com/content/dam/messefrankfurt-mesago/pcim/2019/documents/pdf/en/PCIM_2018_Drazen_Dujic.pdf

[2] M. Jara and V. Blahnik, "Cost-effective medium-power charging station for public transport vehicles," *2016 International Conference on Applied Electronics (AE)*, Pilsen, 2016, pp. 103-106. [Online] Disponible: https://ieeexplore.ieee.org/stamp/stamp.jsp?tp=&arnumber=7577251

[3] D. Aggeler, F. Canales, H. Zelaya-De La Parra, A. Coccia, N. Butcher and O. Apeldoorn, "Ultra-fast DC-charge infrastructures for EV-mobility and future smart grids," *2010 IEEE PES Innovative Smart Grid Technologies Conference Europe (ISGT Europe)*, Gothenberg, 2010, pp. 1-8. [Online] Disponible: https://ieeexplore.ieee.org/stamp/stamp.jsp?tp=&arnumber=5638899

[4] S. Bai, D. Yu and S. Lukic, "Optimum design of an EV/PHEV charging station with DC bus and storage system," *2010 IEEE Energy Conversion Congress and Exposition*, Atlanta, GA, 2010, pp. 1178-1184. [Online] Disponible: https://ieeexplore.ieee.org/stamp/stamp.jsp?tp=&arnumber=7577251

[5] Pinto, J. & Monteiro, Vitor & Exposto, Bruno & Barros, Luis & Sousa, Tiago & Monteiro, Luís & Afonso, J.L.. (2018). “Power Electronics Converters for an Electric Vehicle Fast Charging Station with Energy Storage System and Renewable Energy Sources”. EAI Endorsed Transactions on Energy Web. 7. 161749. 10.4108/eai.13-7-2018.161749. [Online] Disponible: https://www.researchgate.net/publication/337434169_Power_Electronics_Converters_for_an_Electric_Vehicle_Fast_Charging_Station_with_Energy_Storage_System_and_Renewable_Energy_Sources

[6] W. Marańda, "Capacity degradation of lead-acid batteries under variable-depth cycling operation in photovoltaic system," 2015 22nd International Conference Mixed Design of Integrated Circuits & Systems (MIXDES), Torun, 2015, pp. 552-555. [Online]. Available: https://ieeexplore.ieee.org/stamp/stamp.jsp?tp=&arnumber=7208584

[7] A. Vázquez, “Modular desing proposals and parallel arrengement of synchronous boost converter for bidirectional power systems”, Ph.D. dissertation, Univ. de Oviedo, 2016 [Online]. Available: http://hdl.handle.net/10651/37566

[8] I. Ojer, A. Berrueta, J. Pascual, P. Sanchis and A. Ursúa, “Development of energy management strategies for the sizing of a fast charging station for electric buses”, Department of Electrical, Electronic and Communication Engineering of the Public University of Navarre (UPNA), Spain

[9] J. Mashal, T. Sloane, “A battery for hire: AC vs.DC coupling for solar+energy storage projects”, Fluence, [Online]. Available: https://blog.fluenceenergy.com/energy-storage-ac-dc-coupled-solar

[10] J. A. Davis, “Reverse DC-Coupled PV+Storage”, *Dynapower*. [Online]. Available: https://www.dynapower.com/reverse-dc-coupled-pv-plus-storage/

[11] D. Ronanki, A. Kelkar, and S. S. Williamson, “Extreme Fast Charging Technology—Prospects to Enhance Sustainable Electric Transportation”, Energies, vol. 12, no. 19, p. 3721, Sep. 2019. [Online]. Available: https://www.mdpi.com/1996-1073/12/19/3721

[12] D. Kumar, F. Zare and A. Ghosh, "DC Microgrid Technology: System Architectures, AC Grid Interfaces, Grounding Schemes, Power Quality, Communication Networks, Applications, and Standardizations Aspects," in IEEE Access, vol. 5, pp. 12230-12256, 2017, doi: 10.1109/ACCESS.2017.2705914

[13] D. Lumbreras, E. L. Barrios, A. Urtasun, A. Ursúa, L. Marroyo and P. Sanchis, "On the Stability of Advanced Power Electronic Converters: The Generalized Bode Criterion," in IEEE Transactions on Power Electronics, vol. 34, no. 9, pp. 9247-9262, Sept. 2019, doi: 10.1109/TPEL.2018.2884892

[14] D. Lumbreras, E. L. Barrios, A. Ursúa, L. Marroyo and P. Sanchis, "On the stability criteria for inverter current control loops with LCL output filters and varying grid impedance," 2017 19th European Conference on Power Electronics and Applications (EPE'17 ECCE Europe), Warsaw, 2017, pp. P.1-P.10, doi: 10.23919/EPE17ECCEEurope.2017.8099365

[15] A. Urtasun, P. Sanchis, F. Guinjoan and L. Marroyo, "Parameter-Independent Battery Control Based on Series and Parallel Impedance Emulation," in IEEE Access, vol. 7, pp. 70021-70031, 2019, doi: 10.1109/ACCESS.2019.2919275

[16] M. M. Mon, “Design of 50 kW DC-DC Converter used in Hybrid Electric Vehicle,” International Journal of Scientific Engineering and Technology Research, Dept of Electrical Power Engineering of Mandalay Technological University, 2014. [Online] Available: http://ijsetr.com/uploads/356412IJSETR1678-580.pdf

[17] Urtasun, J. Samanes, E. L. Barrios, P. Sanchis and L. Marroyo, "Control of a Photovoltaic Array Interfacing Current-Mode-Controlled Boost Converter Based on Virtual Impedance Emulation", in IEEE Transactions on Industrial Electronics, vol. 66, no. 5, pp. 3496-3506, May 2019, doi: 10.1109/TIE.2018.2856192

[18] L. Marroyo, J. Marcos, Asignatura del grado de Tecnologías Industriales de la UPNA “Convertidores Electrónicos de Potencia”, Capítulo 5, pág. 214

[19] Urtasun, P. Sanchis, F. Guinjoan and L. Marroyo, "Parameter-Independent Battery Control Based on Series and Parallel Impedance Emulation," in IEEE Access, vol. 7, pp. 70021-70031, 2019, doi: 10.1109/ACCESS.2019.2919275

[20] I. Gil Mera, “Diseño de un sistema de almacenamiento de energía híbrido basado en baterías y supercondensadores para su integración en microredes eléctricas”, trabajo de fin de carrera, Univ. de Sevilla, 2010 [En línea]. Disponible: http://catedraendesa.us.es/documentos/ProyectoFinCarrera%20IGM.pdf

[21] M. Florides, “Interleaved Switching of DC/DC Converters”, Ph.D. dissertation, Univ. Of Newcastle Upon Tyle, 2010. [Online]. Available: https://www.researchgate.net/publication/308886975_Interleaved_Switching_of_DCDC_Converters

APPENDIX A. MATLAB scripts

Appendix A.1. Power losses calculation

Converter 1.1.1

```
%Datos
Fcon=10e3;
Tcon=1/Fcon;
f=50;
Vdc=1000;
L=40.4e-6;
RL=0.018;
Pnom=250e3;
Vred=230;
Vref=600;
C=63.3E-6;
Rc=0.13;

%Inicializar valores
k=0;

Econ_IGBT=zeros(1,length(0:1:210));
Econm_IGBT=zeros(1,length(0:1:210));
Eper_IGBT=zeros(1,length(0:1:210));
Econ_Diodo=zeros(1,length(0:1:210));
Econm_Diodo=zeros(1,length(0:1:210));
Eper_Diodo=zeros(1,length(0:1:210));
El=zeros(1,length(0:1:210));
Econd=zeros(1,length(0:1:210));
Econ=zeros(1,length(0:1:210));
Eper=zeros(1,length(0:1:210));

P=zeros(1,length(0:1:210));
Pper=zeros(1,length(0:1:210));
n=zeros(1,length(0:1:210));

for i=0:1:210
    k=k+1;

    if k<=84
    P(k)=(0.1786*i+220)*1000;
    else
    P(k)=(0.0037*i^2-1.8384*i+363.4)*1000;
    end

    for t=0:Tcon:(0.01-Tcon)  %Semiciclo positivo

        %Cálculo de ton y toff
        m=2*sqrt(2)*Vred*sin(2*pi*f*t)/Vdc;
%m*Vdc/2=Vred*sqrt(2)*sin(2*pi*f*t)

        T=Tcon;
        ton=T*m;
        toff=T-ton;


        %Cálculo de Ic
        Il=P(k)*sin(2*pi*f*t)/(Vred*sqrt(2)*3); %Corriente en la bobina para
cada instante t
        Ilmed=(Il+P(k)/(Vred*sqrt(2)*3)*sin(2*pi*f*(t+Tcon)))/2;
        Ic=Ilmed;

        %Cargar valores Eon, Eoff, Err, Vce y Vf
        [Eon,Eoff,Err,Vce,Vf]=Graficas_conv_1_1_1(Ic);
```

```
        %Cálculo pérdidas IGBT
        Econ_IGBT(k)=Econ_IGBT(k)+ton*Vce*Ic; %Energía de conducción del IGBT
        Econm_IGBT(k)=Econm_IGBT(k)+((Eon+Eoff)*(Vdc/Vref)^1.3*1e-3); %Energía
de encendido y apagado del IGBT
        Eper_IGBT(k)=Econ_IGBT(k)+Econm_IGBT(k); %Energía de pérdidas en el
IGBT

        %Cálculo pérdidas Diodo
        Econ_Diodo(k)=Econ_Diodo(k)+toff*Ic*Vf; %Energía de conduccción del
Diodo
        Econm_Diodo(k)=Econm_Diodo(k)+Err*(Vdc/Vref)^0.6*1e-3; %Energía de
recuperación del Diodo
        Eper_Diodo(k)=Econ_Diodo(k)+Econm_Diodo(k);

        %Cálculo de pérdidas en la bobina
        El(k)=El(k)+Ic^2*RL*Tcon;

        %Cálculo de pérdidas en el condensador
        Icond=Ic*abs(i^2*(2*pi()*f)*L*C);
        Econd(k)=Econd(k)+Icond^2*Rc*Tcon;

        %Pérdidas totales en un semiciclo (0.01 s) teniendo en cuenta las 3
ramas
        Eper(k)=3*Eper_IGBT(k)+3*Eper_Diodo(k)+3*El(k)+3*Econd(k);

    end

        %Pérdidas (en potencia) y rendimientos
        Pper(k)=Eper(k)*100;
        n(k)=(P(k)-Pper(k))/P(k)*100;
end

%Potencia media y perdidas (kW)
Pot_Perdida=sum(Pper)/k/1000
Pot_media=sum(P)/k/1000


function [Eon,Eoff,Err,Vce,Vf]=Graficas_conv_1_1_1(Ic)
       Eon=-3E-20*Ic^3+5E-05*Ic^2+0.0304*Ic+ 6.6429;
       Eoff=5e-05*Ic^2+0.115*Ic+ 6.2143;
       Err=-4e-05*Ic^2+ 0.059*Ic+ 9.3393;
       Vce0=1;
       options = optimoptions('fsolve','MaxIter',600);
       Vce = fsolve(@(Vce)-1.3807*Vce^6+ 17.991 *Vce^5-87.239 *Vce^4+
       177.43*Vce^3- 71.274*Vce^2+ 17.646*Vce+ 0.3187-Ic,Vce0,options);
       Vf0=1;
       Vf = fsolve(@(Vf)3.1197*Vf^5- 25.159*Vf^4+ 60.68*Vf^3+ 22.752*Vf^2-
       3.7026*Vf-Ic- 0.9756,Vf0,options);
end
```

Converter 1.1.2

```
%Datos
Fcon=10e3;
Tcon=1/Fcon;
Ve=1000;
f=50;
Vsa=650;
L=546e-6;
RL=0.02;
f=50;
Vpt=10;
Vref=600;


%Inicializar valores
k=0;
```

```
Econ_IGBT=zeros(1,length(0:1:210));
Econm_IGBT=zeros(1,length(0:1:210));
Eper_IGBT=zeros(1,length(0:1:210));
Econ_Diodo=zeros(1,length(0:1:210));
Econm_Diodo=zeros(1,length(0:1:210));
Eper_Diodo=zeros(1,length(0:1:210));
El=zeros(1,length(0:1:210));
Econ=zeros(1,length(0:1:210));
Eper=zeros(1,length(0:1:210));

P=zeros(1,length(0:1:210));
Pper=zeros(1,length(0:1:210));
n=zeros(1,length(0:1:210));

 %Cálculo de ton y toff
        d=Vsa/Ve;
        T=Tcon;
        ton=T*d;
        toff=T-ton;

for i=0:1:210
    k=k+1;

    if k<=84
    P(k)=(0.1786*i+220)*1000;
    else
    P(k)=(0.0037*i^2-1.8384*i+363.4)*1000;
    end

        %Cálculo de Il
        Il=P(k)/Vsa

        %Cargar valores Eon, Eoff, Err, Vce y Vf
        [Eon,Eoff,Err,Vce,Vf]=Graficas_conv_1_1_2(Il);

        %Cálculo pérdidas IGBT
        Econ_IGBT(k)=Econ_IGBT(k)+ton*Vce*Il; %Energía de conducción del IGBT
        Econm_IGBT(k)=Econm_IGBT(k)+((Eon+Eoff)*(Ve/Vref)^1.3*1e-3); %Energía
de encendido y apagado del IGBT
        Eper_IGBT(k)=Econ_IGBT(k)+Econm_IGBT(k); %Energía de pérdidas en el
IGBT

        %Cálculo pérdidas Diodo
        Econ_Diodo(k)=Econ_Diodo(k)+toff*Il*Vf; %Energía de conduccción del
Diodo
        Econm_Diodo(k)=Econm_Diodo(k)+Err*(Ve/Vref)^0.6*1e-3; %Energía de
recuperación del Diodo
        Eper_Diodo(k)=Econ_Diodo(k)+Econm_Diodo(k);

        %Cálculo de pérdidas en la bobina
        El(k)=El(k)+Il^2*RL*Tcon;

        %Pérdidas totales
        Eper(k)=Eper_IGBT(k)+Eper_Diodo(k)+El(k);

        %Pérdidas (Potencia)
        Pper(k)=Eper(k)*Fcon;
        n(k)=(P(k)-Pper(k))/P(k)*100;
end

%Potencia media y perdidas (kW)
Pot_Perdida=sum(Pper)/k/1000
Pot_media=sum(P)/k/1000


function [Eon,Eoff,Err,Vce,Vf]=Graficas_conv_1_1_1(Il)
       Eon=6E-05*Il^2+ 0.0389*Il+ 7.9293;
```

```
        Eoff=1E-05*Il^2+0.1218*Il+ 6.3518;
        Err=-5E-05*Il^2+ 0.0787*Il+7.7221;
        Vce0=1;
        options = optimoptions('fsolve','MaxIter',500);
        Vce = fsolve(@(Vce)5.707*Vce^4- 61.068*Vce^3+ 233.63*Vce^2- 120.24*Vce+
        1.7936-Il,Vce0,options);
        Vf0=1;
        Vf = fsolve(@(Vf)-9.9405*Vf^3+ 122.98*Vf^2- 58.28*Vf-Il+
        2.0127,Vf0,options);
end
```

Converter 1.1.3

```
%Datos

Pnom=50e3; %Disponibilidad de potencia PV a variar entre 0, 12.5, 25, 37.5 y
50 kW

Fcon=20e3;
Tcon=1/Fcon;
Vsa=1000;
Ve=405;
L=275e-6;
RL=0.01;
f=50;
Vpt=10;
Vref=600;

%Cálculo de ton y toff
d=(Vsa-Ve)/Vsa;
T=Tcon;
ton=T*d;
toff=T-ton;

Il=Pnom/Ve;

%Cargar valores Eon, Eoff, Err, Vce y Vf
[Eon,Eoff,Err,Vce,Vf]=Graficas_conv_1_1_3(Il);

%Cálculo pérdidas IGBT
Econ_IGBT= ton*Vce*Il; %Energía de conducción del IGBT
Econm_IGBT=(Eon+Eoff)*(Vsa/Vref)^1.3*1e-3; %Energía de encendido y apagado del
IGBT
Eper_IGBT=Econ_IGBT+Econm_IGBT; %Energía de pérdidas en el IGBT

%Cálculo pérdidas Diodo
Econ_Diodo=toff*Il*Vf; %Energía de conduccción del Diodo
Econm_Diodo=Err*(Vsa/Vref)^0.6*1e-3; %Energía de recuperación del Diodo
Eper_Diodo=Econ_Diodo+Econm_Diodo;

%Cálculo de pérdidas en la bobina
El=Il^2*RL*Tcon;

%Pérdidas totales en un semiciclo teniendo en cuenta las 3 ramas(0,01s)
Eper=Eper_IGBT+Eper_Diodo+El;

%Pérdidas (Potencia)
Pper_elevador=Eper*Fcon
n=(Pnom-Pper_elevador)/Pnom*100



function [Eon,Eoff,Err,Vce,Vf]=Graficas_conv_1_1_3(Il)
        Eon=-3E-20*Il^3+5E-05*Il^2+0.0304*Il+ 6.6429;
        Eoff=5e-05*Il^2+0.115*Il+ 6.2143;
        Err=-4e-05*Il^2+ 0.059*Il+ 9.3393;
        Vce0=1;
```

```
        options = optimoptions('fsolve','MaxIter',500);
        Vce = fsolve(@(Vce)-14.888^3+ 114.77*Vce^2- 40.848*Vce- 1.4316-
        Il,Vce0,options);
        Vf0=1;
        Vf = fsolve(@(Vf)3.1197*Vf^5- 25.159*Vf^4+ 60.68*Vf^3+ 22.752*Vf^2-
        3.7026*Vf-Il- 0.9756,Vf0,options);
end
```

Converter 1.1.4

```
%Datos

P=50e3; %Disponibilidad de potencia PV

Fcon=20e3;
Tcon=1/Fcon;
f=50;
Vdc=1000;
L=101e-6;
RL=0.045;
Vred=230;
Vpt=10;
Vref=600;

%Inicializar valores
k=0;

Econ_IGBT=0;
Econm_IGBT=0;
Eper_IGBT=0;
Econ_Diodo=0;
Econm_Diodo=0;
Eper_Diodo=0;
El=0;
Econ=0;
Eper=0;

    for t=0:Tcon:(0.01-Tcon)  %Semiciclo positivo

        %Cálculo de ton y toff
        m=2*sqrt(2)*Vred*sin(2*pi*f*t)/Vdc;
%m*Vdc/2=Vred*sqrt(2)*sin(2*pi*f*t)
        T=Tcon;
        ton=T*m;
        toff=T-ton;

        %Cálculo de Ic
        Il=P*sin(2*pi*f*t)/(Vred*sqrt(2)*3); %Corriente en la bobina para cada
instante t
        Ilmed=(Il+P/(Vred*sqrt(2)*3)*sin(2*pi*f*(t+Tcon)))/2;
        Ic=Ilmed;

        %Cargar valores Eon, Eoff, Err, Vce y Vf
        [Eon,Eoff,Err,Vce,Vf]=Graficas_Conv_1_1_4(Ic);

        %Cálculo pérdidas IGBT
        Econ_IGBT=Econ_IGBT+ton*Vce*Ic; %Energía de conducción del IGBT
        Econm_IGBT=Econm_IGBT+((Eon+Eoff)*(Vdc/Vref)^1.3*1e-3); %Energía de
encendido y apagado del IGBT
        Eper_IGBT=Econ_IGBT+Econm_IGBT; %Energía de pérdidas en el IGBT

        %Cálculo pérdidas Diodo
        Econ_Diodo=Econ_Diodo+toff*Ic*Vf; %Energía de conduccción del Diodo
        Econm_Diodo=Econm_Diodo+Err*(Vdc/Vref)^0.6*1e-3; %Energía de
recuperación del Diodo
        Eper_Diodo=Econ_Diodo+Econm_Diodo;
```

```
        %Cálculo de pérdidas en la bobina
        El=El+Ic^2*RL*Tcon;

        %Pérdidas totales en un semiciclo teniendo en cuenta las 3
ramas(0,01s)
        Eper=3*Eper_IGBT+3*Eper_Diodo+3*El;

    end

%Pérdidas (Potencia)
Pper=Eper*100

n=(P-Pper)/P*100;

function [Eon,Eoff,Err,Vce,Vf]=Graficas_Conv_1_1_4(Ic)
       Eon=0.0006*Ic^2- 0.0306*Ic+ + 7.8;
       Eoff=-3E-05*Ic^2+0.115*Ic+ 2.12;
       Err=3E-07*Ic^3- 0.0002*Ic^2+ 0.0757*Ic+ 2.3;
       Vce0=1;
       options = optimoptions('fsolve','MaxIter',500);
       Vce = fsolve(@(Vce)-1.0982*Vce^6+14.254*Vce^5-67.149*Vce^4+131.19*Vce^3-
       62.961*Vce^2+5.984*Vce+0.0164-Ic,Vce0,options);
       Vf0=1;
       Vf = fsolve(@(Vf)-2.3528*Vf^4+ 10.079*Vf^3+ 23.485*Vf^2- 4.9025*Vf-Ic+
       0.0192,Vf0,options);
end
```

Converter 1.1.5 (ESS charge)

```
%Datos
Fcon=10e3;
Tcon=1/Fcon;
Vsa=500;
Ve=1000;
L=379e-6;
RL=0.014;
Pnom=75e3;
f=50;
Vpt=10;
Vref=600;

Il=Pnom/Vsa;

%Cálculo de ton y toff
d=Vsa/Ve;
T=Tcon;
ton=T*d;
toff=T-ton;

%Cargar valores Eon, Eoff, Err, Vce y Vf
[Eon,Eoff,Err,Vce,Vf]=Graficas_Conv_1_1_5_carga_ESS(Il);

%Cálculo pérdidas IGBT
Econ_IGBT=ton*Vce*Il; %Energía de conducción del IGBT
Econm_IGBT=(Eon+Eoff)*(Vsa/Vref)^1.3*1e-3; %Energía de encendido y apagado del
IGBT
Eper_IGBT=Econ_IGBT+Econm_IGBT; %Energía de pérdidas en el IGBT

%Cálculo pérdidas Diodo
Econ_Diodo=toff*Il*Vf; %Energía de conduccción del Diodo
Econm_Diodo=Err*(Vsa/Vref)^0.6*1e-3; %Energía de recuperación del Diodo
Eper_Diodo=Econ_Diodo+Econm_Diodo;

%Cálculo de pérdidas en la bobina
El=Il^2*RL*Tcon;

%Pérdidas totales en un semiciclo teniendo en cuenta las 3 ramas(0,01s)
```

```
Eper=Eper_IGBT+Eper_Diodo+El;

%Pérdidas (Potencia)
Pper_elevador=Eper*Fcon
n=(Pnom-Pper_elevador)/Pnom*100;



function [Eon,Eoff,Err,Vce,Vf]=Graficas_Conv_1_1_5_carga_ESS(Il)
       Eon=-2E-10*Il^4+ 8E-07*Il^3- 0.0008*Il^2+ 0.3502*Il- 24.653;
       Eoff=0.1222*Il+ 3.3648;
       Err=3E-08*Il^3- 0.0001*Il^2+ 0.1044*Il+ 8.1455;
       Vce0=1;
       options = optimoptions('fsolve','MaxIter',500);
       Vce = fsolve(@(Vce)4.7094*Vce^4- 52.862*Vce^3+ 208.48*Vce^2- 74.49*Vce+
       0.2065-Il,Vce0,options);
       Vf0=1;
       Vf = fsolve(@(Vf)3.9988*Vf^4- 44.949*Vf^3+ 198.38*Vf^2- 90.023*Vf-Il+
       0.5969,Vf0,options);
end
```

Converter 1.1.5 (BEB charge)

```
%Datos
Fcon=10e3;
Tcon=1/Fcon;
Vsa=1000;
Ve=500;
L=379e-6;
RL=0.014;
f=50;
Vpt=10;
Vref=600;

%Inicializar valores
k=0;

Econ_IGBT=zeros(1,length(0:1:210));
Econm_IGBT=zeros(1,length(0:1:210));
Eper_IGBT=zeros(1,length(0:1:210));
Econ_Diodo=zeros(1,length(0:1:210));
Econm_Diodo=zeros(1,length(0:1:210));
Eper_Diodo=zeros(1,length(0:1:210));
El=zeros(1,length(0:1:210));
Econ=zeros(1,length(0:1:210));
Eper=zeros(1,length(0:1:210));

P=zeros(1,length(0:1:210));
Pper=zeros(1,length(0:1:210));
n=zeros(1,length(0:1:210));

%Cálculo de ton y toff
d=(Vsa-Ve)/Vsa;
T=Tcon;
ton=T*d;
toff=T-ton;

for i=0:1:210
    k=k+1;

    if k<=84
    P(k)=(0.1786*i+220)*1000-75000;
    else
    P(k)=(0.0037*i^2-1.8384*i+363.4)*1000-75000;
    end

        %Cálculo de Ilmax
```

```
        Il=P(k)/Ve;

        %Cargar valores Eon, Eoff, Err, Vce y Vf
        [Eon,Eoff,Err,Vce,Vf]=Graficas_Conv_1_1_5_descarga_ESS(Il);

        %Cálculo pérdidas IGBT
        Econ_IGBT(k)=Econ_IGBT(k)+ton*Vce*Il; %Energía de conducción del IGBT
        Econm_IGBT(k)=Econm_IGBT(k)+((Eon+Eoff)*(Vsa/Vref)^1.3*1e-3); %Energía
de encendido y apagado del IGBT
        Eper_IGBT(k)=Econ_IGBT(k)+Econm_IGBT(k); %Energía de pérdidas en el
IGBT

        %Cálculo pérdidas Diodo
        Econ_Diodo(k)=Econ_Diodo(k)+toff*Il*Vf; %Energía de conduccción del
Diodo
        Econm_Diodo(k)=Econm_Diodo(k)+Err*(Vsa/Vref)^0.6*1e-3; %Energía de
recuperación del Diodo
        Eper_Diodo(k)=Econ_Diodo(k)+Econm_Diodo(k);

        %Cálculo de pérdidas en la bobina
        El(k)=El(k)+Il^2*RL*Tcon;

        %Pérdidas totales en un semiciclo teniendo en cuenta las 3
ramas(0,01s)
        Eper(k)=Eper_IGBT(k)+Eper_Diodo(k)+El(k);

        %Pérdidas (Potencia)
        Pper_elevador(k)=Eper(k)*Fcon;
        n(k)=(P(k)-Pper_elevador(k))/P(k)*100;
end

%Potencia media y perdidas (kW)
Pot_Perdida=sum(Pper)/k/1000
Pot_media=sum(P)/k/1000


function [Eon,Eoff,Err,Vce,Vf]=Graficas_Conv_1_1_5_descarga_ESS(Il)
      Eon=-2E-10*Il^4+ 8E-07*Il^3- 0.0008*Il^2+ 0.3502*Il- 24.653;
      Eoff=0.1222*Il+ 3.3648;
      Err=3E-08*Il^3- 0.0001*Il^2+ 0.1044*Il+ 8.1455;
      Vce0=1;
      options = optimoptions('fsolve','MaxIter',500);
      Vce = fsolve(@(Vce)4.7094*Vce^4- 52.862*Vce^3+ 208.48*Vce^2- 74.49*Vce+
      0.2065-Il,Vce0,options);
      Vf0=1;
      Vf = fsolve(@(Vf)3.9988*Vf^4- 44.949*Vf^3+ 198.38*Vf^2- 90.023*Vf-Il+
      0.5969,Vf0,options);
end
```

Converter 1.1.6 (ESS charge)

```
%Datos
Fcon=10e3;
Tcon=1/Fcon;
f=50;
Vdc=1000;
L=57e-6;
RL=0.025;
P=75e3;
Vred=230;
f=50;
Vpt=10;
Vref=600;

%Inicializar valores
k=0;
```

```
Econ_IGBT=0;
Econm_IGBT=0;
Eper_IGBT=0;
Econ_Diodo=0;
Econm_Diodo=0;
Eper_Diodo=0;
El=0;
Econ=0;
Eper=0;

    for t=0:Tcon:(0.01-Tcon)  %Semiciclo positivo

        %Cálculo de ton y toff
        m=2*sqrt(2)*Vred*sin(2*pi*f*t)/Vdc;
%m*Vdc/2=Vred*sqrt(2)*sin(2*pi*f*t)
        T=Tcon;
        ton=T*m;
        toff=T-ton;

        %Cálculo de Ic
        Il=P*sin(2*pi*f*t)/(Vred*sqrt(2)*3); %Corriente en la bobina para cada
instante t
        Ilmed=(Il+P/(Vred*sqrt(2)*3)*sin(2*pi*f*(t+Tcon)))/2;
        Ic=Ilmed;

        %Cargar valores Eon, Eoff, Err, Vce y Vf
        [Eon,Eoff,Err,Vce,Vf]=Graficas_Conv_1_1_6_carga_ESS(Ic);

        %Cálculo pérdidas IGBT
        Econ_IGBT=Econ_IGBT+ton*Vce*Ic; %Energía de conducción del IGBT
        Econm_IGBT=Econm_IGBT+((Eon+Eoff)*(Vdc/Vref)^1.3*1e-3); %Energía de
encendido y apagado del IGBT
        Eper_IGBT=Econ_IGBT+Econm_IGBT; %Energía de pérdidas en el IGBT

        %Cálculo pérdidas Diodo
        Econ_Diodo=Econ_Diodo+toff*Ic*Vf; %Energía de conduccción del Diodo
        Econm_Diodo=Econm_Diodo+Err*(Vdc/Vref)^0.6*1e-3; %Energía de
recuperación del Diodo
        Eper_Diodo=Econ_Diodo+Econm_Diodo;

        %Cálculo de pérdidas en la bobina
        El=El+Ic^2*RL*Tcon;

        %Pérdidas totales en un semiciclo teniendo en cuenta las 3
ramas(0,01s)
        Eper=3*Eper_IGBT+3*Eper_Diodo+3*El;

    end

%Pérdidas (Potencia)
Pper=Eper*100

n=(P-Pper)/P*100;



function [Eon,Eoff,Err,Vce,Vf]=Graficas_Conv_1_1_6_carga_ESS(Ic)
       Eon=-3E-20*Ic^3+5E-05*Ic^2+0.0304*Ic+ 6.6429;
       Eoff=5e-05*Ic^2+0.115*Ic+ 6.2143;
       Err=-4e-05*Ic^2+ 0.059*Ic+ 9.3393;
       Vce0=1;
       options = optimoptions('fsolve','MaxIter',500);
       Vce = fsolve(@(Vce)-14.888*Vce^3+ 114.77*Vce^2- 40.848*Vce- 1.4316-
       Ic,Vce0,options);
       Vf0=1;
       Vf = fsolve(@(Vf)3.1197*Vf^5- 25.159*Vf^4+ 60.68*Vf^3+ 22.752*Vf^2-
       3.7026*Vf-Ic- 0.9756,Vf0,options);
end
```

Converter 1.1.6 (BEB charge)

```
%Datos
Fcon=10e3;
Tcon=1/Fcon;
f=50;
Vdc=1000;
L=57e-6;
RL=0.025;
Vred=230;
f=50;
Vpt=10;
Vref=600;

%Inicializar valores
k=0;

Econ_IGBT=zeros(1,length(0:1:210));
Econm_IGBT=zeros(1,length(0:1:210));
Eper_IGBT=zeros(1,length(0:1:210));
Econ_Diodo=zeros(1,length(0:1:210));
Econm_Diodo=zeros(1,length(0:1:210));
Eper_Diodo=zeros(1,length(0:1:210));
El=zeros(1,length(0:1:210));
Econ=zeros(1,length(0:1:210));
Eper=zeros(1,length(0:1:210));

P=zeros(1,length(0:1:210));
Pper=zeros(1,length(0:1:210));
n=zeros(1,length(0:1:210));

for i=0:1:210
    k=k+1;

    if k<=84
    P(k)=(0.1786*i+220)*1000-75000;
    else
    P(k)=(0.0037*i^2-1.8384*i+363.4)*1000-75000;
    end

    for t=0:Tcon:(0.01-Tcon)  %Semiciclo positivo

        %Cálculo de ton y toff
        m=2*sqrt(2)*Vred*sin(2*pi*f*t)/Vdc;
%m*Vdc/2=Vred*sqrt(2)*sin(2*pi*f*t)
        T=Tcon;
        ton=T*m;
        toff=T-ton;

        %Cálculo de Ic
        Il=P(k)*sin(2*pi*f*t)/(Vred*sqrt(2)*3); %Corriente en la bobina para
cada instante t
        Ilmed=(Il+P(k)/(Vred*sqrt(2)*3)*sin(2*pi*f*(t+Tcon)))/2;
        Ic=Ilmed;

        %Cargar valores Eon, Eoff, Err, Vce y Vf
        [Eon,Eoff,Err,Vce,Vf]= Graficas_Graficas_Conv_1_1_6_carga_ESS(Ic);

        %Cálculo pérdidas IGBT
        Econ_IGBT(k)=Econ_IGBT(k)+ton*Vce*Ic; %Energía de conducción del IGBT
        Econm_IGBT(k)=Econm_IGBT(k)+((Eon+Eoff)*(Vdc/Vref)^1.3*1e-3); %Energía
de encendido y apagado del IGBT
        Eper_IGBT(k)=Econ_IGBT(k)+Econm_IGBT(k); %Energía de pérdidas en el
IGBT

        %Cálculo pérdidas Diodo
```

```
        Econ_Diodo(k)=Econ_Diodo(k)+toff*Ic*Vf; %Energía de conduccción del
Diodo
        Econm_Diodo(k)=Econm_Diodo(k)+Err*(Vdc/Vref)^0.6*1e-3; %Energía de
recuperación del Diodo
        Eper_Diodo(k)=Econ_Diodo(k)+Econm_Diodo(k);

        %Cálculo de pérdidas en la bobina
        El(k)=El(k)+Ic^2*RL*Tcon;

        %Pérdidas totales en un semiciclo teniendo en cuenta las 3
ramas(0,01s)
        Eper(k)=3*Eper_IGBT(k)+3*Eper_Diodo(k)+3*El(k);

    end
    %Pérdidas (Potencia)
    Pper(k)=Eper(k)*100;

    n(k)=(P(k)-Pper(k))/P(k)*100;
end

%Potencia media y perdidas (kW)
Pot_Perdida=sum(Pper)/k/1000
Pot_media=sum(P)/k/1000


function [Eon,Eoff,Err,Vce,Vf]=Graficas_Graficas_Conv_1_1_6_carga_ESS(Ic)
       Eon=-3E-20*Ic^3+5E-05*Ic^2+0.0304*Ic+ 6.6429;
       Eoff=5e-05*Ic^2+0.115*Ic+ 6.2143;
       Err=-4e-05*Ic^2+ 0.059*Ic+ 9.3393;
       Vce0=1;
       options = optimoptions('fsolve','MaxIter',500);
       Vce = fsolve(@(Vce)-14.888*Vce^3+ 114.77*Vce^2- 40.848*Vce- 1.4316-
       Ic,Vce0,options);
       Vf0=1;
       Vf = fsolve(@(Vf)3.1197*Vf^5- 25.159*Vf^4+ 60.68*Vf^3+ 22.752*Vf^2-
       3.7026*Vf-Ic- 0.9756,Vf0,options);
end
```

Converter 1.2.5 (ESS charge)

```
%Datos

Pfov=50; %Valor a variar

Fcon=10e3;
Tcon=1/Fcon;
f=50;
Vdc=1000;
L=45e-6;
RL=0.02;
P=(75-Pfov)*1000;
Vred=230;
Vpt=10;
Vref=600;

%Inicializar valores
k=0;

Econ_IGBT=0;
Econm_IGBT=0;
Eper_IGBT=0;
Econ_Diodo=0;
Econm_Diodo=0;
Eper_Diodo=0;
El=0;
Econ=0;
Eper=0;
```

```
    for t=0:Tcon:(0.01-Tcon)  %Semiciclo positivo

        %Cálculo de ton y toff
        m=2*sqrt(2)*Vred*sin(2*pi*f*t)/Vdc;
%m*Vdc/2=Vred*sqrt(2)*sin(2*pi*f*t)
        T=Tcon;
        ton=T*m;
        toff=T-ton;

        %Cálculo de Ic
        Il=P*sin(2*pi*f*t)/(Vred*sqrt(2)*3); %Corriente en la bobina para cada
instante t
        Ilmed=(Il+P/(Vred*sqrt(2)*3)*sin(2*pi*f*(t+Tcon)))/2;
        Ic=Ilmed;

        %Cargar valores Eon, Eoff, Err, Vce y Vf
        [Eon,Eoff,Err,Vce,Vf]=Graficas_Conv_1_2_5_carga_ESS(Ic);

        %Cálculo pérdidas IGBT
        Econ_IGBT=Econ_IGBT+ton*Vce*Ic; %Energía de conducción del IGBT
        Econm_IGBT=Econm_IGBT+((Eon+Eoff)*(Vdc/Vref)^1.3*1e-3); %Energía de
encendido y apagado del IGBT
        Eper_IGBT=Econ_IGBT+Econm_IGBT; %Energía de pérdidas en el IGBT

        %Cálculo pérdidas Diodo
        Econ_Diodo=Econ_Diodo+toff*Ic*Vf; %Energía de conduccción del Diodo
        Econm_Diodo=Econm_Diodo+Err*(Vdc/Vref)^0.6*1e-3; %Energía de
recuperación del Diodo
        Eper_Diodo=Econ_Diodo+Econm_Diodo;

        %Cálculo de pérdidas en la bobina
        El=El+Ic^2*RL*Tcon;

        %Pérdidas totales en un semiciclo teniendo en cuenta las 3
ramas(0,01s)
        Eper=3*Eper_IGBT+3*Eper_Diodo+3*El;

    end

%Pérdidas (Potencia)
Pper=Eper*100

n=(P-Pper)/P*100;



function [Eon,Eoff,Err,Vce,Vf]=Graficas_Conv_1_2_5_carga_ESS(Ic)
       Eon=-3E-20*Ic^3+5E-05*Ic^2+0.0304*Ic+ 6.6429;
       Eoff=5e-05*Ic^2+0.115*Ic+ 6.2143;
       Err=-4e-05*Ic^2+ 0.059*Ic+ 9.3393;
       Vce0=1;
       options = optimoptions('fsolve','MaxIter',500);
       Vce = fsolve(@(Vce)-14.888*Vce^3+ 114.77*Vce^2- 40.848*Vce- 1.4316-
       Ic,Vce0,options);
       Vf0=1;
       Vf = fsolve(@(Vf)3.1197*Vf^5- 25.159*Vf^4+ 60.68*Vf^3+ 22.752*Vf^2-
       3.7026*Vf-Ic- 0.9756,Vf0,options);
end
```

Converter 1.2.5 (BEB charge)

```
%Datos

Pfotov=50e3; %valor a ir variando

Fcon=10e3;
```

```
Tcon=1/Fcon;
f=50;
Vdc=1000;
L=45e-6;
RL=0.02;
Pnom=225e3;
Vred=230;
Vpt=10;
Vref=600;

%Inicializar valores
k=0;

Econ_IGBT=zeros(1,length(0:1:210));
Econm_IGBT=zeros(1,length(0:1:210));
Eper_IGBT=zeros(1,length(0:1:210));
Econ_Diodo=zeros(1,length(0:1:210));
Econm_Diodo=zeros(1,length(0:1:210));
Eper_Diodo=zeros(1,length(0:1:210));
El=zeros(1,length(0:1:210));
Econ=zeros(1,length(0:1:210));
Eper=zeros(1,length(0:1:210));

P=zeros(1,length(0:1:210));
Pper=zeros(1,length(0:1:210));
n=zeros(1,length(0:1:210));

for i=0:1:210
    k=k+1;

    if k<=84
    P(k)=(0.1786*i+220)*1000+Pfotov-75000;
    else
    P(k)=(0.0037*i^2-1.8384*i+363.4)*1000+Pfotov-75000;
    end

    for t=0:Tcon:(0.01-Tcon)  %Semiciclo positivo

        %Cálculo de ton y toff
        m=2*sqrt(2)*Vred*sin(2*pi*f*t)/Vdc;
%m*Vdc/2=Vred*sqrt(2)*sin(2*pi*f*t)
        T=Tcon;
        ton=T*m;
        toff=T-ton;

        %Cálculo de Ic
        Il=P(k)*sin(2*pi*f*t)/(Vred*sqrt(2)*3); %Corriente en la bobina para
cada instante t
        Ilmed=(Il+P(k)/(Vred*sqrt(2)*3)*sin(2*pi*f*(t+Tcon)))/2;
        Ic=Ilmed;

        %Cargar valores Eon, Eoff, Err, Vce y Vf
        [Eon,Eoff,Err,Vce,Vf]=Graficas_Conv_1_2_5_descarga_ESS(Ic);

        %Cálculo pérdidas IGBT
        Econ_IGBT(k)=Econ_IGBT(k)+ton*Vce*Ic; %Energía de conducción del IGBT
        Econm_IGBT(k)=Econm_IGBT(k)+((Eon+Eoff)*(Vdc/Vref)^1.3*1e-3); %Energía
de encendido y apagado del IGBT
        Eper_IGBT(k)=Econ_IGBT(k)+Econm_IGBT(k); %Energía de pérdidas en el
IGBT

        %Cálculo pérdidas Diodo
        Econ_Diodo(k)=Econ_Diodo(k)+toff*Ic*Vf; %Energía de conduccción del
Diodo
        Econm_Diodo(k)=Econm_Diodo(k)+Err*(Vdc/Vref)^0.6*1e-3; %Energía de
recuperación del Diodo
        Eper_Diodo(k)=Econ_Diodo(k)+Econm_Diodo(k);
```

```
        %Cálculo de pérdidas en la bobina
        El(k)=El(k)+Ic^2*RL*Tcon;

        %Cálculo de pérdidas de control
        %Econ(k)=Econ(k)+Pcon*Tcon;              +Econ(k)

        %Pérdidas totales en un semiciclo teniendo en cuenta las 3
ramas(0,01s)
        Eper(k)=3*Eper_IGBT(k)+3*Eper_Diodo(k)+3*El(k);

    end
    %Pérdidas (Potencia)
    Pper(k)=Eper(k)*100;

    n(k)=(P(k)-Pper(k))/P(k)*100;
end

%Potencia media y perdidas (kW)
Pot_Perdida=sum(Pper)/k/1000
Pot_media=sum(P)/k/1000


function [Eon,Eoff,Err,Vce,Vf]=Graficas_Conv_1_2_5_descarga_ESS(Ic)
       Eon=-3E-20*Ic^3+5E-05*Ic^2+0.0304*Ic+ 6.6429;
       Eoff=5e-05*Ic^2+0.115*Ic+ 6.2143;
       Err=-4e-05*Ic^2+ 0.059*Ic+ 9.3393;
       Vce0=1;
       options = optimoptions('fsolve','MaxIter',500);
       Vce = fsolve(@(Vce)-14.888*Vce^3+ 114.77*Vce^2- 40.848*Vce- 1.4316-
       Ic,Vce0,options);
       Vf0=1;
       Vf = fsolve(@(Vf)3.1197*Vf^5- 25.159*Vf^4+ 60.68*Vf^3+ 22.752*Vf^2-
       3.7026*Vf-Ic- 0.9756,Vf0,options);
End
```

Converter 2.1

```
%Datos

Pfotov=50; %Valor a ir variando

Fcon=16e3;
Tcon=1/Fcon;
f=50;
Vdc=1000;
L=83e-6;
RL=0.036;
P=(75-Pfotov)*1000;
Vred=230;
Vpt=10;
Vref=600;

%Inicializar valores
k=0;

Econ_IGBT=0;
Econm_IGBT=0;
Eper_IGBT=0;
Econ_Diodo=0;
Econm_Diodo=0;
Eper_Diodo=0;
El=0;
Econ=0;
Eper=0;

    for t=0:Tcon:(0.01-Tcon)  %Semiciclo positivo
```

```
        %Cálculo de ton y toff
        m=2*sqrt(2)*Vred*sin(2*pi*f*t)/Vdc;
%m*Vdc/2=Vred*sqrt(2)*sin(2*pi*f*t)
        T=Tcon;
        ton=T*m;
        toff=T-ton;

        %Cálculo de Ic
        Il=P*sin(2*pi*f*t)/(Vred*sqrt(2)*3); %Corriente en la bobina para cada
instante t
        Ilmed=(Il+P/(Vred*sqrt(2)*3)*sin(2*pi*f*(t+Tcon)))/2;
        Ic=Ilmed;

        %Cargar valores Eon, Eoff, Err, Vce y Vf
        [Eon,Eoff,Err,Vce,Vf]=Graficas_Conv_2_1(Ic);

        %Cálculo pérdidas IGBT
        Econ_IGBT=Econ_IGBT+ton*Vce*Ic; %Energía de conducción del IGBT
        Econm_IGBT=Econm_IGBT+((Eon+Eoff)*(Vdc/Vref)^1.3*1e-3); %Energía de
encendido y apagado del IGBT
        Eper_IGBT=Econ_IGBT+Econm_IGBT; %Energía de pérdidas en el IGBT

        %Cálculo pérdidas Diodo
        Econ_Diodo=Econ_Diodo+toff*Ic*Vf; %Energía de conduccción del Diodo
        Econm_Diodo=Econm_Diodo+Err*(Vdc/Vref)^0.6*1e-3; %Energía de
recuperación del Diodo
        Eper_Diodo=Econ_Diodo+Econm_Diodo;

        %Cálculo de pérdidas en la bobina
        El=El+Ic^2*RL*Tcon;

        %Pérdidas totales en un semiciclo teniendo en cuenta las 3
ramas(0,01s)
        Eper=3*Eper_IGBT+3*Eper_Diodo+3*El;

    end

%Pérdidas (Potencia)
Pper=Eper*100

n=(P-Pper)/P*100;


function [Eon,Eoff,Err,Vce,Vf]=Graficas_Conv_2_1(Ic)
       Eon=0.0006*Ic^2- 0.0306*Ic+ + 7.8;
       Eoff=-3E-05*Ic^2+0.115*Ic+ 2.12;
       Err=3E-07*Ic^3- 0.0002*Ic^2+ 0.0757*Ic+ 2.3;
       Vce0=1;
       options = optimoptions('fsolve','MaxIter',500);
       Vce = fsolve(@(Vce)-1.0982*Vce^6+14.254*Vce^5-67.149*Vce^4+131.19*Vce^3-
       62.961*Vce^2+5.984*Vce+0.0164-Ic,Vce0,options);
       Vf0=1;
       Vf = fsolve(@(Vf)-2.3528*Vf^4+ 10.079*Vf^3+ 23.485*Vf^2- 4.9025*Vf-Ic+
       0.0192,Vf0,options);
end
```

Appendix A.2. Power losses comparation between converter 1.1.1 with and without interleaving technique

```
%Datos
ramas=3; %ramas interleaving
Fcon=10e3;
Fcon_inter=Fcon/ramas;
Tcon=1/Fcon;
Tcon_inter=Tcon*ramas;
f=50;
```

```
Vdc=1000;
L=40.4e-6;
L_inter=L;
RL=0.018;
RL_inter=RL;
Pnom=250e3;
Vred=230;
Vref=600;
C=63.3E-6;
Rc=0.13;

%Inicializar valores
k=0;

Econ_IGBT=zeros(1,length(0:2500:Pnom));
Econm_IGBT=zeros(1,length(0:2500:Pnom));
Eper_IGBT=zeros(1,length(0:2500:Pnom));
Econ_Diodo=zeros(1,length(0:2500:Pnom));
Econm_Diodo=zeros(1,length(0:2500:Pnom));
Eper_Diodo=zeros(1,length(0:2500:Pnom));
El=zeros(1,length(0:2500:Pnom));
Econd=zeros(1,length(0:2500:Pnom));
Econ=zeros(1,length(0:2500:Pnom));
Eper=zeros(1,length(0:2500:Pnom));

Econ_IGBT_inter=zeros(1,length(0:2500:Pnom));
Econm_IGBT_inter=zeros(1,length(0:2500:Pnom));
Eper_IGBT_inter=zeros(1,length(0:2500:Pnom));
Econ_Diodo_inter=zeros(1,length(0:2500:Pnom));
Econm_Diodo_inter=zeros(1,length(0:2500:Pnom));
Eper_Diodo_inter=zeros(1,length(0:2500:Pnom));
El_inter=zeros(1,length(0:2500:Pnom));
Econ_inter=zeros(1,length(0:2500:Pnom));
Econd_inter=zeros(1,length(0:2500:Pnom));
Eper_inter=zeros(1,length(0:2500:Pnom));

P=zeros(1,length(0:2500:Pnom));
Pper=zeros(1,length(0:2500:Pnom));
Pper_inter=zeros(1,length(0:2500:Pnom));
n=zeros(1,length(0:2500:Pnom));
n_inter=zeros(1,length(0:2500:Pnom));

for j=0:2500:Pnom
    k=k+1;
    P(k)=j;

    %Sin interleaving
    for t=0:Tcon:(0.01-Tcon)  %Semiciclo positivo

        %Cálculo de ton y toff
        m=2*sqrt(2)*Vred*sin(2*pi*f*t)/Vdc;
%m*Vdc/2=Vred*sqrt(2)*sin(2*pi*f*t)

        T=Tcon;
        ton=T*m;
        toff=T-ton;

        %Cálculo de Ic
        Il=P(k)*sin(2*pi*f*t)/(Vred*sqrt(2)*3); %Corriente en la bobina para
cada instante t
        Ilmed=(Il+P(k)/(Vred*sqrt(2)*3)*sin(2*pi*f*(t+Tcon)))/2;
        Ic=Ilmed;

        %Cargar valores Eon, Eoff, Err, Vce y Vf
        [Eon,Eoff,Err,Vce,Vf]=Graficas_ conv_1_1_1 (Ic);

        %Cálculo pérdidas IGBT
        Econ_IGBT(k)=Econ_IGBT(k)+ton*Vce*Ic; %Energía de conducción del IGBT
```

```
        Econm_IGBT(k)=Econm_IGBT(k)+((Eon+Eoff)*(Vdc/Vref)^1.3*1e-3); %Energía
de encendido y apagado del IGBT
        Eper_IGBT(k)=Econ_IGBT(k)+Econm_IGBT(k); %Energía de pérdidas en el
IGBT

        %Cálculo pérdidas Diodo
        Econ_Diodo(k)=Econ_Diodo(k)+toff*Ic*Vf; %Energía de conduccción del
Diodo
        Econm_Diodo(k)=Econm_Diodo(k)+Err*(Vdc/Vref)^0.6*1e-3; %Energía de
recuperación del Diodo
        Eper_Diodo(k)=Econ_Diodo(k)+Econm_Diodo(k);

        %Cálculo de pérdidas en la bobina
        El(k)=El(k)+Ic^2*RL*Tcon;

        %Cálculo de pérdidas en el condensador
        Icond=Ic*abs(i^2*(2*pi()*f)*L*C);
        Econd(k)=Econd(k)+Icond^2*Rc*Tcon;

        %Pérdidas totales en un semiciclo (0.01 s) teniendo en cuenta las 3
ramas
        Eper(k)=3*Eper_IGBT(k)+3*Eper_Diodo(k)+3*El(k)+3*Econd(k);

    end

        %Pérdidas (en potencia) y rendimientos
        Pper(k)=Eper(k)*100;
        n(k)=(P(k)-Pper(k))/P(k)*100;

    %Con interleaving
    for t_inter=0:Tcon_inter:(0.01-Tcon_inter)  %Semiciclo positivo

        %Cálculo de ton y toff
        m=2*sqrt(2)*Vred*sin(2*pi*f*t_inter)/Vdc;
%m*Vdc/2=Vred*sqrt(2)*sin(2*pi*f*t)

        T_inter=Tcon_inter;
        ton_inter=T_inter*m;
        toff_inter=T_inter-ton_inter;

        %Cálculo de Ic
        Il_inter=P(k)*sin(2*pi*f*t_inter)/(Vred*sqrt(2)*3); %Corriente en la
bobina para cada instante t

Ilmed_inter=(Il_inter+P(k)/(Vred*sqrt(2)*3)*sin(2*pi*f*(t_inter+Tcon_inter)))/
2;
        Ic_inter=Ilmed_inter/ramas;

        %Cargar valores Eon, Eoff, Err, Vce y Vf
        [Eon_inter,Eoff_inter,Err_inter,Vce_inter,Vf_inter]=Graficas_
conv_1_1_1_inter(Ic_inter);

        %Cálculo pérdidas IGBT
        Econ_IGBT_inter(k)=Econ_IGBT_inter(k)+ton_inter*Vce_inter*Ic_inter;
%Energía de conducción del IGBT

Econm_IGBT_inter(k)=Econm_IGBT_inter(k)+((Eon_inter+Eoff_inter)*(Vdc/Vref)^1.3
*1e-3); %Energía de encendido y apagado del IGBT
        Eper_IGBT_inter(k)=Econ_IGBT_inter(k)+Econm_IGBT_inter(k); %Energía de
pérdidas en el IGBT

        %Cálculo pérdidas Diodo
        Econ_Diodo_inter(k)=Econ_Diodo_inter(k)+toff_inter*Ic_inter*Vf_inter;
%Energía de conduccción del Diodo
        Econm_Diodo_inter(k)=Econm_Diodo_inter(k)+Err_inter*(Vdc/Vref)^0.6*1e-
3; %Energía de recuperación del Diodo
        Eper_Diodo_inter(k)=Econ_Diodo_inter(k)+Econm_Diodo_inter(k);
```

```
        %Cálculo de pérdidas en la bobina
        El_inter(k)=El_inter(k)+Ic_inter^2*RL_inter*Tcon_inter;

        %Cálculo de pérdidas en el condensador
        Icond_inter=Ic_inter*abs(i^2*(2*pi()*f)*L*C);
        Econd_inter(k)=Econd_inter(k)+Icond_inter^2*Rc*Tcon;

        %Pérdidas totales en un semiciclo (0.01 s) teniendo en cuenta las 9
ramas

Eper_inter(k)=9*Eper_IGBT_inter(k)+9*Eper_Diodo_inter(k)+9*El_inter(k)+9*Econd
_inter(k);

    end

    %Pérdidas (en potencia: dividir entre 0.01 s) y rendimientos
    Pper_inter(k)=Eper_inter(k)*100;
    n_inter(k)=(P(k)-Pper_inter(k))/P(k)*100;
   end

Pcon_IGBT=100*Econ_IGBT*3;
Pcon_Diodo=100*Econ_Diodo*3;
Pconm_IGBT=100*Econm_IGBT*3;
Pconm_Diodo=100*Econm_Diodo*3;
Pl=El*100*3;
Pcond=Econd*100*3;

Pcon_IGBT_inter=100*Econ_IGBT_inter*9;
Pcon_Diodo_inter=100*Econ_Diodo_inter*9;
Pconm_IGBT_inter=100*Econm_IGBT_inter*9;
Pconm_Diodo_inter=100*Econm_Diodo_inter*9;
Pl_inter=El_inter*100*9;
Pcond_inter=Econd_inter*100*3;


plot(P,Pcon_IGBT)
hold on
plot(P,Pcon_Diodo)
hold on
plot(P,Pconm_IGBT)
hold on
plot(P,Pconm_Diodo)
hold on
plot(P,Pl)
hold on
plot(P,Pcond)
legend({'PconIGBT','PconDiodo','PswIGBT','PswDiodo','P
L','Pcap'},'Location','northwest')
xlabel('Power (W)')
ylabel('Power losses (W)')
title('Power losses in the converter 1.1.1 without interleaving technique')

plot(P,Pcon_IGBT_inter)
hold on
plot(P,Pcon_Diodo_inter)
hold on
plot(P,Pconm_IGBT_inter)
hold on
plot(P,Pconm_Diodo_inter)
hold on
plot(P,Pl_inter)
hold on
plot(P,Pcond)
legend({'PconIGBT','PconDiodo','PswIGBT','PswDiodo','P
L','Pcap'},'Location','northwest')
xlabel('Power (W)')
ylabel('Power losses (W)')
title('Power losses in the converter 1.1.1 with interleaving technique')
```

```
axis([0 2.5e5 0 2500])

plot(P,n)
hold on
plot(P,n_inter)
legend({'without interleaving','with interleaving'},'Location','southeast')
xlabel('Power (W)')
ylabel('Efficiency (%)')
title('Efficiency of the converter 1.1.1')


function [Eon,Eoff,Err,Vce,Vf]=Graficas_conv_1_1_1(Ic)
       Eon=-3E-20*Ic^3+5E-05*Ic^2+0.0304*Ic+ 6.6429;
       Eoff=5e-05*Ic^2+0.115*Ic+ 6.2143;
       Err=-4e-05*Ic^2+ 0.059*Ic+ 9.3393;
       Vce0=1;
       options = optimoptions('fsolve','MaxIter',600);
       Vce = fsolve(@(Vce)-1.3807*Vce^6+ 17.991 *Vce^5-87.239 *Vce^4+
       177.43*Vce^3- 71.274*Vce^2+ 17.646*Vce+ 0.3187-Ic,Vce0,options);
       Vf0=1;
       Vf = fsolve(@(Vf)3.1197*Vf^5- 25.159*Vf^4+ 60.68*Vf^3+ 22.752*Vf^2-
       3.7026*Vf-Ic- 0.9756,Vf0,options);
end


function [Eon_inter,Eoff_inter,Err_inter,Vce_inter,Vf_inter]=Graficas_
conv_1_1_1_inter(Ic_inter)
       Eon_inter=0.0006*Ic_inter^2- 0.0306*Ic_inter+ 7.8;
       Eoff_inter=-3E-05*Ic_inter^2+0.115*Ic_inter+ 2.12;
       Err_inter=3E-07*Ic_inter^3- 0.0002*Ic_inter^2+ 0.0757*Ic_inter+ 2.3;
       Vce0=1;
       options = optimoptions('fsolve','MaxIter',600);
       Vce_inter = fsolve(@(Vce_inter)-1.0982*Vce_inter^6+14.254*Vce_inter^5-
       67.149*Vce_inter^4+131.19*Vce_inter^3-
       62.961*Vce_inter^2+5.984*Vce_inter+0.0164-Ic_inter,Vce0,options);
       Vf0=1;
       Vf_inter = fsolve(@(Vf_inter)-2.3528*Vf_inter^4+ 10.079*Vf_inter^3+
       23.485*Vf_inter^2- 4.9025*Vf_inter-Ic_inter+ 0.0192,Vf0,options);
end
```

APPENDIX B. Datasheets

SEMiX151GAL12E4s

Trench IGBT Modules

SEMiX151GAL12E4s

Features

- Homogeneous Si
- Trench = Trenchgate technology
- $V_{CE(sat)}$ with positive temperature coefficient
- High short circuit capability
- UL recognized, file no. E63532

Typical Applications*

- AC inverter drives
- UPS
- Electronic Welding

Remarks

- Case temperature limited to T_C=125°C max.
- Product reliability results are valid for T_j=150°C

Absolute Maximum Ratings				
Symbol	**Conditions**		**Values**	**Unit**
IGBT				
V_{CES}	T_j = 25 °C		1200	V
I_C	T_j = 175 °C	T_c = 25 °C	232	A
		T_c = 80 °C	179	A
I_{Cnom}			150	A
I_{CRM}	I_{CRM} = 3xI_{Cnom}		450	A
V_{GES}			-20 ... 20	V
t_{psc}	V_{CC} = 800 V $V_{GE} \leq$ 20 V $V_{CES} \leq$ 1200 V	T_j = 150 °C	10	µs
T_j			-40 ... 175	°C
Inverse diode				
I_F	T_j = 175 °C	T_c = 25 °C	189	A
		T_c = 80 °C	141	A
I_{Fnom}			150	A
I_{FRM}	I_{FRM} = 3xI_{Fnom}		450	A
I_{FSM}	t_p = 10 ms, sin 180°, T_j = 25 °C		900	A
T_j			-40 ... 175	°C
Freewheeling diode				
I_F	T_j = 175 °C	T_c = 25 °C	189	A
		T_c = 80 °C	141	A
I_{Fnom}			150	A
I_{FRM}	I_{FRM} = 3xI_{Fnom}		450	A
I_{FSM}	t_p = 10 ms, sin 180°, T_j = 25 °C		900	A
T_j			-40 ... 175	°C
Module				
$I_{t(RMS)}$	$T_{terminal}$ = 80 °C		600	A
T_{stg}			-40 ... 125	°C
V_{isol}	AC sinus 50Hz, t = 1 min		4000	V

Characteristics						
Symbol	**Conditions**		**min.**	**typ.**	**max.**	**Unit**
IGBT						
$V_{CE(sat)}$	I_C = 150 A V_{GE} = 15 V chiplevel	T_j = 25 °C		1.8	2.05	V
		T_j = 150 °C		2.2	2.4	V
V_{CE0}	chiplevel	T_j = 25 °C		0.8	0.9	V
		T_j = 150 °C		0.7	0.8	V
r_{CE}	V_{GE} = 15 V chiplevel	T_j = 25 °C		6.7	7.7	mΩ
		T_j = 150 °C		10.0	10.7	mΩ
$V_{GE(th)}$	V_{GE}=V_{CE}, I_C =6 mA		5	5.8	6.5	V
I_{CES}	V_{GE} =0 V V_{CE} = 1200 V	T_j = 25 °C			2.0	mA
		T_j = 150 °C				mA
C_{ies}	V_{CE} = 25V V_{GE} =0 V	f=1 MHz		9.3		nF
C_{oes}		f=1 MHz		0.58		nF
C_{res}		f=1 MHz		0.51		nF
Q_G	V_{GE} = - 8 V...+ 15 V			850		nC
R_{Gint}	T_j = 25 °C			5.00		Ω

Characteristics						
Symbol	**Conditions**		**min.**	**typ.**	**max.**	**Unit**
$t_{d(on)}$	V_{CC} = 600 V	T_j = 150 °C		204		ns
t_r	I_C = 150 A	T_j = 150 °C		42		ns
E_{on}	V_{GE} = ±15 V	T_j = 150 °C		16.6		mJ
$t_{d(off)}$	$R_{G\ on}$ =1 Ω R_G $_{off}$ =1 Ω	T_j = 150 °C		468		ns
t_f	di/dt_{on} = 3900 A/µs	T_j = 150 °C		91		ns
E_{off}	di/dt_{off} = 2000 A/µs	T_j = 150 °C		18.4		mJ
$R_{th(j-c)}$	per IGBT				0.19	K/W
Inverse diode						
$V_F = V_{EC}$	I_F = 150A	T_j = 25 °C		2.1	2.46	V
	V_{GE} = 0 V chiplevel	T_j = 150 °C		2.1	2.4	V
V_{F0}	chiplevel	T_j = 25 °C	1.1	1.3	1.5	V
		T_j = 150 °C	0.7	0.9	1.1	V
r_F	chiplevel	T_j = 25 °C	4.3	5.6	6.4	mΩ
		T_j = 150 °C	6.7	7.8	8.5	mΩ
I_{RRM}	I_F = 150 A	T_j = 150 °C		115		A
Q_{rr}	di/dt_{off} = 3400 A/µs	T_j = 150 °C		23		µC
E_{rr}	V_{GE} = -15 V V_{CC} = 600 V	T_j = 150 °C		8.9		mJ
$R_{th(j-c)}$	per diode				0.31	K/W
Freewheeling diode						
$V_F = V_{EC}$	I_F = 150A	T_j = 25 °C		2.1	2.46	V
	V_{GE} = 0 V chiplevel	T_j = 150 °C		2.1	2.4	V
V_{F0}	chiplevel	T_j = 25 °C	1.1	1.3	1.5	V
		T_j = 150 °C	0.7	0.9	1.1	V
r_F	chiplevel	T_j = 25 °C	4.3	5.6	6.4	mΩ
		T_j = 150 °C	6.7	7.8	8.5	mΩ
I_{RRM}	I_F = 150 A	T_j = 150 °C		115		A
Q_{rr}	di/dt_{off} = 3400 A/µs	T_j = 150 °C		23		µC
E_{rr}	V_{GE} = -15 V V_{CC} = 600 V	T_j = 150 °C		8.9		mJ
$R_{th(j-c)}$	per diode				0.31	K/W
Module						
L_{CE}				16		nH
$R_{CC'+EE'}$	res., terminal-chip	T_C = 25 °C		0.7		mΩ
		T_C = 125 °C		1		mΩ
$R_{th(c-s)}$	per module			0.075		K/W
M_s	to heat sink (M5)		3		5	Nm
M_t		to terminals (M6)	2.5		5	Nm
						Nm
w					145	g
Temperature Sensor						
R_{100}	T_c=100°C (R_{25}=5 kΩ)			493 ± 5%		Ω
$B_{100/125}$	$R_{(T)}=R_{100}\exp[B_{100/125}(1/T-1/T_{100})]$; T[K];			3550 ±2%		K

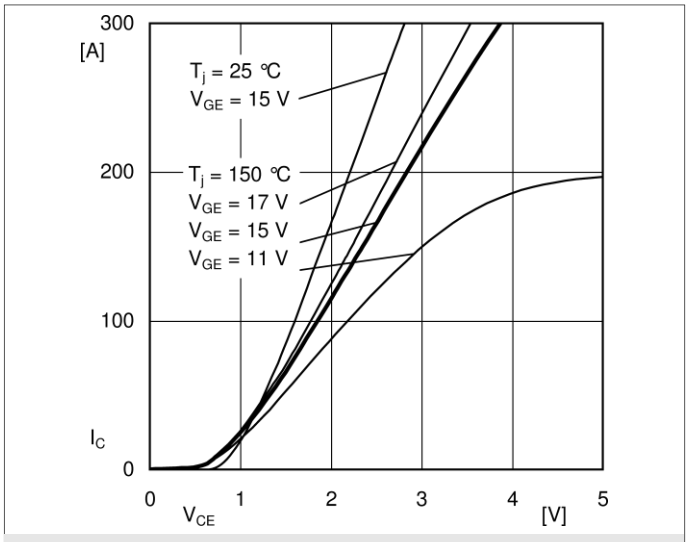

Fig. 1: Typ. output characteristic, inclusive $R_{CC'+EE'}$

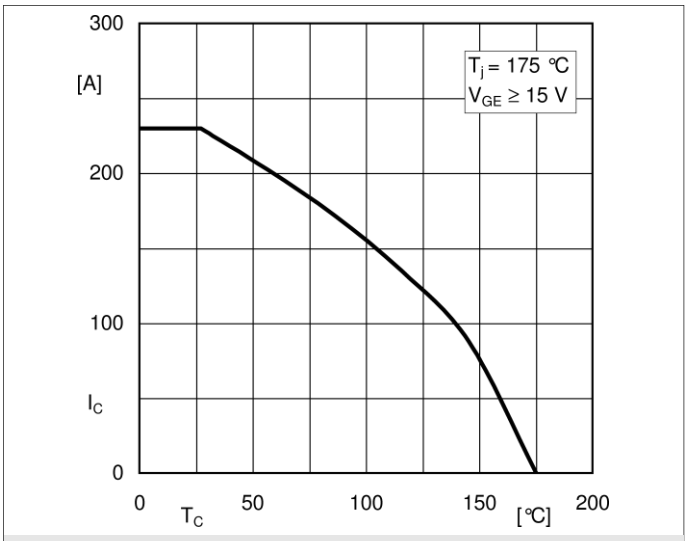

Fig. 2: Rated current vs. temperature $I_C = f(T_C)$

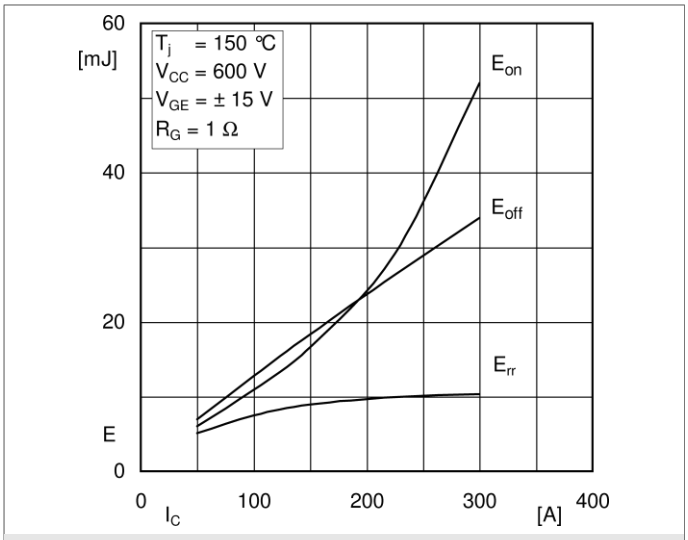

Fig. 3: Typ. turn-on /-off energy = f (I_C)

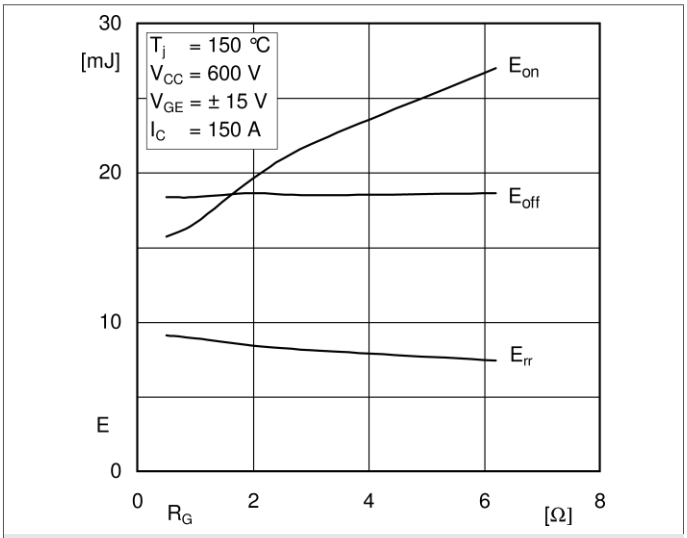

Fig. 4: Typ. turn-on /-off energy = f (R_G)

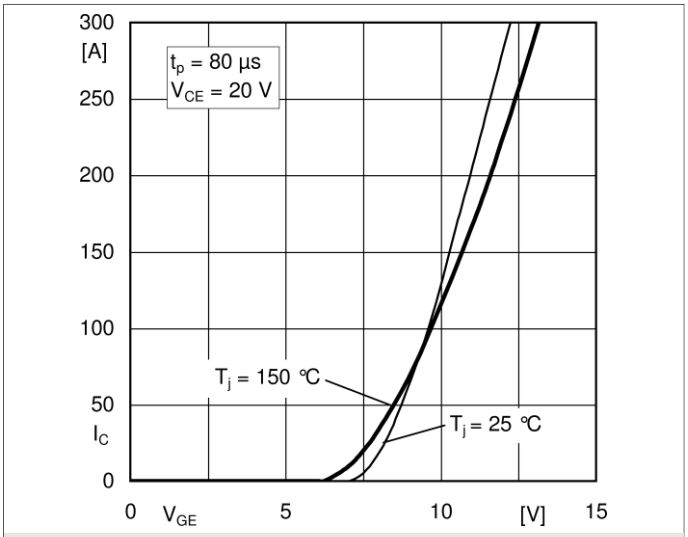

Fig. 5: Typ. transfer characteristic

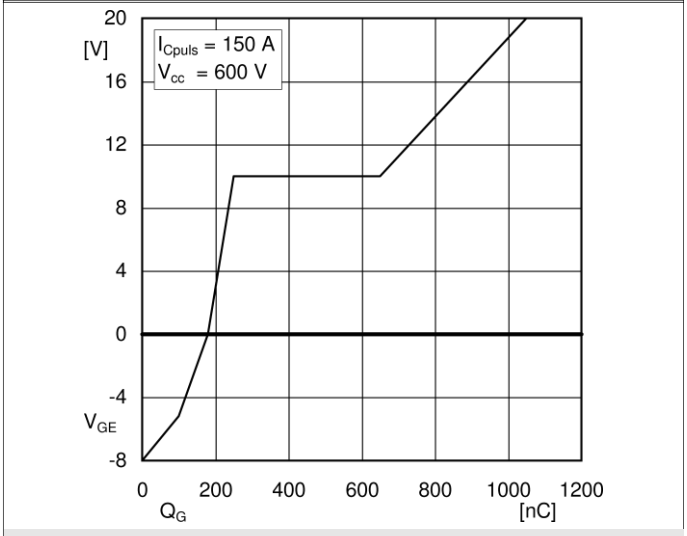

Fig. 6: Typ. gate charge characteristic

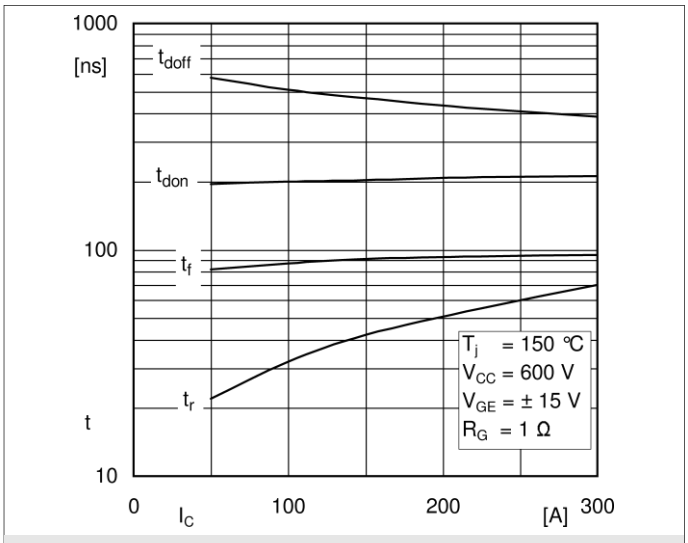

Fig. 7: Typ. switching times vs. I_C

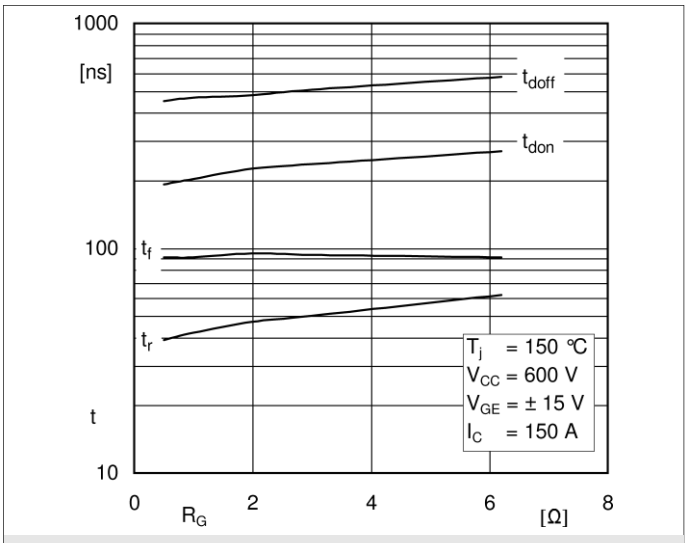

Fig. 8: Typ. switching times vs. gate resistor R_G

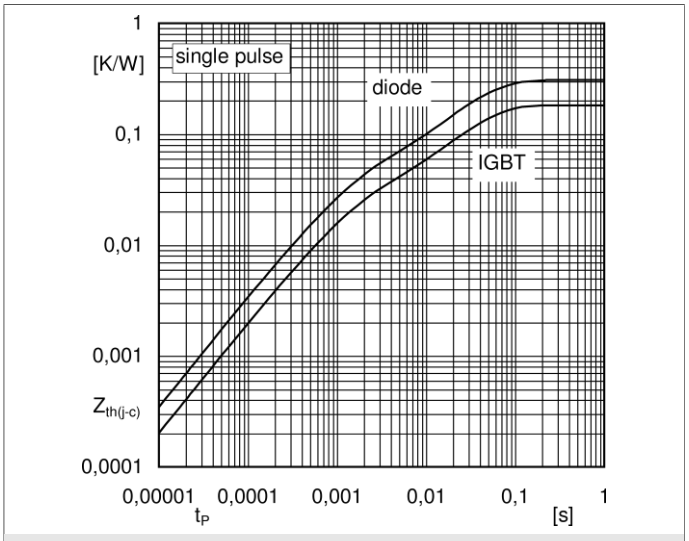

Fig. 9: Typ. transient thermal impedance

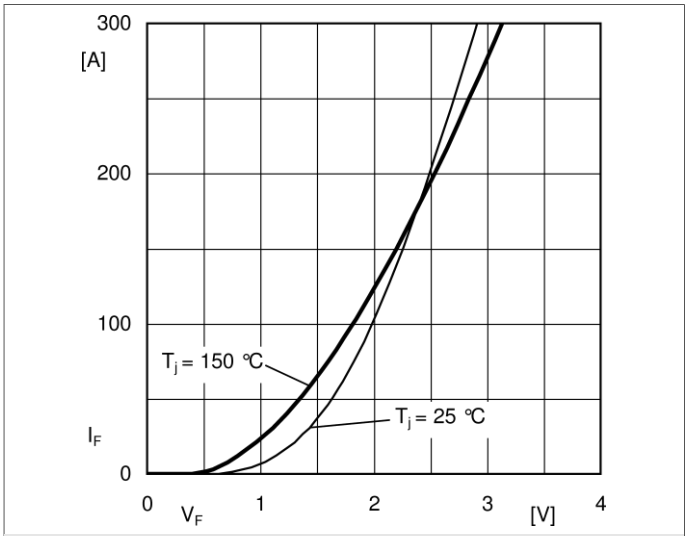

Fig. 10: Typ. CAL diode forward charact., incl. $R_{CC'+ EE'}$

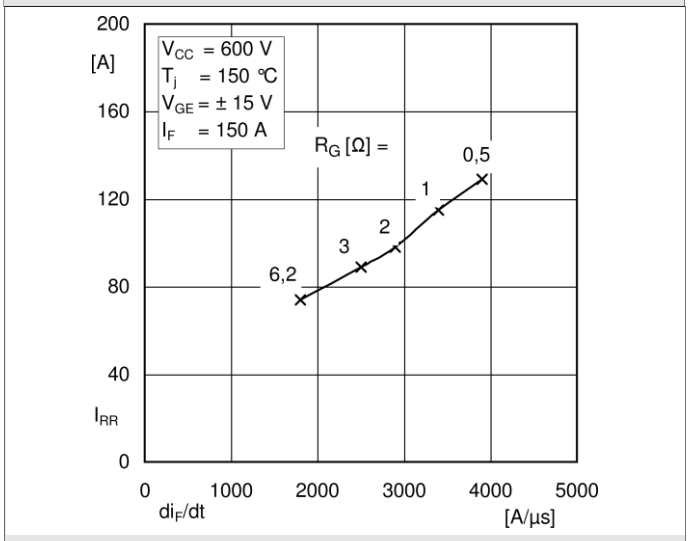

Fig. 11: Typ. CAL diode peak reverse recovery current

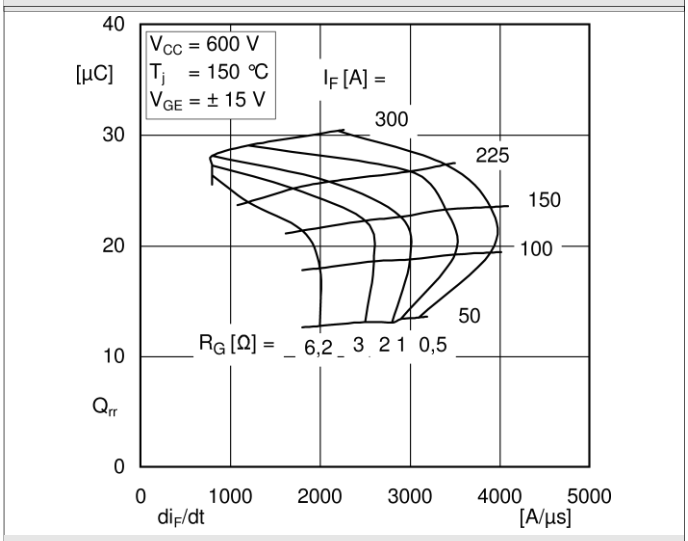

Fig. 12: Typ. CAL diode recovery charge

SEMiX151GB12E4s

SEMiX® 1s

Trench IGBT Modules

SEMiX151GB12E4s

Features

- Homogeneous Si
- Trench = Trenchgate technology
- $V_{CE(sat)}$ with positive temperature coefficient
- High short circuit capability
- UL recognized, file no. E63532

Typical Applications*

- AC inverter drives
- UPS
- Electronic Welding

Remarks

- Case temperature limited to T_C=125°C max.
- Product reliability results are valid for T_j=150°C

Absolute Maximum Ratings

Symbol	Conditions		Values	Unit
IGBT				
V_{CES}	T_j = 25 °C		1200	V
I_C	T_j = 175 °C	T_c = 25 °C	232	A
		T_c = 80 °C	179	A
I_{Cnom}			150	A
I_{CRM}	I_{CRM} = 3xI_{Cnom}		450	A
V_{GES}			-20 ... 20	V
t_{psc}	V_{CC} = 800 V V_{GE} ≤ 20 V V_{CES} ≤ 1200 V	T_j = 150 °C	10	µs
T_j			-40 ... 175	°C
Inverse diode				
I_F	T_j = 175 °C	T_c = 25 °C	189	A
		T_c = 80 °C	141	A
I_{Fnom}			150	A
I_{FRM}	I_{FRM} = 3xI_{Fnom}		450	A
I_{FSM}	t_p = 10 ms, sin 180°, T_j = 25 °C		900	A
T_j			-40 ... 175	°C
Module				
$I_{t(RMS)}$	$T_{terminal}$ = 80 °C		600	A
T_{stg}			-40 ... 125	°C
V_{isol}	AC sinus 50Hz, t = 1 min		4000	V

Characteristics

Symbol	Conditions		min.	typ.	max.	Unit
IGBT						
$V_{CE(sat)}$	I_C = 150 A V_{GE} = 15 V chiplevel	T_j = 25 °C		1.8	2.05	V
		T_j = 150 °C		2.2	2.4	V
V_{CE0}	chiplevel	T_j = 25 °C		0.8	0.9	V
		T_j = 150 °C		0.7	0.8	V
r_{CE}	V_{GE} = 15 V chiplevel	T_j = 25 °C		6.7	7.7	mΩ
		T_j = 150 °C		10.0	10.7	mΩ
$V_{GE(th)}$	V_{GE}=V_{CE}, I_C =6 mA		5	5.8	6.5	V
I_{CES}	V_{GE} =0 V V_{CE} = 1200 V	T_j = 25 °C			2.0	mA
		T_j = 150 °C				mA
C_{ies}	V_{CE} = 25V V_{GE} =0 V	f=1 MHz		9.3		nF
C_{oes}		f=1 MHz		0.58		nF
C_{res}		f=1 MHz		0.51		nF
Q_G	V_{GE} = - 8 V...+ 15 V			850		nC
R_{Gint}	T_j = 25 °C			5.00		Ω
$t_{d(on)}$	V_{CC} = 600 V I_C = 150 A V_{GE} = ±15 V $R_{G\ on}$ =1 Ω R_G $_{off}$ =1 Ω di/dt_{on} = 3900 A/µs di/dt_{off} = 2000 A/µs	T_j = 150 °C		204		ns
t_r		T_j = 150 °C		42		ns
E_{on}		T_j = 150 °C		16.6		mJ
$t_{d(off)}$		T_j = 150 °C		468		ns
t_f		T_j = 150 °C		91		ns
E_{off}		T_j = 150 °C		18.4		mJ
$R_{th(j-c)}$	per IGBT				0.19	K/W

Characteristics						
Symbol	**Conditions**		**min.**	**typ.**	**max.**	**Unit**
Inverse diode						
$V_F = V_{EC}$	I_F = 150A V_{GE} = 0 V chiplevel	T_j = 25 °C		2.1	2.46	V
		T_j = 150 °C		2.1	2.4	V
V_{F0}	chiplevel	T_j = 25 °C	1.1	1.3	1.5	V
		T_j = 150 °C	0.7	0.9	1.1	V
r_F	chiplevel	T_j = 25 °C	4.3	5.6	6.4	mΩ
		T_j = 150 °C	6.7	7.8	8.5	mΩ
I_{RRM}	I_F = 150 A di/dt_{off} = 3400 A/µs V_{GE} = -15 V V_{CC} = 600 V	T_j = 150 °C		115		A
Q_{rr}		T_j = 150 °C		23		µC
E_{rr}		T_j = 150 °C		8.9		mJ
$R_{th(j-c)}$	per diode				0.31	K/W
Module						
L_{CE}				16		nH
$R_{CC'+EE'}$	res., terminal-chip	T_C = 25 °C		0.7		mΩ
		T_C = 125 °C		1		mΩ
$R_{th(c-s)}$	per module			0.075		K/W
M_s	to heat sink (M5)		3		5	Nm
M_t		to terminals (M6)	2.5		5	Nm
						Nm
w					145	g
Temperature Sensor						
R_{100}	T_c=100°C (R_{25}=5 kΩ)			493 ± 5%		Ω
$B_{100/125}$	$R_{(T)}=R_{100}\exp[B_{100/125}(1/T-1/T_{100})]$; T[K];			3550 ±2%		K

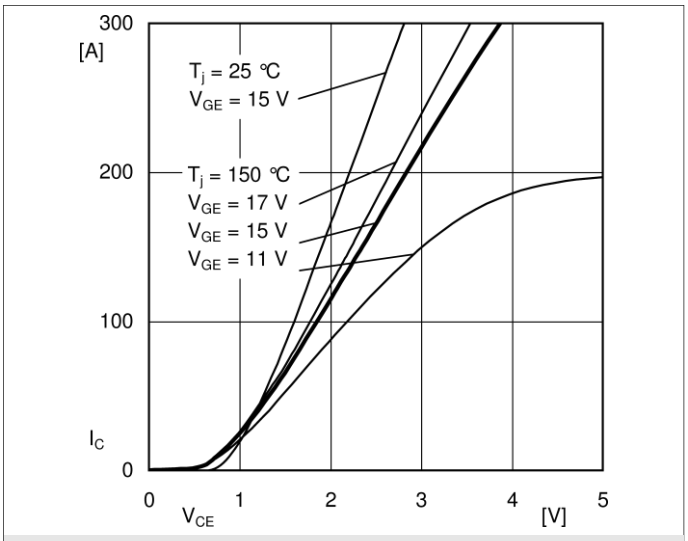

Fig. 1: Typ. output characteristic, inclusive $R_{CC'+ EE'}$

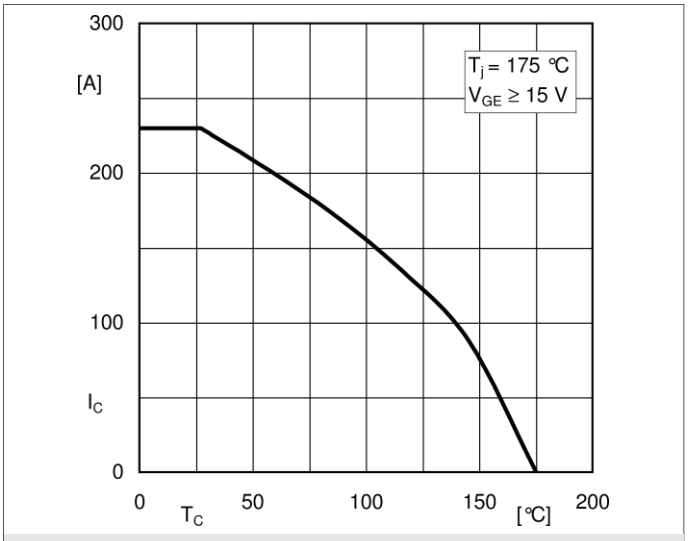

Fig. 2: Rated current vs. temperature $I_C = f(T_C)$

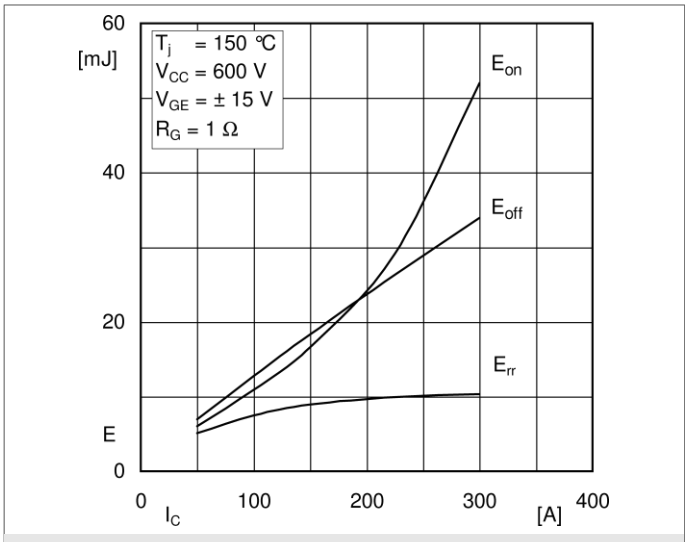

Fig. 3: Typ. turn-on /-off energy = f (I_C)

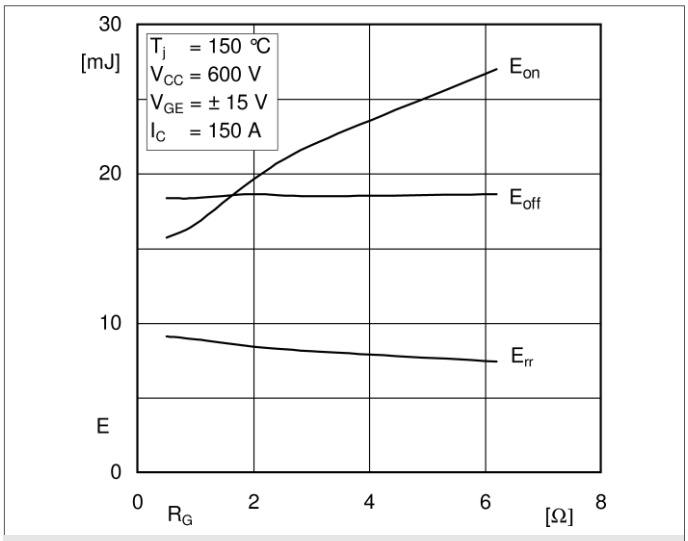

Fig. 4: Typ. turn-on /-off energy = f (R_G)

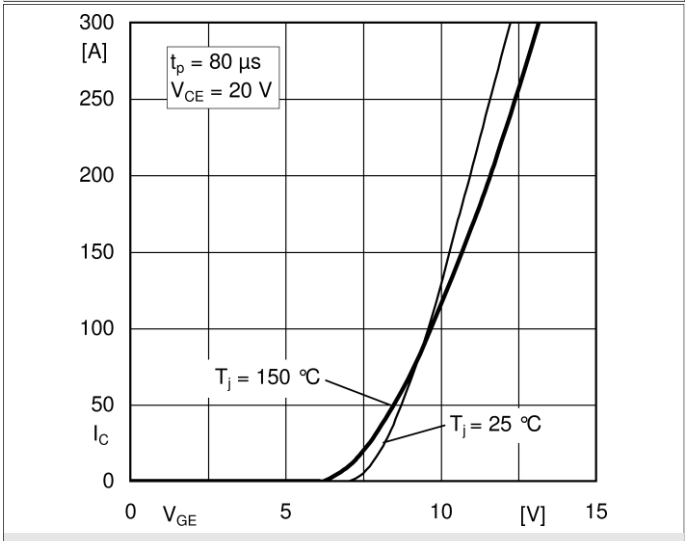

Fig. 5: Typ. transfer characteristic

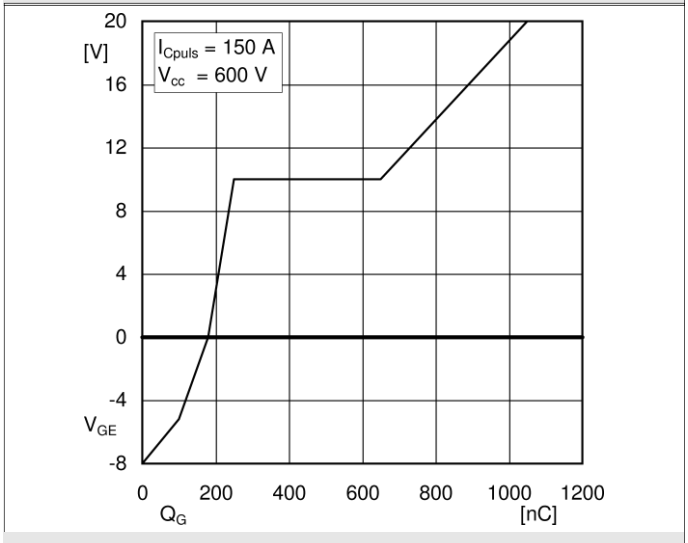

Fig. 6: Typ. gate charge characteristic

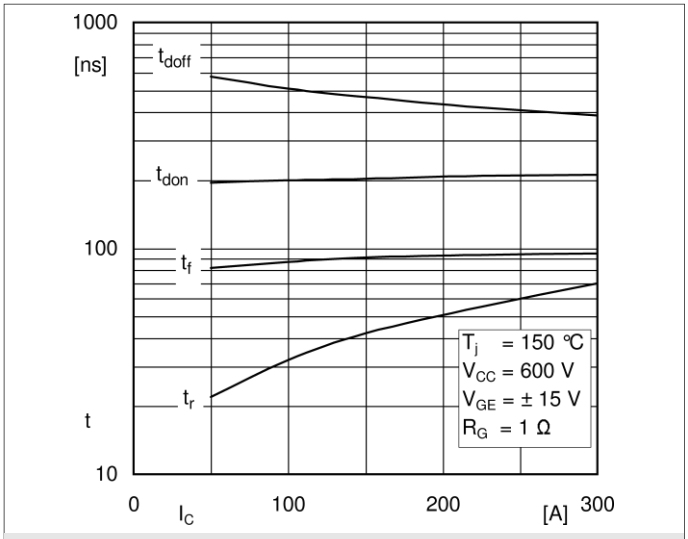

Fig. 7: Typ. switching times vs. I_C

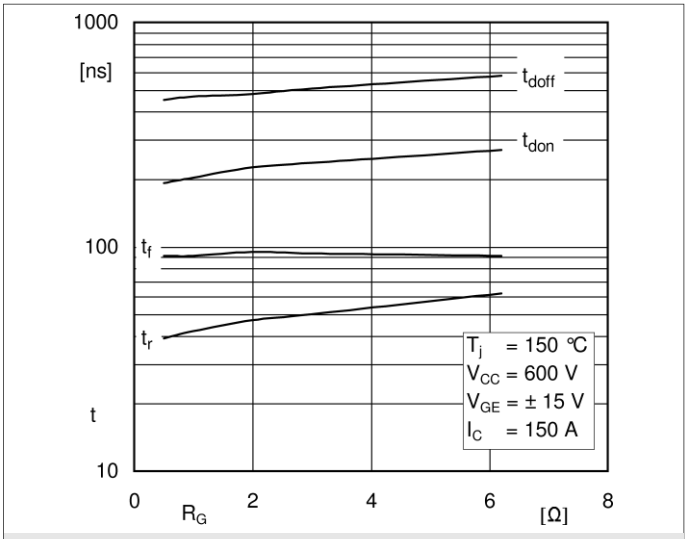

Fig. 8: Typ. switching times vs. gate resistor R_G

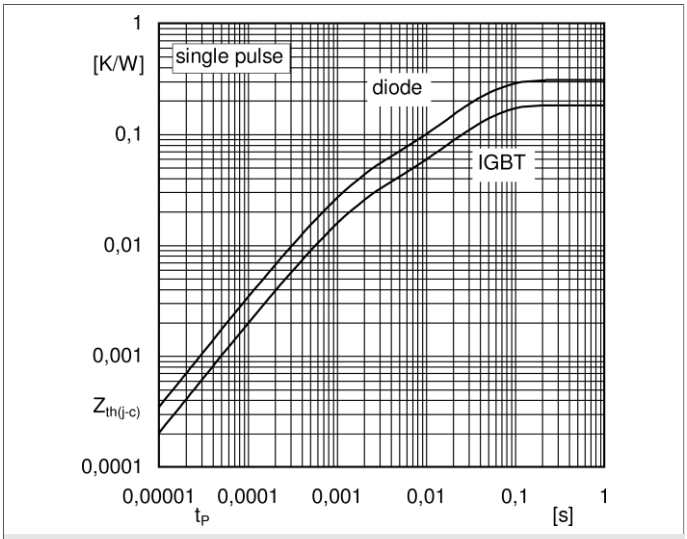

Fig. 9: Typ. transient thermal impedance

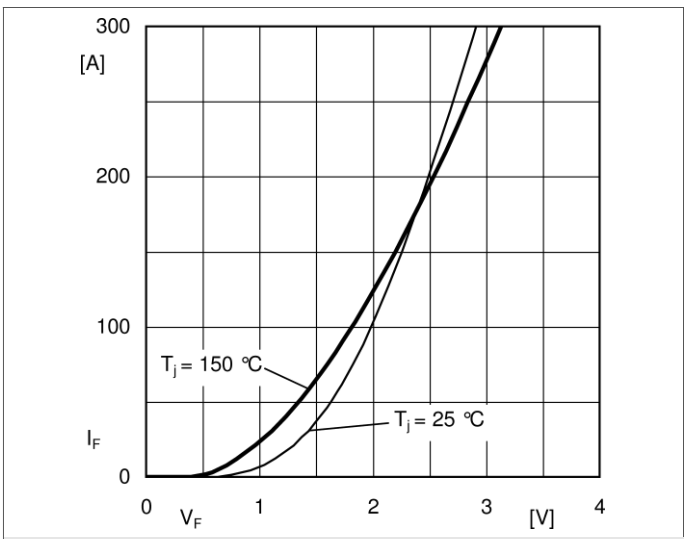

Fig. 10: Typ. CAL diode forward charact., incl. $R_{CC'+ EE'}$

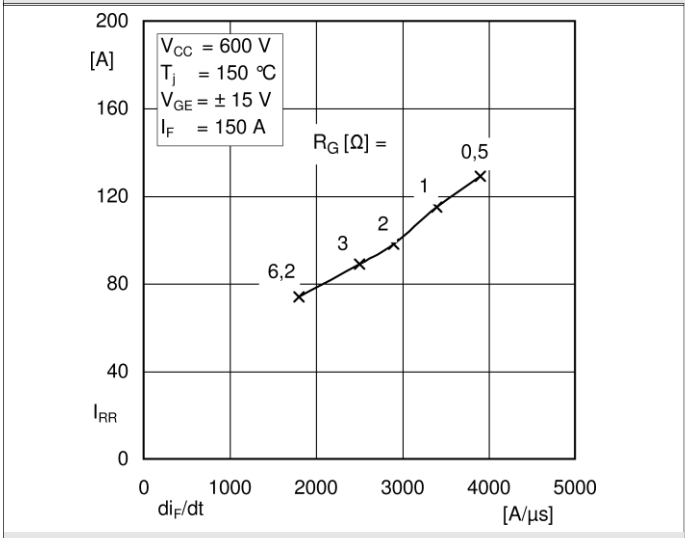

Fig. 11: Typ. CAL diode peak reverse recovery current

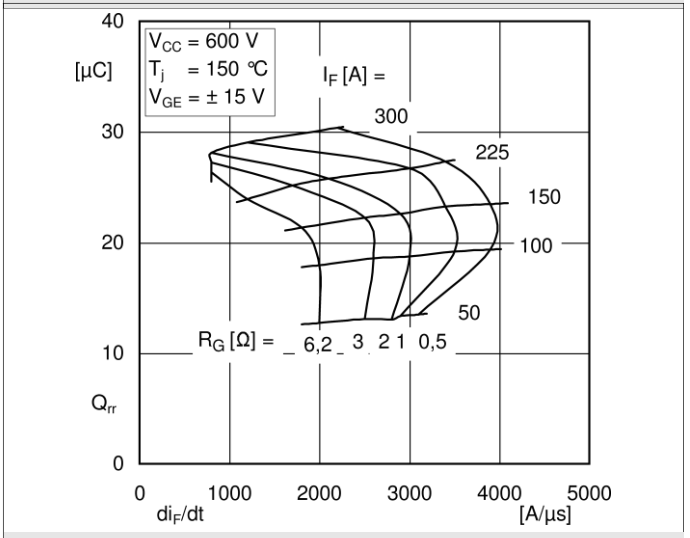

Fig. 12: Typ. CAL diode recovery charge

SEMiX404GB12E4s

SEMiX® 4s

Trench IGBT Modules

SEMiX404GB12E4s

Features

- Homogeneous Si
- Trench = Trenchgate technology
- $V_{CE(sat)}$ with positive temperature coefficient
- High short circuit capability
- UL recognized, file no. E63532

Typical Applications*

- AC inverter drives
- UPS
- Electronic Welding

Remarks

- Case temperature limited to T_C=125°C max.
- Product reliability results are valid for T_j=150°C
- Dynamic values apply to the following combination of resistors: RGon,main = 1,0 Ω

Absolute Maximum Ratings				
Symbol	**Conditions**		**Values**	**Unit**
IGBT				
V_{CES}	T_j = 25 °C		1200	V
I_C	T_j = 175 °C	T_c = 25 °C	618	A
		T_c = 80 °C	475	A
I_{Cnom}			400	A
I_{CRM}	I_{CRM} = 3xI_{Cnom}		1200	A
V_{GES}			-20 ... 20	V
t_{psc}	V_{CC} = 800 V V_{GE} ≤ 20 V V_{CES} ≤ 1200 V	T_j = 150 °C	10	µs
T_j			-40 ... 175	°C
Inverse diode				
I_F	T_j = 175 °C	T_c = 25 °C	440	A
		T_c = 80 °C	329	A
I_{Fnom}			400	A
I_{FRM}	I_{FRM} = 3xI_{Fnom}		1200	A
I_{FSM}	t_p = 10 ms, sin 180°, T_j = 25 °C		1980	A
T_j			-40 ... 175	°C
Module				
$I_{t(RMS)}$	$T_{terminal}$ = 80 °C		600	A
T_{stg}			-40 ... 125	°C
V_{isol}	AC sinus 50Hz, t = 1 min		4000	V

Characteristics						
Symbol	**Conditions**		**min.**	**typ.**	**max.**	**Unit**
IGBT						
$V_{CE(sat)}$	c V_{GE} = 15 V chiplevel	T_j = 25 °C		1.80	2.05	V
		T_j = 150 °C		2.22	2.40	V
V_{CE0}	chiplevel	T_j = 25 °C		0.8	0.9	V
		T_j = 150 °C		0.7	0.8	V
r_{CE}	V_{GE} = 15 V chiplevel	T_j = 25 °C		2.5	2.9	mΩ
		T_j = 150 °C		3.8	4	mΩ
$V_{GE(th)}$	V_{GE}=V_{CE}, I_C = 15.2 mA		5	5.8	6.5	V
I_{CES}	V_{GE} =0 V V_{CE} = 1200 V	T_j = 25 °C			5	mA
		T_j = 150 °C				mA
C_{ies}	V_{CE} = 25V V_{GE} =0 V	f=1 MHz		24.6		nF
C_{oes}		f=1 MHz		1.62		nF
C_{res}		f=1 MHz		1.38		nF
Q_G	V_{GE} = - 8 V...+ 15 V			2260		nC
R_{Gint}	T_j = 25 °C			1.88		Ω
$t_{d(on)}$	V_{CC} = 600 V I_C = 400 A V_{GE} = +15/-15 V $R_{G\ on}$ = 1.7 Ω $R_{G\ off}$ = 1.7 Ω di/dt_{on} = 5800 A/µs di/dt_{off} = 3700 A/µs	T_j = 150 °C		296		ns
t_r		T_j = 150 °C		67		ns
E_{on}		T_j = 150 °C		27		mJ
$t_{d(off)}$		T_j = 150 °C		634		ns
t_f		T_j = 150 °C		137		ns
E_{off}		T_j = 150 °C		59.7		mJ
$R_{th(j-c)}$	per IGBT				0.072	K/W

SEMiX® 4s

Trench IGBT Modules

SEMiX404GB12E4s

Features

- Homogeneous Si
- Trench = Trenchgate technology
- $V_{CE(sat)}$ with positive temperature coefficient
- High short circuit capability
- UL recognized, file no. E63532

Typical Applications*

- AC inverter drives
- UPS
- Electronic Welding

Remarks

- Case temperature limited to T_C=125°C max.
- Product reliability results are valid for T_j=150°C
- Dynamic values apply to the following combination of resistors: RGon,main = 1,0 Ω

Characteristics						
Symbol	**Conditions**		**min.**	**typ.**	**max.**	**Unit**
Inverse diode						
$V_F = V_{EC}$	I_F = 400A V_{GE} = 0 V chiplevel	T_j = 25 °C		2.20	2.52	V
		T_j = 150 °C		2.15	2.47	V
V_{F0}	chiplevel	T_j = 25 °C	1.1	1.3	1.5	V
		T_j = 150 °C	0.7	0.9	1.1	V
r_F	chiplevel	T_j = 25 °C	2	2.3	2.6	mΩ
		T_j = 150 °C	2.6	3.1	3.4	mΩ
I_{RRM}	I_F = 400 A di/dt_{off} = 4900 A/µs V_{GE} = -15 V V_{CC} = 600 V	T_j = 150 °C		315		A
Q_{rr}		T_j = 150 °C		63		µC
E_{rr}		T_j = 150 °C		26.4		mJ
$R_{th(j-c)}$	per diode				0.14	K/W
Module						
L_{CE}				22		nH
$R_{CC'+EE'}$	res., terminal-chip	T_C = 25 °C		0.7		mΩ
		T_C = 125 °C		1		mΩ
$R_{th(c-s)}$	per module			0.03		K/W
M_s	to heat sink (M5)		3		5	Nm
M_t		to terminals (M6)	2.5		5	Nm
						Nm
w					400	g
Temperature Sensor						
R_{100}	T_c=100°C (R_{25}=5 kΩ)			493 ± 5%		Ω
$B_{100/125}$	$R_{(T)}=R_{100}\exp[B_{100/125}(1/T-1/T_{100})]$; T[K];			3550 ±2%		K

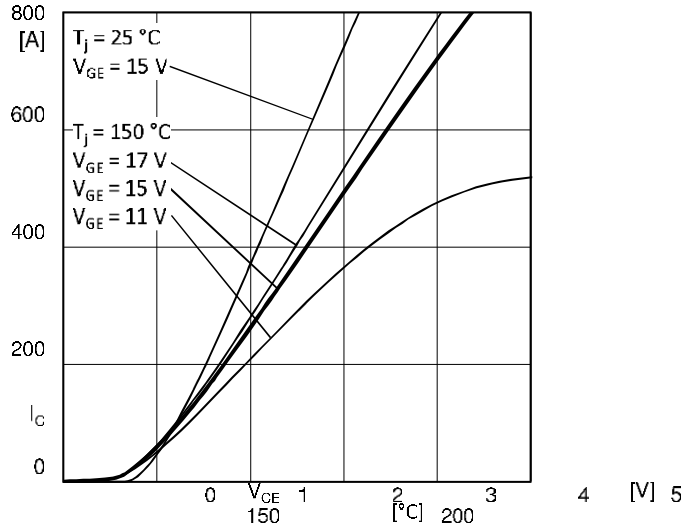

Fig. 1: Typ. output characteristic, inclusive $R_{CC'+ EE'}$

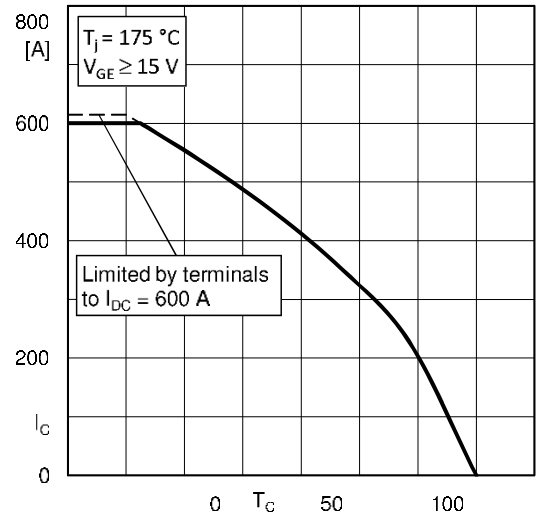

Fig. 2: Rated current vs. temperature $I_C = f(T_C)$

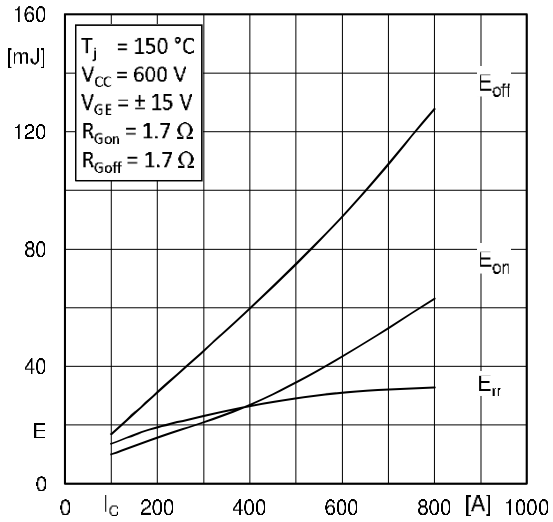

Fig. 3: Typ. turn-on /-off energy = f (I_C)

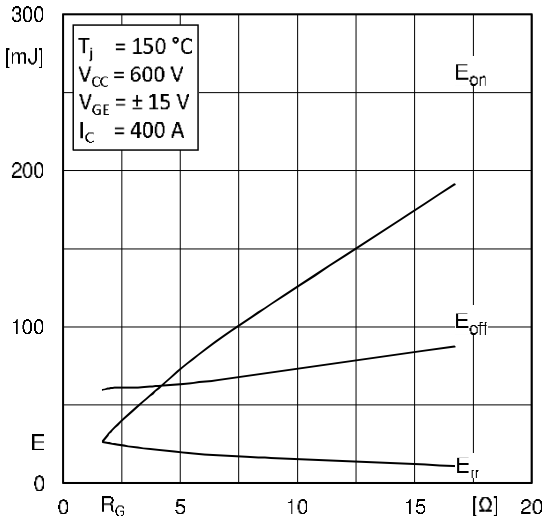

Fig. 4: Typ. turn-on /-off energy = f (R_G)

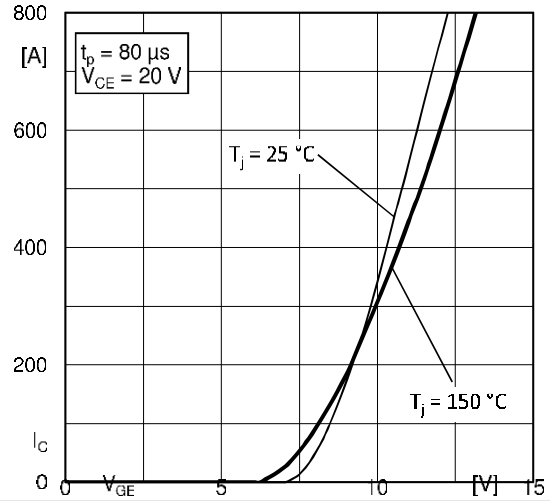

Fig. 5: Typ. transfer characteristic

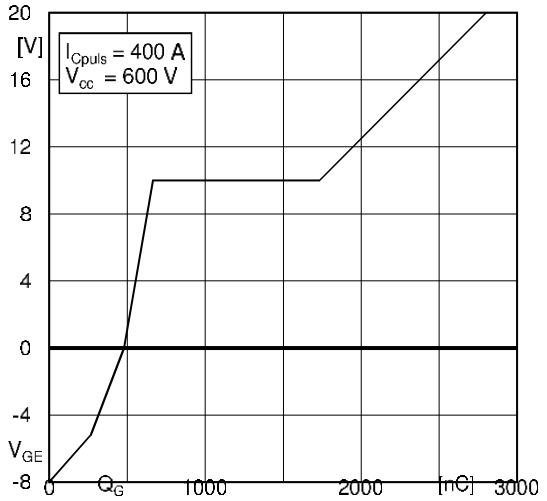

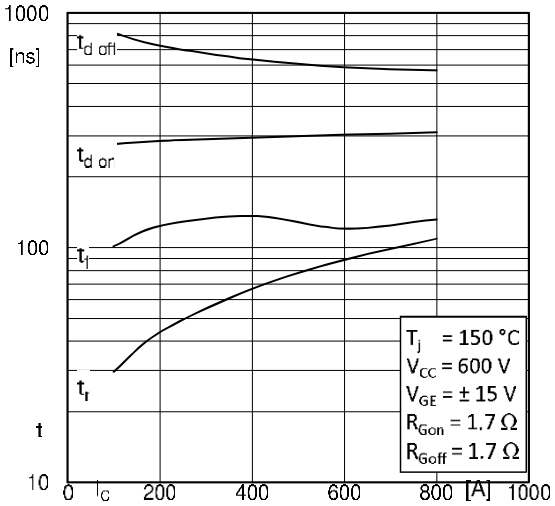

Fig. 7: Typ. switching times vs. I_C

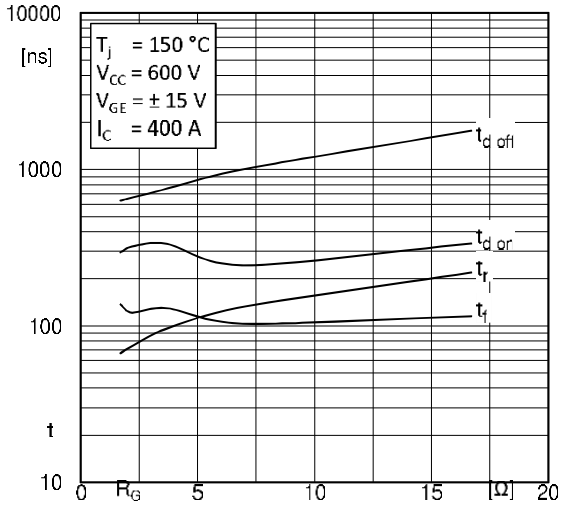

Fig. 8: Typ. switching times vs. gate resistor R_G

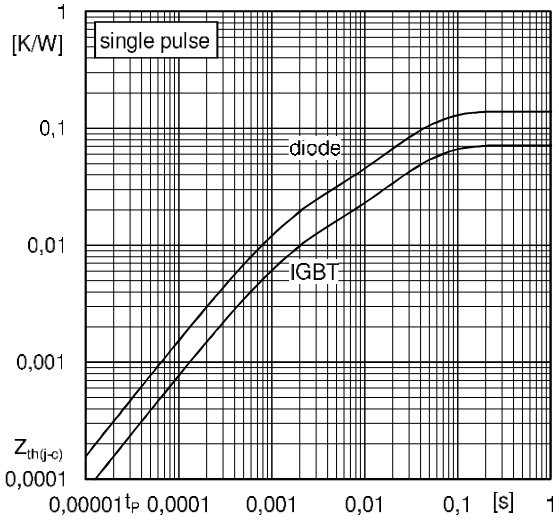

Fig. 9: Typ. transient thermal impedance

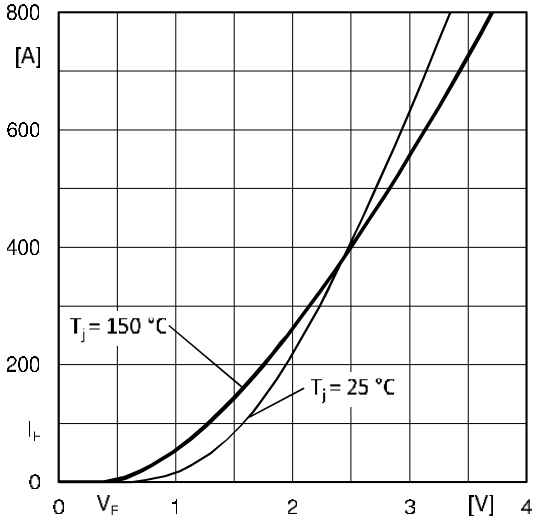

Fig. 10: Typ. CAL diode forward charact., incl. $R_{CC'+\ EE'}$

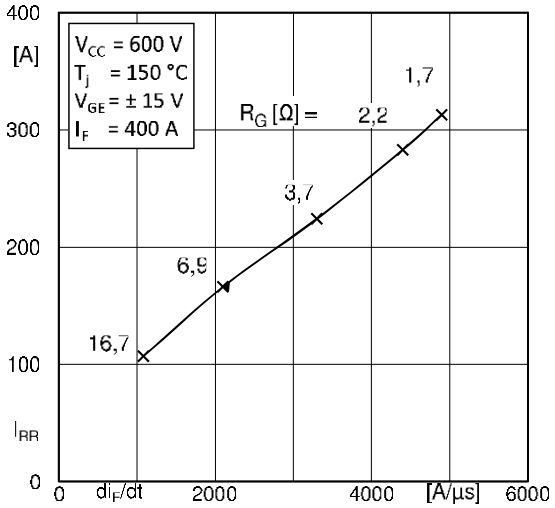

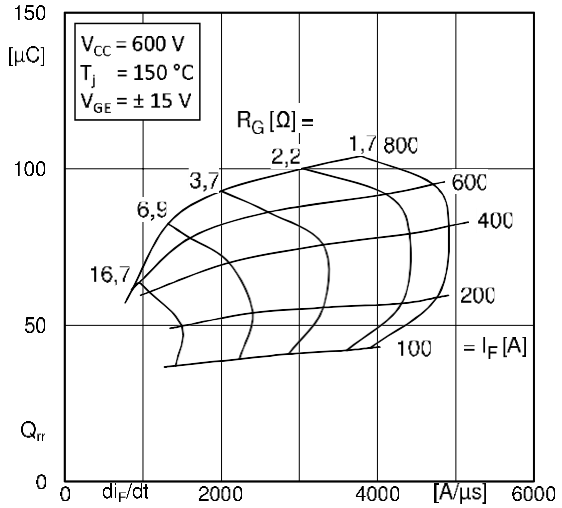

Fig. 11: Typ. CAL diode peak reverse recovery current

SEMiX400GAR12E4

SEMITRANS® 3

IGBT4 Modules

SKM400GAR12E4

Features

- IGBT4 = 4. generation medium fast trench IGBT (Infineon)
- CAL4 = Soft switching 4. generation CAL-diode
- Isolated copper baseplate using DBC technology (Direct Bonded Copper)
- Increased power cycling capability
- With integrated gate resistor
- For higher switching frequenzies up to 12kHz
- UL recognized, file no. E63532

Typical Applications*

- DC/DC – converter
- Brake chopper
- Switched reluctance motor

Remarks

- Case temperature limited to T_c =

Absolute Maximum Ratings				
Symbol	**Conditions**		**Values**	**Unit**
IGBT				
V_{CES}	T_j = 25 °C		1200	V
I_C	T_j = 175 °C	T_c = 25 °C	616	A
		T_c = 80 °C	474	A
I_{Cnom}			400	A
I_{CRM}	I_{CRM} = 3xI_{Cnom}		1200	A
V_{GES}			-20 ... 20	V
t_{psc}	V_{CC} = 800 V $V_{GE} \leq$ 15 V $V_{CES} \leq$ 1200 V	T_j = 150 °C	10	µs
T_j			-40 ... 175	°C
Inverse diode				
I_F	T_j = 175 °C	T_c = 25 °C	440	A
		T_c = 80 °C	329	A
I_{Fnom}			400	A
I_{FRM}	I_{FRM} = 3xI_{Fnom}		1200	A
I_{FSM}	t_p = 10 ms, sin 180°, T_j = 25 °C		1980	A
T_j			-40 ... 175	°C
Freewheeling diode				
I_F	T_j = 175 °C	T_c = 25 °C	440	A
		T_c = 80 °C	329	A
I_{Fnom}			400	A
I_{FRM}	I_{FRM} = 3xI_{Fnom}		1200	A
I_{FSM}	t_p = 10 ms, sin 180°, T_j = 25 °C		1980	A
T_j			-40 ... 175	°C
Module				
$I_{t(RMS)}$	$T_{terminal}$ = 80 °C		500	A
T_{stg}			-40 ... 125	°C
V_{isol}	AC sinus 50 Hz, t = 1 min		4000	V

Characteristics						
Symbol	**Conditions**		**min.**	**typ.**	**max.**	**Unit**
IGBT						
$V_{CE(sat)}$	I_C = 400 A V_{GE} = 15 V chiplevel	T_j = 25 °C		1.80	2.05	V
		T_j = 150 °C		2.20	2.40	V
V_{CE0}	chiplevel	T_j = 25 °C		0.8	0.9	V
		T_j = 150 °C		0.7	0.8	V
r_{CE}	V_{GE} = 15 V chiplevel	T_j = 25 °C		2.50	2.88	mΩ
		T_j = 150 °C		3.75	4.00	mΩ
$V_{GE(th)}$	V_{GE}=V_{CE}, I_C = 15.2 mA		5	5.8	6.5	V
I_{CES}	V_{GE} =0 V V_{CE} = 1200 V	T_j = 25 °C			5	mA
		T_j = 150 °C				mA
C_{ies}	V_{CE} = 25V V_{GE} =0 V	f=1 MHz		24.6		nF
C_{oes}		f=1 MHz		1.62		nF
C_{res}		f=1 MHz		1.38		nF
Q_G	V_{GE} = - 8 V...+ 15 V			2260		nC
R_{Gint}	T_j = 25 °C			1.9		Ω

Characteristics						
Symbol	**Conditions**		**min.**	**typ.**	**max.**	**Unit**
$t_{d(on)}$	V_{CC} = 600 V	T_j = 150 °C		242		ns
t_r	I_C = 400 A	T_j = 150 °C		47		ns
E_{on}	V_{GE} = ±15 V	T_j = 150 °C		33		mJ
$t_{d(off)}$	$R_{G\ on}$ =1 Ω R_G $_{off}$ =1 Ω	T_j = 150 °C		580		ns
t_f	di/dt_{on} = 9700 A/µs	T_j = 150 °C		101		ns
E_{off}	di/dt_{off} = 4300 A/µs	T_j = 150 °C		56		mJ
$R_{th(j-c)}$	per IGBT				0.072	K/W
Inverse diode						
$V_F = V_{EC}$	I_F = 400A	T_j = 25 °C		2.20	2.52	V
	V_{GE} = 0 V chiplevel	T_j = 150 °C		2.15	2.47	V
V_{F0}	chiplevel	T_j = 25 °C		1.3	1.5	V
		T_j = 150 °C		0.9	1.1	V
r_F	chiplevel	T_j = 25 °C		2.3	2.5	mΩ
		T_j = 150 °C		3.1	3.4	mΩ
I_{RRM}	I_F = 400 A	T_j = 150 °C		450		A
Q_{rr}	di/dt_{off} = 8800 A/µs	T_j = 150 °C		68		µC
E_{rr}	V_{GE} = ±15 V V_{CC} = 600 V	T_j = 150 °C		30.5		mJ
$R_{th(j-c)}$	per diode				0.14	K/W
Freewheeling diode						
$V_F = V_{EC}$	I_F = 400A	T_j = 25 °C		2.20	2.52	V
	V_{GE} = 0 V chiplevel	T_j = 150 °C		2.15	2.47	V
V_{F0}	chiplevel	T_j = 25 °C		1.3	1.5	V
		T_j = 150 °C		0.9	1.1	V
r_F	chiplevel	T_j = 25 °C		2.3	2.5	mΩ
		T_j = 150 °C		3.1	3.4	mΩ
I_{RRM}	I_F = 400 A	T_j = 150 °C		450		A
Q_{rr}	di/dt_{off} = 8800 A/µs	T_j = 150 °C		68		µC
E_{rr}	V_{GE} = ±15 V V_{CC} = 600 V	T_j = 150 °C		30.5		mJ
$R_{th(j-c)}$	per Diode				0.14	K/W
Module						
L_{CE}				15	20	nH
$R_{CC'+EE'}$	terminal-chip	T_C = 25 °C		0.25		mΩ
		T_C = 125 °C		0.5		mΩ
$R_{th(c-s)}$	per module			0.02	0.038	K/W
M_s	to heat sink M6		3		5	Nm
M_t		to terminals M6	2.5		5	Nm
						Nm
w					325	g

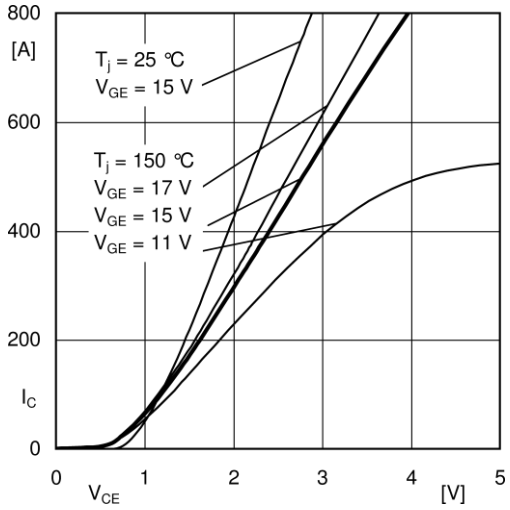

Fig. 1: Typ. output characteristic, inclusive $R_{CC'+ EE'}$

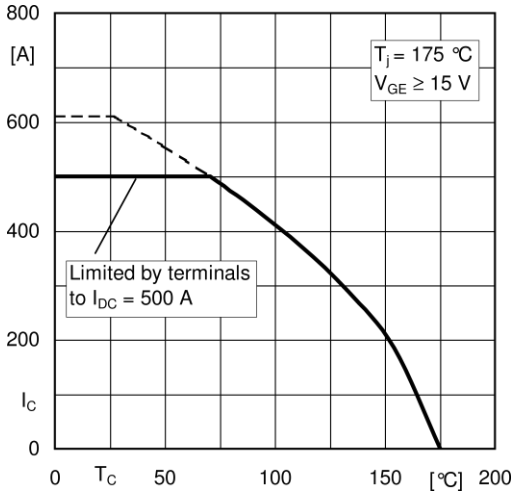

Fig. 2: Rated current vs. temperature $I_C = f(T_C)$

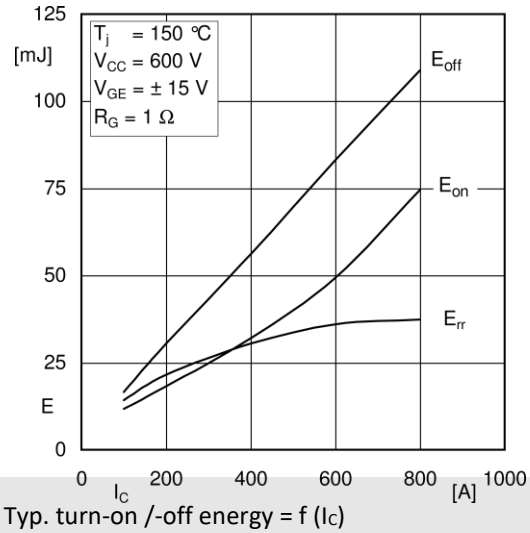

Fig. 3: Typ. turn-on /-off energy = f (I_C)

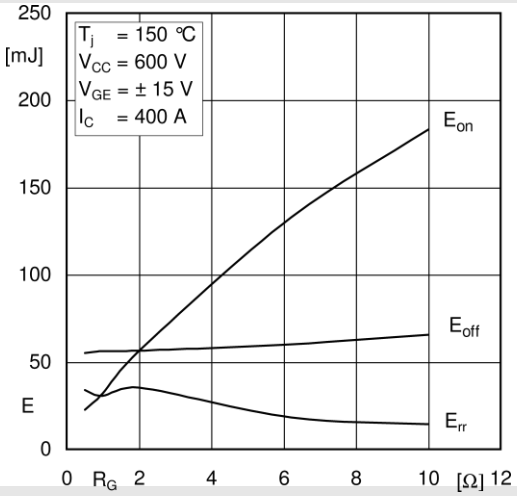

Fig. 4: Typ. turn-on /-off energy = f (R_G)

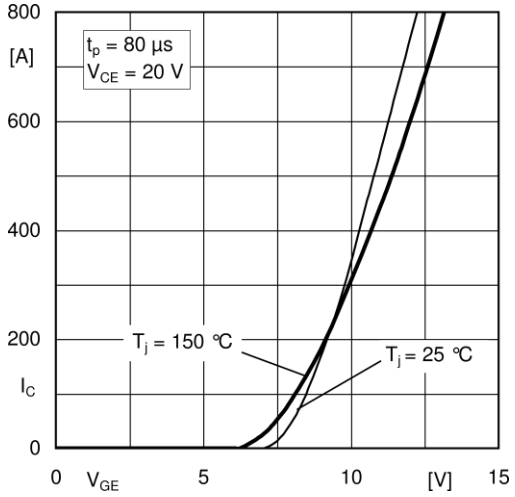

Fig. 5: Typ. transfer characteristic

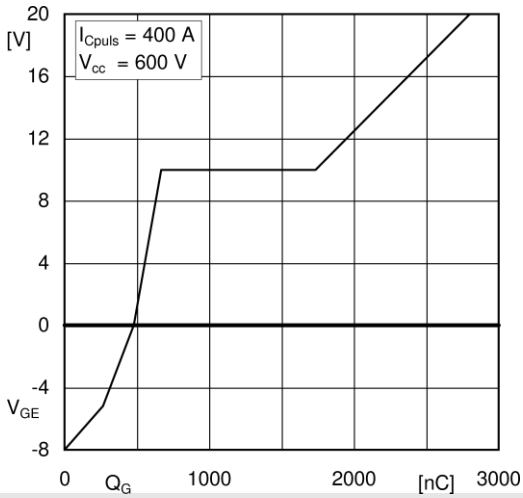

Fig. 6: Typ. gate charge characteristic

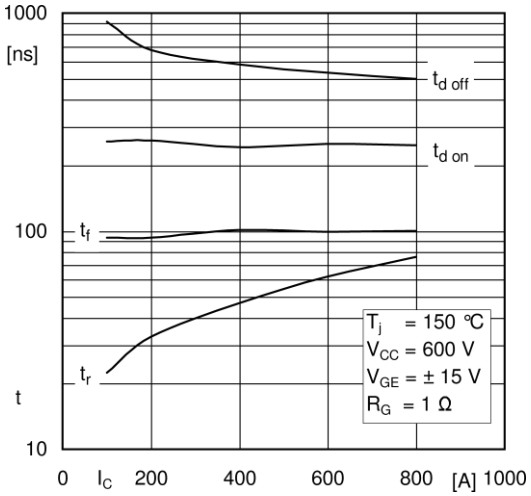

Fig. 7: Typ. switching times vs. I_C

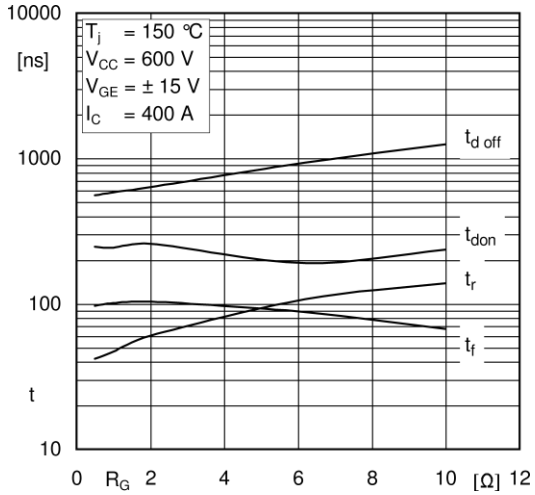

Fig. 8: Typ. switching times vs. gate resistor R_G

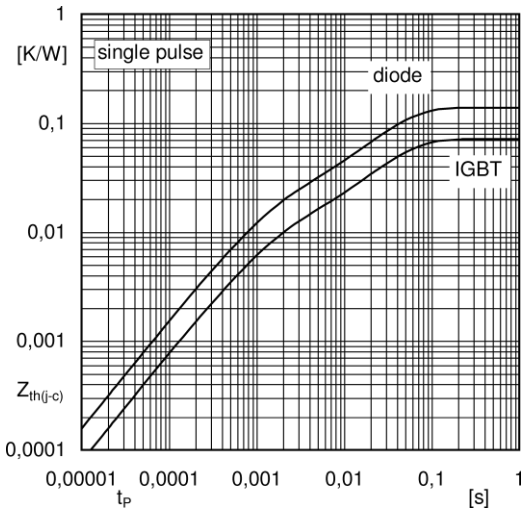

Fig. 9: Transient thermal impedance

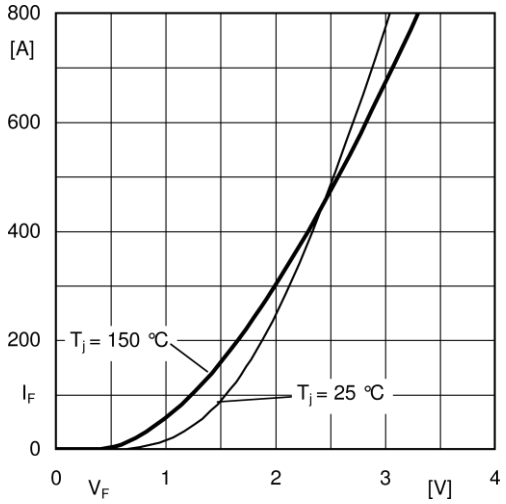

Fig. 10: Typ. CAL diode forward charact., incl. $R_{CC'+\ EE'}$

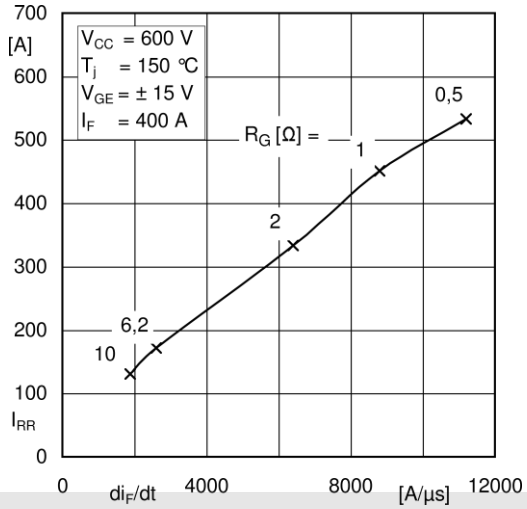

Fig. 11: CAL diode peak reverse recovery current

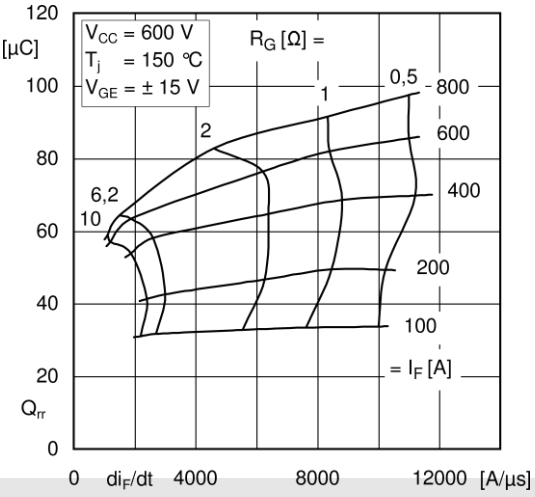

Fig. 12: Typ. CAL diode peak reverse recovery charge

SEMiX603GB12E4p

SEMiX® 3p

Trench IGBT Modules

SEMiX603GB12E4p

Features

- Homogeneous Si
- Trench = Trenchgate technology
- $V_{CE(sat)}$ with positive temperature coefficient
- High short circuit capability
- Press-fit pins as auxiliary contacts
- Thermally optimized ceramic
- UL recognized, file no. E63532

Typical Applications*

- AC inverter drives
- UPS
- Renewable energy systems

Remarks

- Product reliability results are valid for T_j=150°C
- V_{isol} between temperature sensor and power section is only 2500V
- For storage and case

Absolute Maximum Ratings

Symbol	Conditions		Values	Unit
IGBT				
V_{CES}	T_j = 25 °C		1200	V
I_C	T_j = 175 °C	T_c = 25 °C	1110	A
		T_c = 80 °C	853	A
I_{Cnom}			600	A
I_{CRM}	I_{CRM} = 3xI_{Cnom}		1800	A
V_{GES}			-20 ... 20	V
t_{psc}	V_{CC} = 800 V V_{GE} ≤ 15 V V_{CES} ≤ 1200 V	T_j = 150 °C	10	µs
T_j			-40 ... 175	°C
Inverse diode				
V_{RRM}	T_j = 25 °C		1200	V
I_F	T_j = 175 °C	T_c = 25 °C	856	A
		T_c = 80 °C	640	A
I_{Fnom}			600	A
I_{FRM}	I_{FRM} = 3xI_{Fnom}		1800	A
I_{FSM}	t_p = 10 ms, sin 180°, T_j = 25 °C		3456	A
T_j			-40 ... 175	°C
Module				
$I_{t(RMS)}$			600	A
T_{stg}	module without TIM		-40 ... 125	°C
V_{isol}	AC sinus 50Hz, t = 1 min		4000	V

Characteristics

Symbol	Conditions		min.	typ.	max.	Unit
IGBT						
$V_{CE(sat)}$	I_C = 600 A V_{GE} = 15 V chiplevel	T_j = 25 °C		1.80	2.05	V
		T_j = 150 °C		2.03	2.30	V
V_{CE0}	chiplevel	T_j = 25 °C		0.87	1.01	V
		T_j = 150 °C		0.77	0.90	V
r_{CE}	V_{GE} = 15 V chiplevel	T_j = 25 °C		1.55	1.73	m∧
		T_j = 150 °C		2.1	2.3	m∧
$V_{GE(th)}$	V_{GE}=V_{CE}, I_C = 22.2 mA		5.3	5.8	6.3	V
I_{CES}	V_{GE} =0 V, V_{CE} = 1200 V, T_j = 25 °C				5	mA
C_{ies}	V_{CE} = 25V V_{GE} =0 V	f=1 MHz		37.5		nF
C_{oes}		f=1 MHz		2.31		nF
C_{res}		f=1 MHz		2.04		nF
Q_G	V_{GE} = - 8 V...+ 15 V			3450		nC
R_{Gint}	T_j = 25 °C			1.2		∧
$t_{d(on)}$	V_{CC} = 600 V I_C = 600 A V_{GE} = +15/-15 V $R_{G\ on}$ = 1.5 ∧ $R_{G\ off}$ = 1.5 ∧ di/dt_{on} = 6400 A/µs di/dt_{off} = 4150 A/µs du/dt = 3400 V/µs L_s = 21 nH	T_j = 150 °C		260		ns
t_r		T_j = 150 °C		85		ns
E_{on}		T_j = 150 °C		69		mJ
$t_{d(off)}$		T_j = 150 °C		560		ns
t_f		T_j = 150 °C		145		ns
E_{off}		T_j = 150 °C		80		mJ
$R_{th(j-c)}$	per IGBT				0.037	K/W
$R_{th(c-s)}$	per IGBT (λ_{grease}=0.81 W/(m*K))			0.035		K/W
$R_{th(c-s)}$	per IGBT, pre-applied phase change material			0.025		K/W

SEMiX® 3p

Trench IGBT Modules

SEMiX603GB12E4p

Features

- Homogeneous Si
- Trench = Trenchgate technology
- $V_{CE(sat)}$ with positive temperature coefficient
- High short circuit capability
- Press-fit pins as auxiliary contacts
- Thermally optimized ceramic
- UL recognized, file no. E63532

Typical Applications*

- AC inverter drives
- UPS
- Renewable energy systems

Remarks

- Product reliability results are valid for T_j=150°C
- V_{isol} between temperature sensor and power section is only 2500V
- For storage and case

Characteristics						
Symbol	**Conditions**		**min.**	**typ.**	**max.**	**Unit**
Inverse diode						
$V_F = V_{EC}$	I_F = 600A V_{GE} = 0 V chiplevel	T_j = 25 °C		2.08	2.44	V
		T_j = 150 °C		2.08	2.34	V
V_{F0}	chiplevel	T_j = 25 °C		1.39	1.59	V
		T_j = 150 °C		1.08	1.18	V
r_F	chiplevel	T_j = 25 °C		1.16	1.42	m∧
		T_j = 150 °C		1.67	1.93	m∧
I_{RRM}	I_F = 600 A di/dt_{off} = 5100 A/µs V_{GE} = -15 V V_{CC} = 600 V	T_j = 150 °C		475		A
Q_{rr}		T_j = 150 °C		108		µC
E_{rr}		T_j = 150 °C		40		mJ
$R_{th(j-c)}$	per diode				0.065	K/W
$R_{th(c-s)}$	per diode (λ_{grease}=0.81 W/(m*K))			0.039		K/W
$R_{th(c-s)}$	per diode, pre-applied phase change material			0.031		K/W
Module						
L_{CE}				20		nH
$R_{CC'+EE'}$	measured per switch	T_C = 25 °C		1.2		m∧
		T_C = 125 °C		1.65		m∧
$Rth_{(c-s)1}$	calculated without thermal coupling			0.009		K/W
$Rth_{(c-s)2}$	including thermal coupling, Ts underneath module (λ_{grease}=0.81 W/(m*K))			0.014		K/W
$Rth_{(c-s)2}$	including thermal coupling, Ts underneath module, pre-applied phase change material			0.011		K/W
M_s	to heat sink (M5)		3		6	Nm
M_t		to terminals (M6)	3		6	Nm
						Nm
w					350	g
Temperature Sensor						
R_{100}	T_c=100°C (R_{25}=5 k∧)			493 ± 5%		∧
$B_{100/125}$	$R_{(T)}=R_{100}\exp[B_{100/125}(1/T-1/T_{100})]$; T[K];			3550 ±2%		K

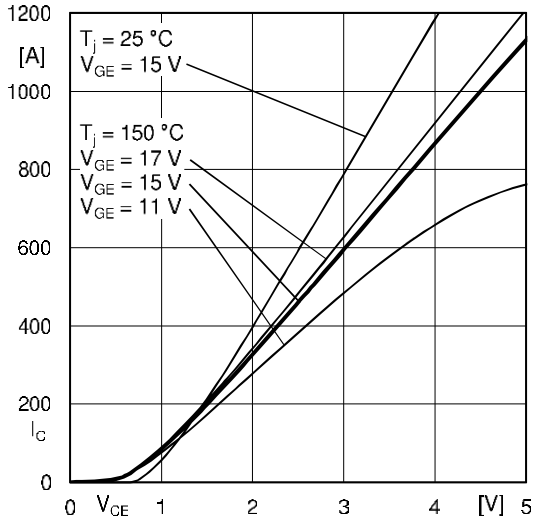

Fig. 1: Typ. output characteristic, inclusive $R_{CC'+EE'}$

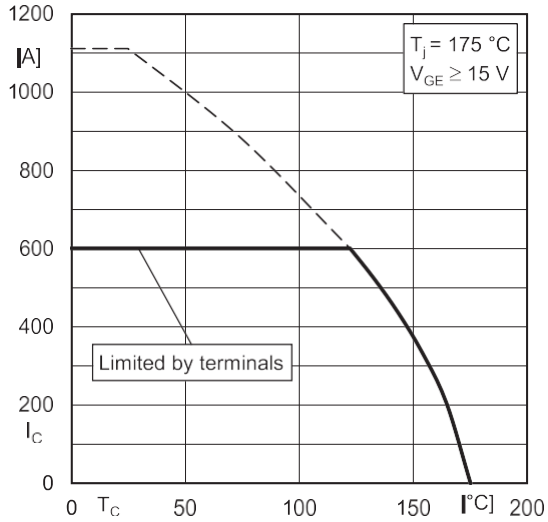

Fig. 2: Rated current vs. temperature $I_C = f(T_C)$

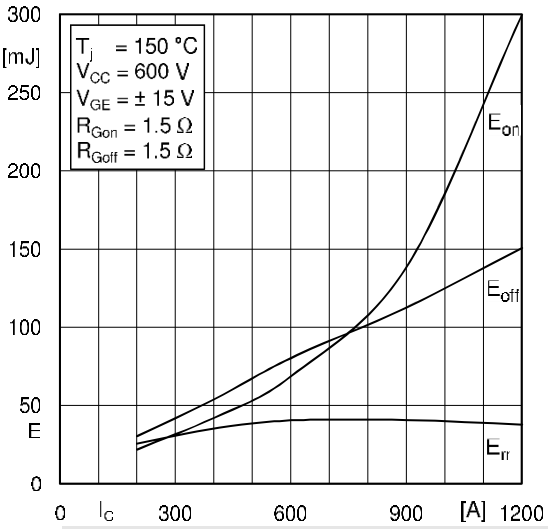

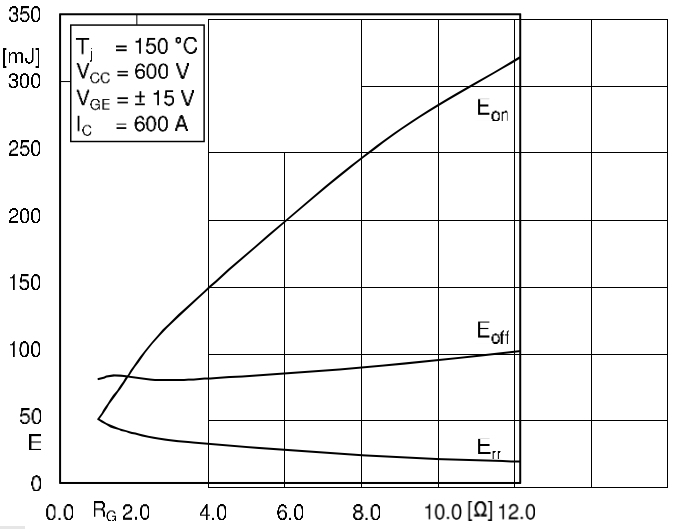

Fig. 3: Typ. turn-on /-off energy = f (I_C)

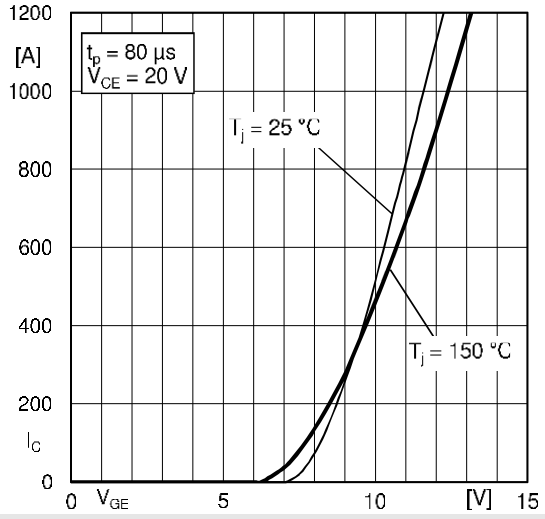

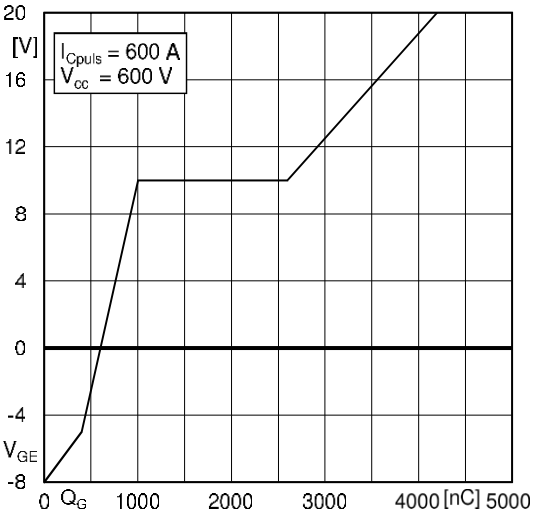

Fig. 5: Typ. transfer characteristic

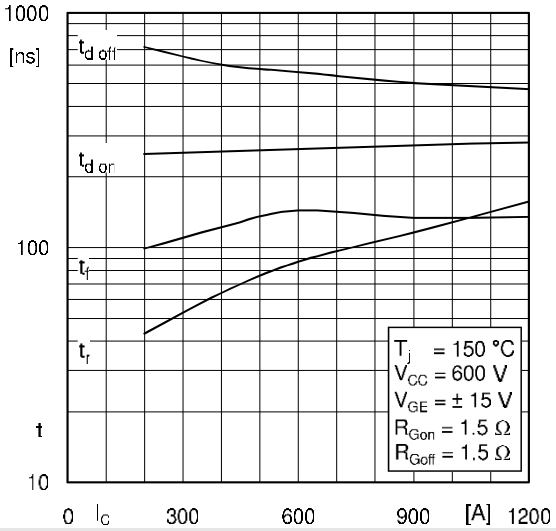

Fig. 7: Typ. switching times vs. I_C

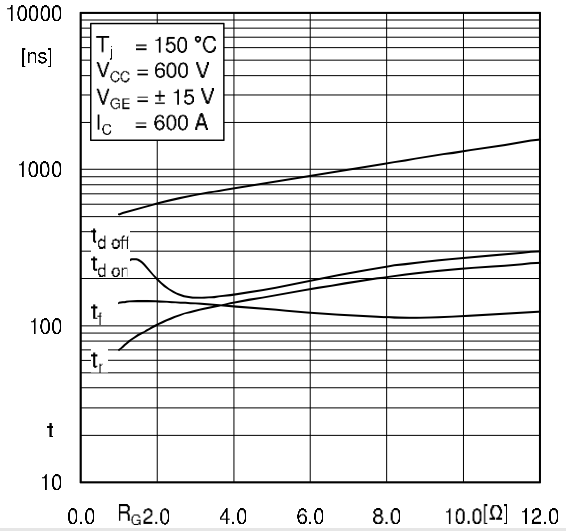

Fig. 8: Typ. switching times vs. gate resistor R_G

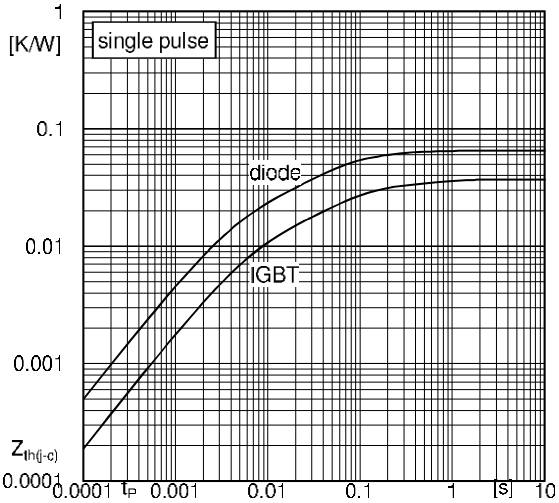

Fig. 9: Transient thermal impedance

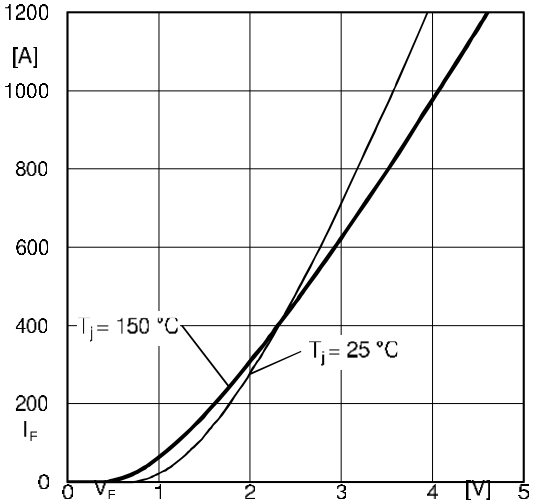

Fig. 10: Typ. CAL diode forward charact., incl. $R_{CC'+\,EE'}$

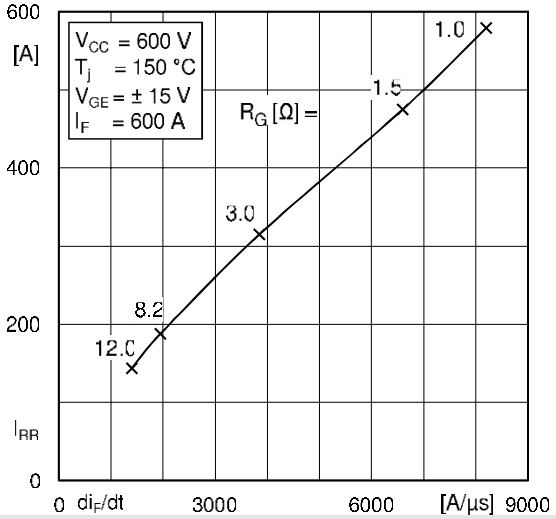

Fig. 11: Typ. CAL diode peak reverse recovery current

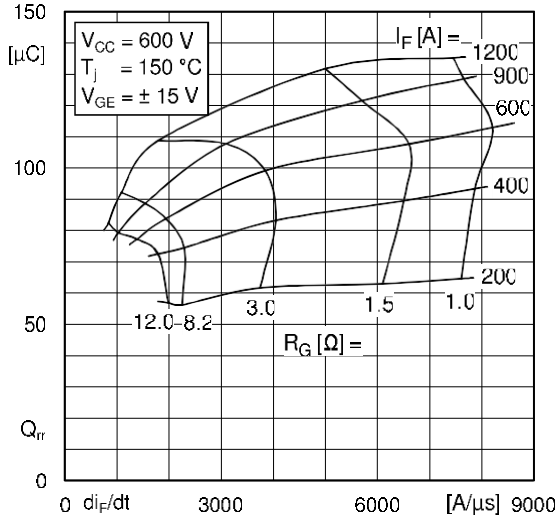

INGECOM SUN 50

INGETEAM INGECON SUN 50-100 Y 100-125TL

Modelo	50	60	70	80	90	100
Valores de Entrada (DC)						
Rango pot. campo FV	52 - 65	63 - 78	73 - 91	83 - 104	93 - 117	104 - 130
Rango de tensión MPP	405 - 750 V	405 - 750 V	405 - 750 V	405 - 750 V	405 - 750 V	405 - 750 V
Tensión máxima DC(2)	900 V	900 V	900 V	900 V	900 V	900 V
Corriente máxima DC	130 A	156 A	182 A	208 A	234 A	260 A
No entradas DC	4	4	4	4	4	4
MPPT	1	1	1	1	1	1
Valores de Salida (AC)						
Potencia nominal AC modo HT(3)	50 kW	60 kW	70 kW	80 kW	90 kW	100 kW
Potencia máxima AC modo HP(4)	55 kW	66 kW	77 kW	88 kW	99 kW	110 kW
Corriente máxima AC	93 A	118 A	131 A	156 A	161 A	161 A
Tensión nominal AC	400 V	400 V	400 V	400 V	400 V	400 V
Frecuencia nominal AC	50 / 60 Hz	50 / 60 Hz	50 / 60 Hz	50 / 60 Hz	50 / 60 Hz	50 / 60 Hz
Coseno Phi(5)	1	1	1	1	1	1
Regulación	Coseno Phi +/-0,9 a Pnom					
THD(6)	<3%	<3%	<3%	<3%	<3%	<3%
Rendimiento						

Eficiencia máxima	96,3%	96,40%	97,20%	97,50%	96,90%	96,80%
Euroeficiencia	94,30%	94,70%	96,10%	96,20%	95,80%	95,70%
	Datos Generales					
Consumo en standby(7)	30 W	30 W	30 W	30 W	30 W	30 W
Consumo nocturno	1W	1W	1W	1W	1W	1W
Temperatura de funcionamiento	-20 oC a +65 oC					
Humedad relativa	0 - 95%	0 - 95%	0 - 95%	0 - 95%	0 - 95%	0 - 95%
Grado de protección	IP 20	IP 20	IP 20	IP 20	IP 20	IP 20